Measurement of the π/K Ratio from the NuMI Target

A dissertation presented

by

Sin Man Seun

to

The Department of Physics

in partial fulfillment of the requirements

for the degree of

Doctor of Philosophy

in the subject of

Physics

Harvard University

Cambridge, Massachusetts

November 2007

©2007 - Sin Man Seun

Dissertation Advisor   Author

Professor Gary J. Feldman   **Sin Man Seun**

Measurement of the π/K Ratio from the NuMI Target

Abstract

Interactions of protons (p) with the NuMI (Neutrinos at the Main Injector) [1] target are used to create the neutrino beam for the MINOS (Main Injector Neutrino Oscillation Search) [2] Experiment. Using the MIPP (Main Injector Particle Production) experimental apparatus, the production of charged pions and kaons in p+NuMI interactions is studied. The data come from a sample of 2×10^6 events obtained by MIPP using the 120 GeV/c proton beam from the Main Injector at Fermi National Accelerator Laboratory in Illinois, USA. Pions and kaons are identified by measurement in a Ring Imaging Cherenkov detector.

Presented are measurements of π^-/π^+, K^-/K^+, π^+/K^+ and π^-/K^- production ratios in the momentum range p_T <2 GeV/c transversely and 20 GeV/c < p_z <90 GeV/c longitudinally. Also provided are detailed comparisons of the MIPP NuMI data with the MIPP Thin Carbon data [3], the MIPP Monte Carlo simulation and the current MINOS models [4, 5] in the relevant momentum ranges.

Contents

List of Figures

List of Tables

Acknowledgments

Chapter 1

Introduction

The study of proton interactions with different atomic targets represents the central goal of the Main Injector Particle Production (MIPP) experimental programme which is aimed at a comprehensive study of hadronic interactions at various energies. The MIPP detector layout combines wide acceptance coverage with complete particle identification, the aim being to collect large statistics data samples for all interaction types. This provides the basis for a model independent understanding of the underlying production mechanisms.

The MIPP experiment measures the secondary hadron production spectra in different momentum regions, and the present study addresses the pion/kaon ratio in 120 GeV/c proton on NuMI target interactions for momenta above 20 GeV/c. The motivation for these measurements comes from long-baseline neutrino oscillation experiments, such as MINOS (Main Injector Neutrino Oscillation Search) [2], which use

1

proton-target collisions to produce a well understood neutrino beam. The neutrinos in these experiments originate as the decay products of mesons (mainly pions and kaons) or of muons, which themselves are primarily pion or kaon decay products. Thus, understanding the detailed composition of accelerator neutrino beams relies heavily on understanding the nature of the hadronic cascade, i.e. the production spectra of the secondaries resulting from the collision of a high energy particle.

The available experimental data on this topic are presently not extensive. The precision of the MINOS experiment depends on the accuracy of the predictions of the neutrino fluxes at the Far detector based on the observations in the Near detector. This extrapolation of the neutrino energy spectrum is a strong function of the details of the production spectra of the secondary pions and kaons. The MIPP Experiment therefore aims to provide high precision reference data for the experiment.

The layout of this thesis is arranged as follows: previous measurements are discussed in Chapter 2. In Chapter 3, the MIPP experimental setup at Fermilab is described. Chapters 4 outlines several key reconstruction stages which are important for this analysis. Chapter 5 describes the NuMI target analysis, the results of which are presented and discussed in Chapter 6.

Chapter 2

Particle Production

One of the largest uncertainties in the extrapolation of the Near detector neutrino spectra to the Far detector site in MINOS arises from hadron production modeling of the NuMI target. This chapter reviews the available data and its relevance to the NuMI beam. The uncertainties in the absolute prediction and the relative Far-Near spectra due to uncertainties in hadron production are also estimated.

2.1 Particle Production Data from Related Experiments

The prediction of secondary production on the NuMI target has large uncertainties primarily due to the lack of available data relevant to the NuMI case. The most relevant measurements are as follows: Atherton *et al*[6], Barton *et al*[7] and SPY [8].

Figure 2.1 shows the p and p_T distribution of π at the target weighted by the number of predicted neutrino interactions produced at the MINOS Near and Far detectors for the low energy beam. Superimposed on the p and p_T distributions are points showing where previous measurements have been made. While the SPY data cover a reasonable fraction of the peak region (0<p<10 GeV/c), the hadron production data in the high energy tail ($p >$20 GeV/c) are significantly more sparse.

Low Energy Beam
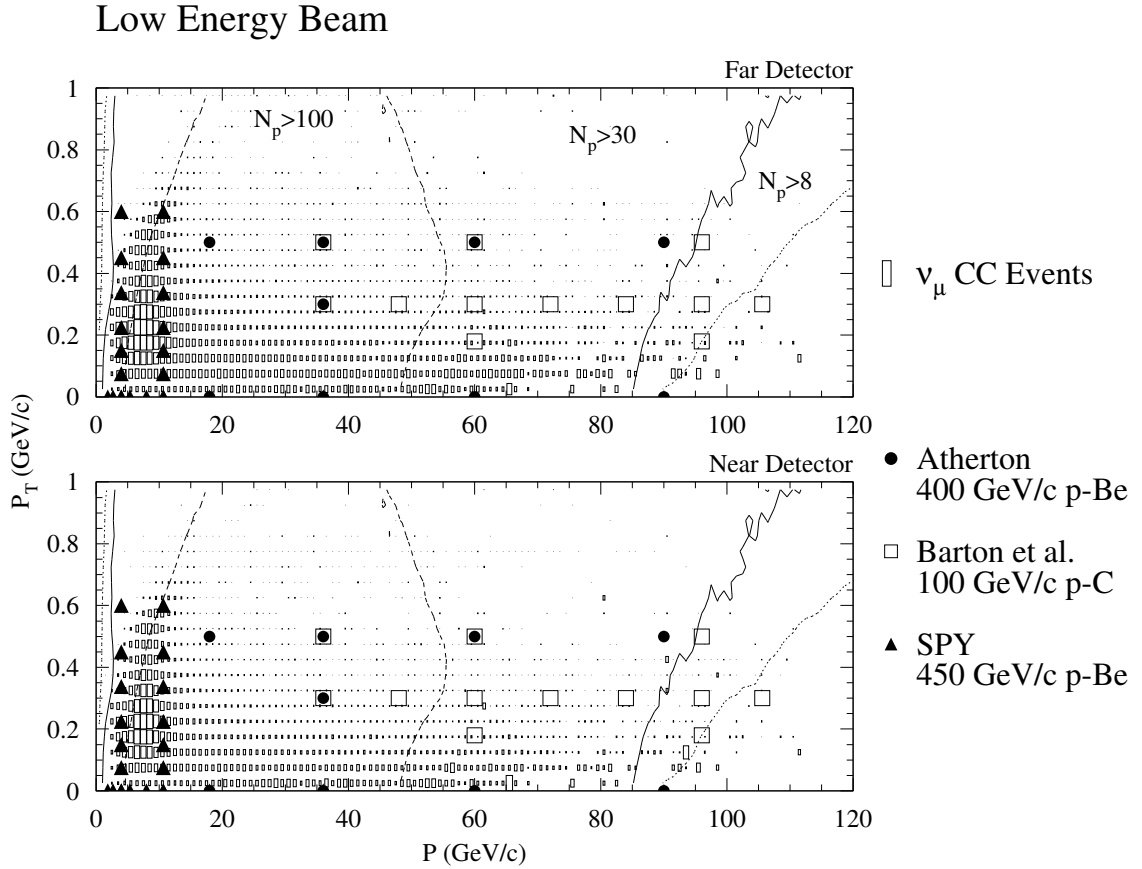
Figure 2.1: The distribution in p and p_T for secondary pions produced on the NuMI target. Secondaries have been weighted by their contributions to the neutrino event rate at the Far (top) and Near (bottom) detectors. Overlaid are the locations of existing hadron production measurements [9].

Most of the available data was taken using Beryllium targets at significantly higher

primary momentum and on shorter targets than that used by MINOS. The data must be extrapolated from different target nuclei and beam momentum to be applied to the NuMI case. For these reasons, roughly 20-30% uncertainties in the predictions of the secondary production of protons from the NuMI target are introduced.

2.2 Simulations of Particle Production from the NuMI Target and Uncertainties in the NuMI Neutrino Spectra

To estimate the impact of uncertainties in hadron production, simulations and parameterizations of the NuMI target have been made [9]. Figure 2.2 compares the predictions of the MINOS absolute neutrino event rates at the Near detector for four hadron production models of the NuMI target: GFLUKA (GEANT-FLUKA [10, 11, 12]), MARS [13], BMPT [14] and Malensek [15]. Variations in the absolute predictions are roughly 10-25%.

The extrapolation of the Near spectrum to the Far spectrum is not straightforward. The distance to the Far detector is roughly 1000 times larger than the length of the NuMI beamline. Thus, to a very good approximation the Far detector sees a point neutrino source. However, the Near detector sees an extended source of neutrinos. Figure 2.3 shows the estimated ratio of the Far neutrino flux to the Near neutrino flux for the same four models. The predictions differ by as much as 20% in the Far/Near

ratio.
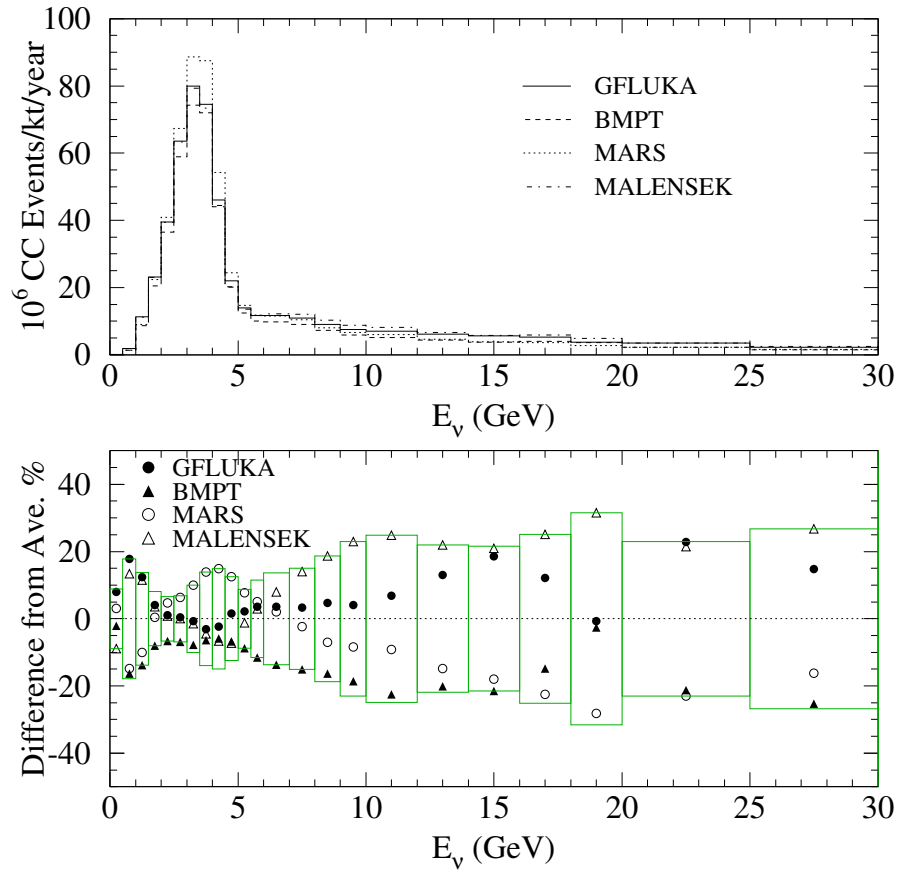
Figure 2.2: Predictions of the absolute neutrino rates at the MINOS Near detector using four hadron production models [9].

The MINOS experiment will compare the neutrino spectrum at the Far detector to the expected spectrum based on the measurement of the spectrum at the Near detector. Therefore, a reduction in the uncertainty in the Far/Near ratio due to hadron production would benefit the MINOS results.
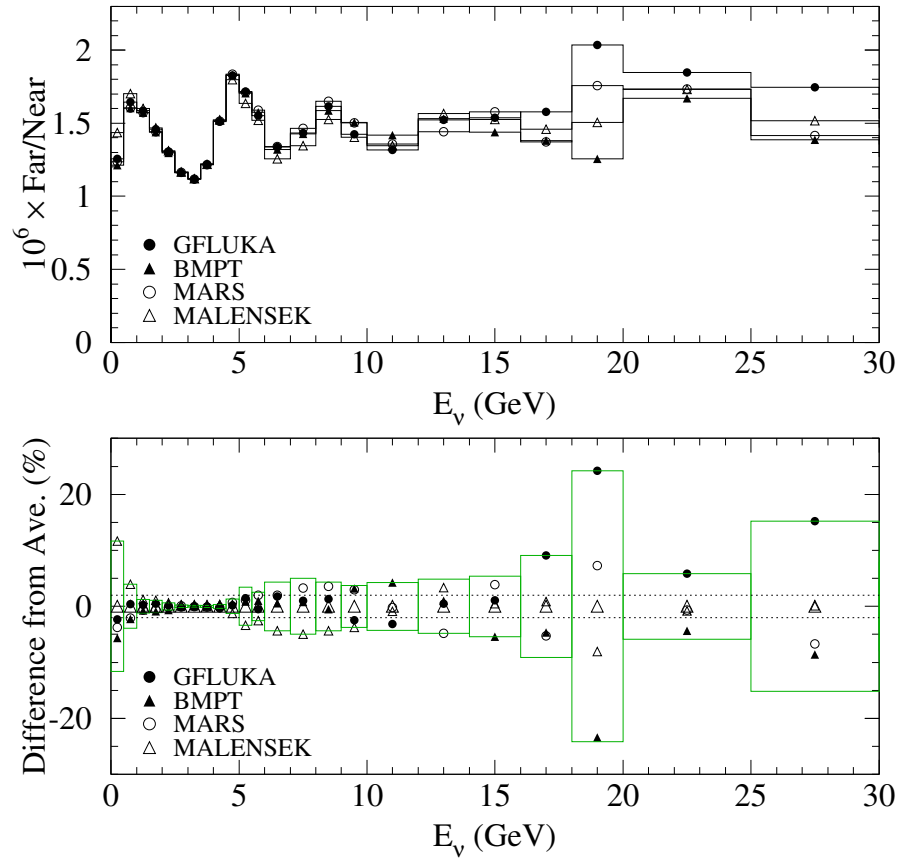
Figure 2.3: Predictions of the ratio of the Far neutrino flux to the Near neutrino flux using four hadron production models [9].

Chapter 3

The MIPP Experiment

The Fermilab experiment E907: the Main Injector Particle Production (MIPP) Experiment took fixed target data in the Meson Center Beam Enclosure 7 (MC7) beamline of the Meson Area at Fermilab from summer 2004 until the beginning of 2006. The experiment is designed to perform high statistics studies of hadron-nucleus interactions at various momenta (5 - 120 GeV/c) for target nuclei ranging from Hydrogen to Bismuth. It uses the 120 GeV/c proton beam from the Main Injector and measures particle production from primary beam interactions in the NuMI/MINOS target and primary and secondary beam interactions in a variety of thin targets. This data has applications in many fields of physics including neutrino beams, atmospheric neutrinos, nuclear physics, heavy ion physics, and proton radiography. The focus of this thesis is the analysis of data from the NuMI target running.

In the following sections, the details of the beamline and the detectors are de-

scribed.

3.1 The Beamline

MIPP runs in the Meson Center beamline. The experiment consists of a secondary beamline containing a beam transport pipe and a set of of Cherenkov counters. A picture of the physical layout of the MIPP beamline is given in Figure 3.1.
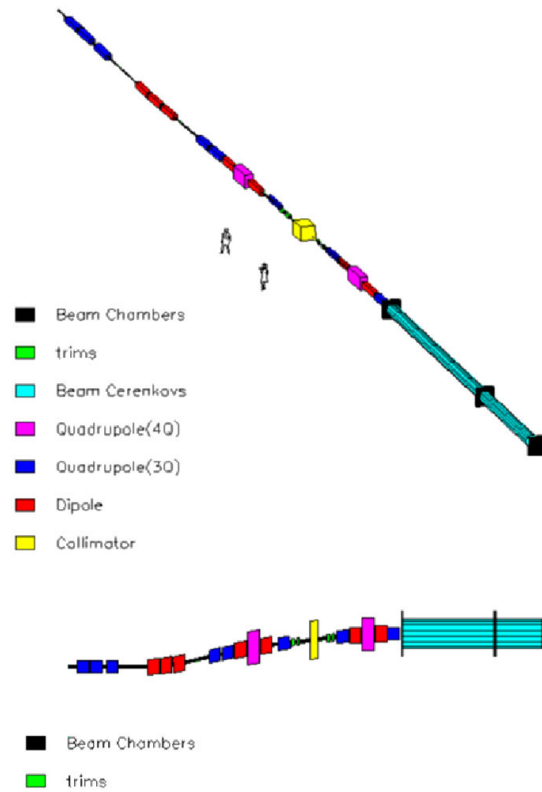
Figure 3.1: The elements and an elevation view of the MIPP beamline.

Primary data are acquired at 120 GeV/c by transporting a low intensity beam from the Main Injector directly onto the NuMI target. The beam flux is limited by

the data taking rate of the experiment. The Meson Center beamline also serves to provide a secondary beam of $\pi^{\pm}$, $K^{\pm}$, and $p^{\pm}$ particles to the MIPP experiment. The secondary beam momenta range from 5 GeV/c to 90 GeV/c. The incident secondary beam species are tagged by threshold beam Cherenkov counters upstream of the secondary target.

3.1.1 Primary Beamline

The primary beamline comes directly from the Main Injector. Control over primary beam characteristics is established through a focusing quadrupole doublet and adjustable collimators located upstream of the primary target. Due to enclosure restrictions and data taking rates in the Time Projection Chamber (TPC, to be described in Subsection 3.3.1), intensity on the primary beam was attenuated to less than 10^5 particles per second. By tuning the primary optics and the collimator aperture, the desired primary beam intensity was achieved. During the NuMI target running period, it was necessary to reduce the beam intensity to 10^3 particles/spill, with a 4-second spill occurring every two minutes from the Main Injector. This is because the NuMI target is two-interaction lengths long and so 90% of the incident particles interact with the target. The primary beam intensity had to be maintained at a lower rate so that the desired event rate was achieved thus avoiding pile-ups.

3.1.2 Secondary Beamline

Using protons from the Meson Center beamline, a secondary beam of charged π's and K's is produced. The π's and K's impinge on a secondary target - the scattering on the secondary target being the focus of the experiment. The secondary beamline is capable of selecting and transporting a beam with an energy in the range of 5 - 90 GeV/c. The secondary beamline must accommodate both the demanded momentum resolution and the precision in particle identification. The former requires the momentum-dispersed beam size to be larger than the transverse beam size and the latter requires low divergence at the Cherenkov detectors. A series of dipoles performs the momentum selection followed by the Cherenkov counters which identify the beam particles.

The primary target is a 0.5×0.5×20 cm copper block, located in between four dipole magnets. The first two dipoles bend the beam onto the primary target in MC5, and the latter two dipoles bend the beam back onto the beam center line for the Meson Center. In addition, three quadrupoles downstream of the primary target focus the beam onto a jaw collimator, with a vertical aperture which can be varied. The strength of the downstream dipoles determines the central momentum value of the beam, and the momentum spread, dp/p, is then set by the jaw aperture size. Finally, the beam is refocused onto the E907 experimental target by three additional quadrupoles.

3.1.3 Beam Cherenkov

The two Beam Cherenkov counters are long cylinders with heads at the exit of the counters. Each counter is read out through two PMTs - the inner PMT, which is covered by a second mirror with an aperture, and the outer PMT. The Cherenkov light from different particle types is reflected from the focusing mirror on the head. The reflected light below the cutoff angle is focused into the second mirror. The light that passes through the aperture of the second mirror is detected by the the inner photomultiplier. The reflected light above the cutoff angle is detected by the outer photomultiplier. The cutoff Cherenkov angle for the upstream counter is 5 mrad and the angle for the downstream counter is 7 mrad. The purpose of these counters is to identify the three possible beam particle species - protons, kaons, and pions. One counter is used to separate pions from kaons, and another is used to separate kaons from protons. The particles are all at the same momentum and that momentum ranges from 5 to 90 GeV/c.

For each threshold Cherenkov detector, one particle is below threshold and one is above. The lengths of the detectors are determined by the mass difference of the particles which need to be differentiated and the momentum at which the differentiation is made. The long detector is 22.9 m (to separate the pions from kaons) and the shorter one is 12.2 m long (to separate the protons from kaons), so they yield the same number of photoelectrons in the worst case (high momentum).

At specific pressure, the protons are below threshold in the upstream counter,

and the kaons and the pions are above the threshold and emit light in both. The Cherenkov light from the kaons are detected mostly by the inner PMT of the upstream counter and the outer PMT of the downstream counter. The light from the pions is incident on the outer PMT of the upstream counter, and the light from the protons focus onto the inner PMT of the downstream counter. Using two threshold Cherenkov detectors, one can then determine which particle passed, by looking for which PMTs get hit by Cherenkov light.

For the case of pion/kaon separation, the required momentum range can be accommodated by using Nitrogen gas. Also, the index of refraction is changed by varying the gas pressure so that the Cherenkov light of selected particles goes through the aperture and hits the inner phototube. The Cherenkov light from particles with masses different from those of the detected particle hit the outer phototube. In the case of the proton/kaon separation, the same gas is used for most of the momentum range. At low momenta (below 30 GeV/c) a larger index of refraction than Nitrogen is required. C_4F_{10} is used with maximum pressure to be set at about 3 atm. The lower momentum beams (5 GeV/c) can be separated by Time-Of-Flight instead of using a high index of refraction gas.

3.2   Targets

The MIPP experiment uses three different types of target: nuclear targets, a cryogenic target and the NuMI target.

The production thin nuclear targets are mounted on a target wheel, which was built by the University of Colorado and taken to Fermilab unassembled. It contains 6 slots, only four of which are occupied at any one time. The targets employed are Beryllium, Carbon 1%, Carbon 2%, Aluminum, Copper, Silver and Bismuth. In the order given, the targets are 0.94, 0.57, 0.94, 0.992, 0.973, 1.4 and 0.87 interaction lengths. The two vacant slots were used for background measurements. The wheel is not centered on the beam, since the target holes are off-axis. The wheel is turned by an ACNET (Fermilab Accelerator Control NETwork) controlled motor mounted to the Time Projection Chamber (TPC) table upstream of the TPC, and outside of the magnetic field of the "Jolly Green Giant" (to be described in Subsection 3.3.7).

The cryogenic target is used to run with liquid hydrogen, and requires a special setup.

MIPP used the spare NuMI target from MINOS, which is shown in Figure 3.2. The target core constitutes 47 graphite segments soldered to two stainless steel cooling pipes with an external diameter of 6.0 mm and thickness of 0.4 mm. Each graphite segment is 0.64 cm wide, 2.0 cm tall and 1.36 cm long with a 0.67 cm gap in between segments. The gaps between the segments allow most of the produced pions and kaons to leave the target before interacting and avoid contact of heated segments. The target core is inserted into a 0.4 mm thick, 30 mm diameter Aluminum cylinder casing. The total length of the casing is about 1.7 m long.

The NuMI target is made from carbon and almost 2 nuclear interaction lengths.
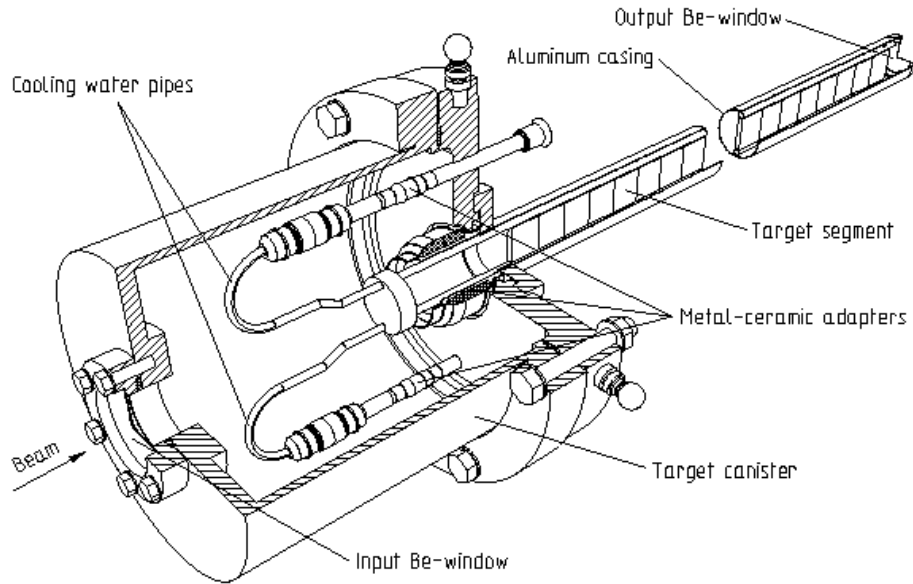
Figure 3.2: Schematic of the NuMI target design [16].

This leads to ~90% of the incoming protons to interact within the target, thus reducing the backgrounds created by non-interacting protons and maximizing meson production.

The pair of stainless steel cooling tubes were designed to remove heat deposited in the target in MINOS. Since the beam intensity during MIPP NuMI running period was much lower than MINOS, no water was circulated in the tubes. And this was taken into account in the MIPP Monte Carlo simulation, which is described in Section 4.1.

3.3 The Detectors

MIPP is a low-cost experiment which uses existing hardware to measure and identify a range of particles over a wide momentum range. The perspective layout of the MIPP experiment is shown in Figure 3.3 with the beam coming from the upper left, and Figure 3.4 shows a plan view of the MIPP detectors with a simulated shower in the Electromagnetic Calorimeter (EMCAL) and the Hadronic Calorimeter (HCAL). The sub-detectors are reused from previous Fermilab and Brookhaven fixed target experiments. The experiment uses a Time Projection Chamber (TPC) most recently used in the Brookhaven E910 experiment to provide vertex and track reconstruction. The TPC also provides particle ID at the lowest particle momenta ($p < 0.7$ GeV/c). The TPC is placed in a large magnet (the "Jolly Green Giant", JGG) which provides a field of 7 kG. Following the TPC, a threshold Cherenkov detector (also from E910) provides particle ID in the momentum range from 3 to 10 GeV. A Time-Of-Flight (TOF) system is used to fill in the gap in particle ID between 0.7 GeV and 3 GeV. The TOF is designed to have a 200 ps timing resolution, providing 2.5 σ particle ID separation at 2 GeV. Then follows the ROSIE spectrometer magnet (most recently used in the DONUT experiment, which provides a 10 kG magnetic field. Multi-wire proportional and drift chambers, taken from the E690 experiment, are interspersed throughout the apparatus. These are used in addition to the TPC for particle tracking. Downstream of ROSIE and the wire chambers is a Ring Imaging Cherenkov detector (RICH). Above 10 GeV, particle ID is provided by the RICH, which was
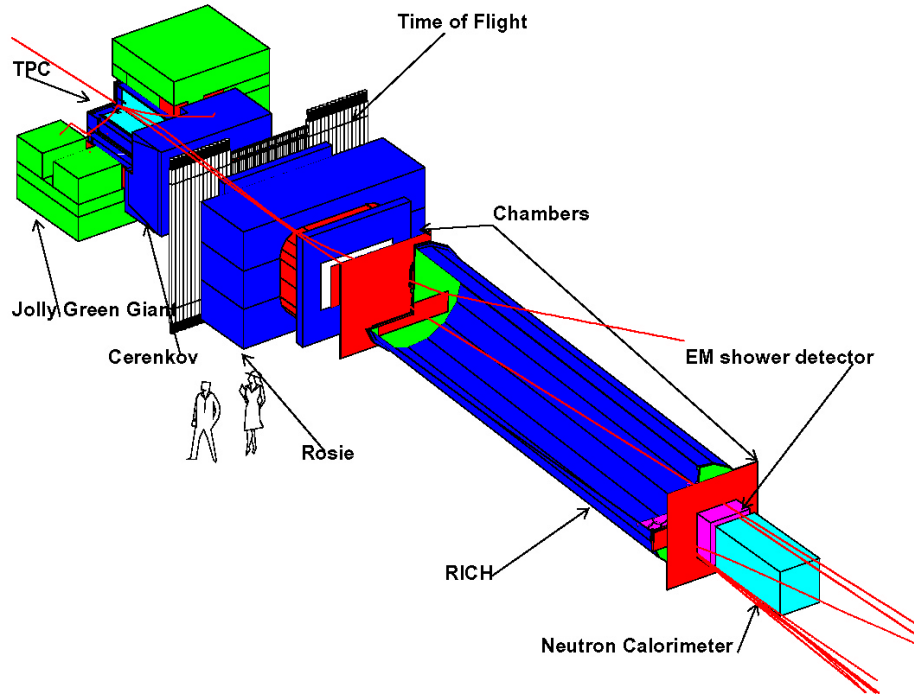
Figure 3.3: Layout of the MIPP experiment.

originally built for the SELEX experiment at Fermilab. This detector is of particular importance to the NuMI target measurement as the momentum range above 10 GeV is the most relevant for the MINOS neutrino fluxes. The final detectors in the chain are an electromagnetic calorimeter and a hadronic calorimeter.

3.3.1 Time Projection Chamber

One of the most important detectors in the MIPP Experiment is the Time Projection Chamber (TPC), operated with P10 (90% Ar, 10% CH_4) gas, a -10 kV drift potential, and +1,300 V anode potential for gas gain of the ionization signal. The TPC was built by Lawrence Berkeley National Laboratory (LBL) for the EOS exper-
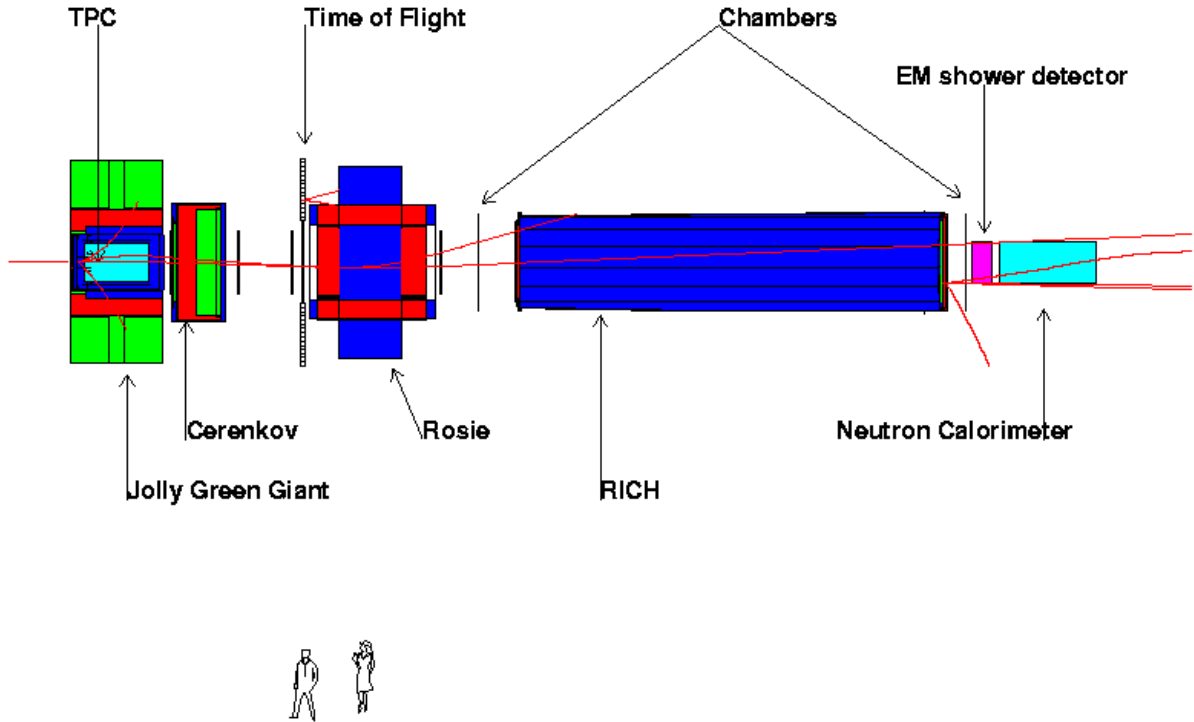
Figure 3.4: Plan view of the E907 detectors.

iment at the Bevalac. It was subsequently used by E907 and E895 at BNL, before being reused by MIPP. Figure 3.5 shows an exploded view of the chamber with the outer case removed.

The TPC provides true 3D tracking in the magnetic field for most of the particles exiting on the downstream side of the target. The active tracking region in the TPC is a rectangular box 1.5 m long in the beam direction, 96 cm wide in the bending direction and 75 cm high in the drift direction, with a uniform electric field of 120 V/cm. The beam passes directly through the center of the TPC volume. The tracking in the magnetic field of 7 kG measures particle rigidity and multi-sampling
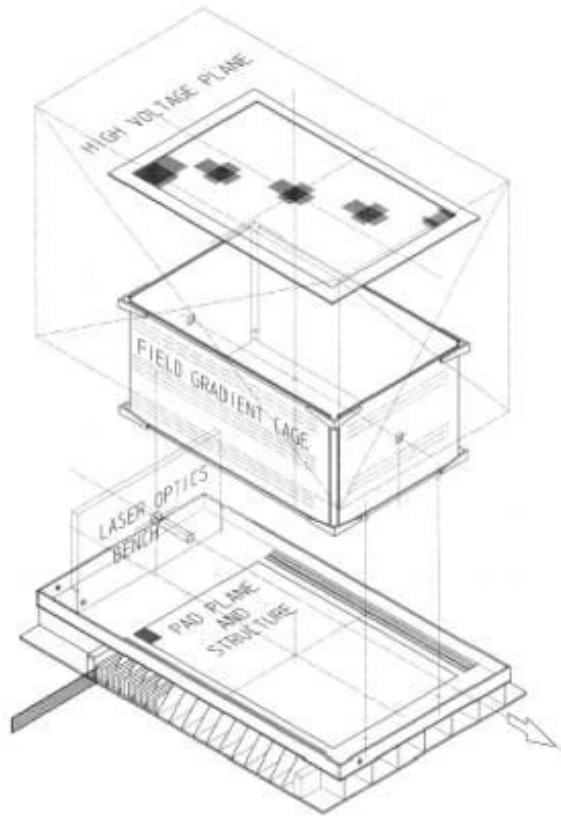
Figure 3.5: Exploded view of the TPC with the outer case removed. The active volume is defined by the pad plane, field cage, and high voltage (cathode) plane.

of dE/dx along the track provides particle ID.

The TPC was configured as a drift volume enclosed with a rectangular field cage sitting over a single, multi-wire proportional chamber (MWPC) - pad plane structure. Charged particles passing through the ground array are accelerated into anode wires. The electrons drift down under the influence of a uniform electric field set up by the cathode plane and ground wire array (Figure 3.6). The electrons pass through the ground array and are accelerated into anode wires. The electron-gas scattering that occurs in the high field region around the anode wires causes additional ionization.

The ionization induces image charges in the pads, which are amplified and digitized by the MWPC and recorded as a function of time. The MWPC pad plane provides a full 2D readout and the drift time provides the third dimension. The MWPC pad system is composed of 20 μm anode wires on a 4 mm pitch located 4 mm above a single panel, which is a continuous rectangular array of 8 mm by 12 mm pads (15,360 pads total). The electrons create avalanches as they drift to the anode wires. The positive ions created in the avalanche induce signals in the pads as they drift from the anode region. The induced signal is spread over 2 to 3 pads allowing accurate position determination through reconstruction. The TPC volume is divided up into a 2.5 million pixel volume (128 pad rows$\times$120 pads$\times$160 time buckets). The drift velocity is 5 cm/μs.
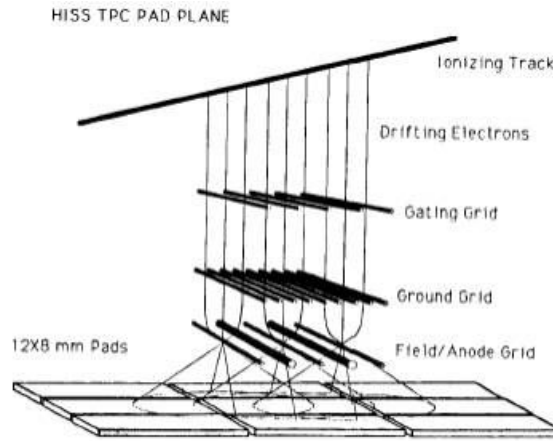
Figure 3.6: Sketch of the wire planes and field lines.

The 15,360 pads are read out via custom original electronics and a VME interface to commercially available data acquisition processors. The signals are written at

10 MHz and they are readout and digitized at a low rate with a commercial 12 bit ADC chip. Our data was recorded 100 ns time buckets.

3.3.2 Time-Of-Flight

The TOF wall is located immediately before the ROSIE magnet and consists of scintillator with R5900U phototubes. This system measures the time of flight for the particles between the target and the scintillator. The size of the TOF is 3.5 m wide by 3 m high. It has 54 3 m long scintillator bars, with 40 5 cm×5 cm bars at the center and the sides covered by 10 cm×10 cm. The TOF has the ability for particle identification between 1 GeV and 3 GeV, and it achieves 180 ps resolution on beam tracks. However, due to single-level trigger, a 150 ns delay cable was inserted. This caused variations up to 2 ns due to temperature changes in the experimental hall.

3.3.3 Cherenkov

The Cherenkov detector, shown in Figure 3.7(a), was used in the previous experiments BNL E766, FNAL E690 and FNAL E910. The Cherenkov counter is located immediately downstream of the first drift chamber. It is used to identify pions, kaons and protons. The gas radiator, C_4F_{10}, has a low threshold momentum of 2.6 GeV/c for charged pions, and 17 GeV/c for protons.

The box dimensions are W×H×D: 2.8194 m×3.3274 m×1.143 m. The size of the front aperture is 139.7 cm×190.5 cm. There are 96 primary mirrors arrayed into
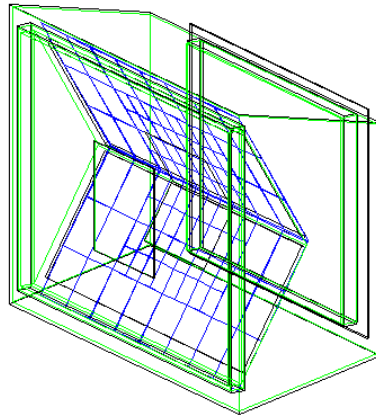
35	38	39	40	41	42	45	48
34	37	4 8 12 16 3 7 11 15	20 24 28 32 19 23 27 31			44	47
33	36	2 6 10 14 1 5 9 13	18 22 26 30 17 21 25 29			43	46
81	84	49 53 57 61 50 54 58 62	65 69 73 77 66 70 74 78			91	94
82	85	51 55 59 63 52 56 60 64	67 71 75 79 68 72 76 80			92	95
83	86	87	88	89	90	93	96

(a) A schematic view.

(b) The mirror numbering when looking at the front of the counter, with beam heading into the screen.
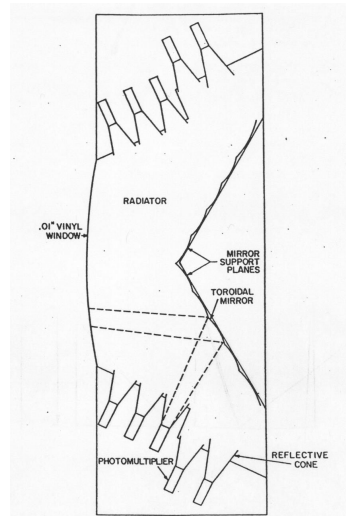
(c) Side View.

Figure 3.7: The Cherenkov detector.

two mosaics assembled on upper and lower panels. The mirrors come in three sizes: 6"×6.928", 12"×13.856" and 12"×9.660". The 6" mirrors are 1 mm thick glass, while the others are 1.5 mm thick. These mirrors divide the common radiator volume into the 96 detection volumes giving the detector its segmentation. Each mirror is matched to an individual phototube. Smaller mirrors cover the central part of the counter where the particle densities are higher. The mirror numbering and size are shown in Figure 3.7(b).

The secondary mirrors are right angled cones, tipped such that the axis of symmetry is coincident with the reflected central ray from the target off of the appropriate primary mirror. The secondary mirrors reflect Cherenkov light onto the photocathodes of the photomultiplier tubes. The side view in Figure 3.7(c) shows the schematic of the Cherenkov and the arrangement of the optics.

The tubes are modified with a wavelength shifting coating on the photocathode window surface to increase the detection efficiency by shifting blue Cherenkov light to green wavelengths.

3.3.4 Ring Imaging Cherenkov Detector

The RICH detector, pictured in Figure 3.8 uses a 32×89 array of $\frac{1}{2}$ inch photomultiplier tubes. An example event display is shown in Figure 3.9. The PMT array is used to measure the Cherenkov ring radius of particles traversing the gas volume.

The main parts of the detector (vessel, mirrors, photon detectors) are briefly
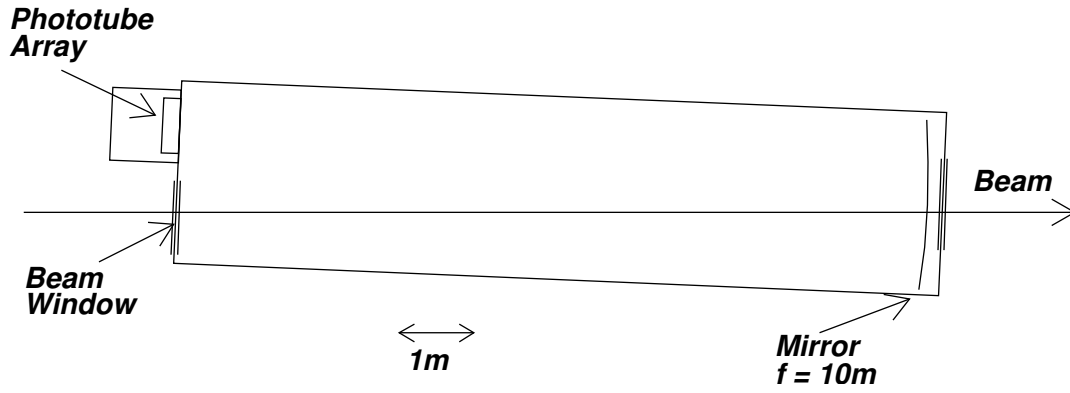
Figure 3.8: A schematic view of the RICH detector.
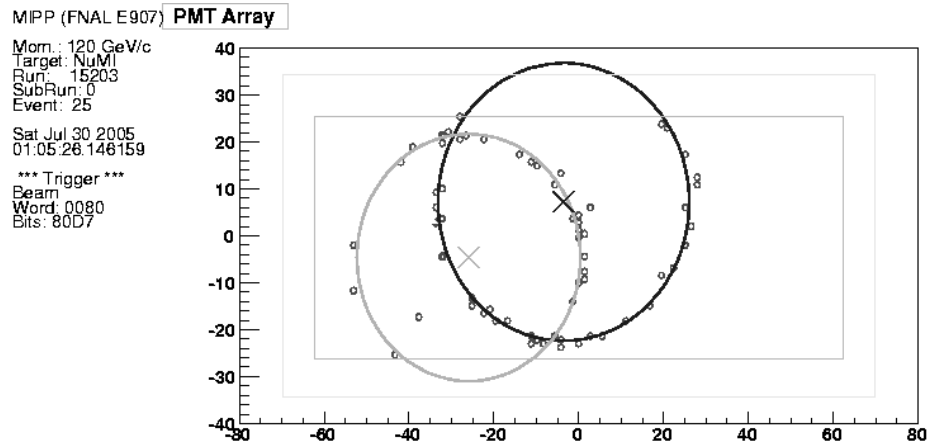
Figure 3.9: Online display in the RICH detector.

described below.

Vessel and Gas System

The RICH vessel is a low carbon steel radiator 10.22 m in length, 2.4 m. in diameter and with a wall thickness of $\frac{1}{2}$ in, filled with Carbon Dioxide at about 1.03 atm. The end flanges are 1.5 in. thick aluminum with provisions for thin beam

windows and a phototube holder plate to be described later.

Provisions were made for thermistors at both ends of the vessel to monitor internal temperature and a LED pulser test array to supply calibration signals for the phototubes.

The vessel is tilted off the horizontal axis by 2.4° with the beam entering horizontally through a thin window so that particles do not pass through the phototubes.

Over the course of a running period lasting for about a year the oxygen level was kept at 1000 parts per million. The volume of CO_2 slowly leaks over time, so CO_2 was added on a weekly basis to keep the pressure variation to within 1%.

To monitor the status of the detector, the following parameters were logged: atmospheric pressure, vessel pressure, vessel upstream temperature, vessel downstream temperature, temperature at several locations within the phototube box, voltages at the end of the HV Zener diode chains, and status of the low voltage system.

Mirrors

The mirror plane at the end of the vessel consists of an array of 16 hexagonally spherical mirrors, as shown in Figure 3.10. The mirrors are mounted in an array which is approximately 2.4 m wide and 1.2 m high, fixed individually to a flat, low mass honeycomb panel of 1 in. thickness with a 3-point kinematic mount. Each mirror is 40 cm across (46 cm tip-to-tip), 1 cm thick, made of low expansion glass, and has a reflectivity > 85% at 160 nm. The average radius of the mirrors is 19.8 m
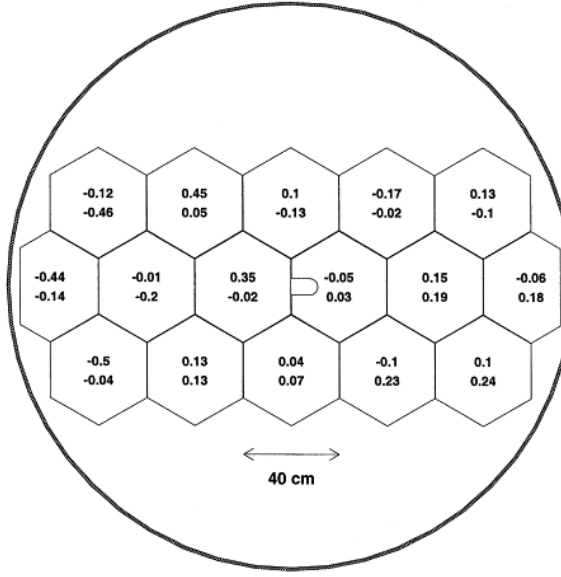
Figure 3.10: Mirror layout in the vessel. The numbers show the deviation from the average center of curvature for the horizontal (top) and vertical (bottom) coordinates in centimeters [17].

with a deviation of less than 5 cm RMS between mirrors as well as on one mirror.

After mounting the mirrors on the honeycomb panel, alignment was performed using a laser, the mirror angles were adjusted until the reflected spot was observed back at the center of curvature.

Photon Detectors

The phototube holder plate at the focal plane is shown in Figure 3.11. The phototube matrix consists of 2848 (89 columns×32 rows) hexagonally close packed (0.635 in. spacing) holes of approximately 0.6 in. diameter.

One side of each hole is a straight channel 2 in. in depth, which is used to support a phototube. A quartz window of 2 mm thickness was inserted into this side of the
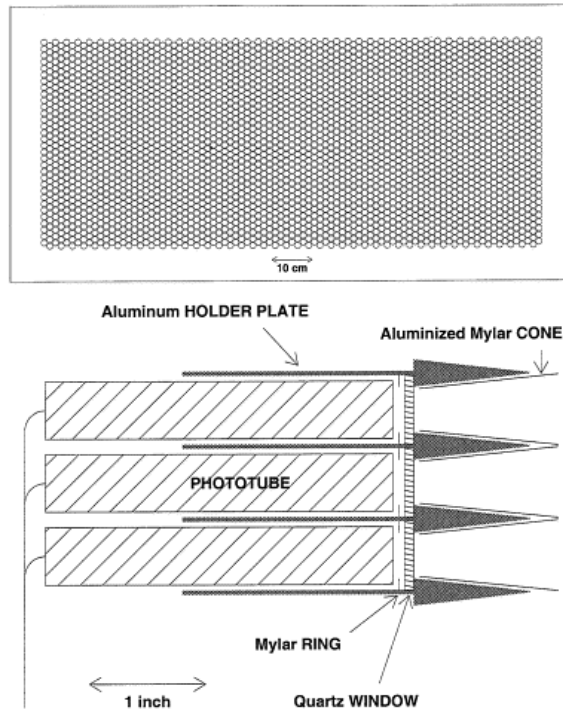
Figure 3.11: Front view (top) and partial cross section (bottom) through the photo-tube holder plate [17].

hole and glued in place. The other side of each hole is a tapered channel 1 in. in depth, with an inner radius of 0.4 in. An aluminized mylar cone is inserted into this side for each phototube and extends slightly out from the block in order to give essentially 100% coverage for detecting photons.

Two different types of $\frac{1}{2}$ in. diameter photomultipliers are used. The first is a commercially available Hamamatsu tube (R760) which has a quartz window allowing photon detection down to 170 nm. It has a quantum efficiency of approximately 25% at its peak wavelength of 350 nm. The second is a Russian tube (FEU60) which has a glass entrance window. These tubes were coated with wavelength shifter to reach the same wavelength range as the R760 tubes. The FEU60 tubes have an average

efficiency of only 36% compared to the R760 phototubes, i.e. 9% quantum efficiency. Tubes are grouped by operating point so that each column of 32 tubes can be run at the same high voltage.

In March 2004, due to a short on an FEU base, the RICH PMT array caught on fire and about 600 phototubes were damaged. The remaining tubes were spread throughout the array: in the central part of the phototube holder plate the Hamamatsu R760 tubes were installed in every 4th column starting at column 17 and ending at column 73; 15 columns were equipped with R760 tubes. The empty columns are located in every 4th column between column 0-40 and column 50-89. In the rest of the matrix, FEU60 tubes were installed.

To accommodate the wide range of operating voltages for the phototubes and the large number of tubes, six chains of air-cooled Zener diodes were used, each driven by a high voltage power supply delivering 200 mA. The voltage for each of the active columns was chosen based on the valid range of operating voltages for the set of tubes on the column.

The phototubes are grouped in sets of 16, two sets comprising a column of 32 phototubes in the 89×32 matrix. The output signals from a group of 16 phototubes are soldered onto paddle cards. The paddle cards plug into a backplane in one of three crates, located on top of the phototube box.

The readout electronics, mounted on cards in the crates, consist of a x20 differential amplifier and an analog comparator - one set per PMT, 32 sets per cards, and

one card for each PMT column.

The front-end electronics originally used in the SELEX experiment were completely replaced. The electronics prototype was produced at Fermilab and the production boards were fabricated and tested at Harvard University.

The front-end electronics cards are arranged into 3 crates, with 30 cards in each of the first two crates and 29 cards in the third crate. Each crate is controlled by one VME controller board.

3.3.5   Electromagnetic and Hadronic Calorimeter

There are two calorimeters at the downstream end of the apparatus, an Electromagnetic Calorimeter (EMCAL) and a Hadronic Calorimeter (HCAL). The lengths of these are 0.35 and 9.7 interaction lengths respectively. The transverse dimensions are 152.4 cm^2 and 100 cm^2 respectively. One of the main purposes of the EMCAL is to detect and measure the angles and energies of forward going photons. The HCAL detects neutrons and other hadrons and measures their energies.

Figure 3.12 shows a side view of the EMCAL and HCAL. The EMCAL consists of 5 horizontal and 5 vertical planes of proportional chambers attached to 0.2 inch-thick lead (absorber) sheets. Each layer has 1 radiation length of lead and 8 chambers. The proportional tubes were constructed from aluminum extrusions with anode wires strung through the center of each tube. The anode wires are 162 cm long and 25 μm in diameter and the wire-to-wire spacing is 2.54 cm. There are 8 chambers and 64 wires

in each plane and horizontal and vertical wire planes are stacked alternately to measure x and y positions. After assembly, the active volume is 162 cm×162 cm×31 cm. The EMCAL is 10 radiation lengths.
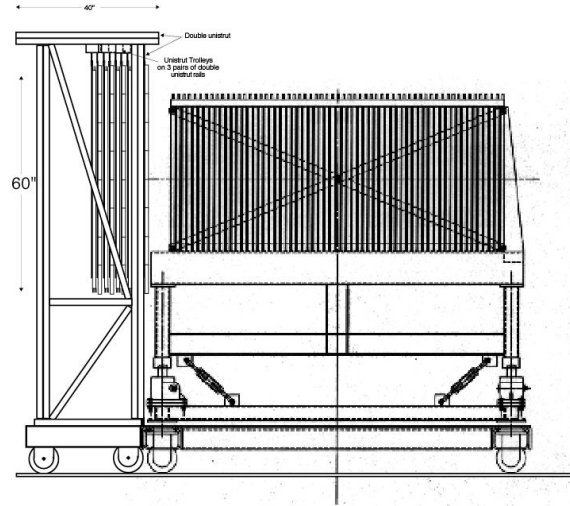
Figure 3.12: Side view sketch of the calorimeters.

The tubes use a gas mixture of P10 and CF_4 in an 86% - 14% ratio. The operating voltage for the anode wires is +2.3 kV. The operating voltage was chosen with the intent of maximizing dynamic range while at the same time providing sensitivity for the detection of minimum ionizing radiation.

Pulses from the wires are shaped and amplified after which they are digitized by ADCs and read out through a custom CAMAC module. The entire set of 640 wires is digitized by 4 ADCs in parallel.

The HCAL is situated behind the ECAL, and it is the most downstream detector. The calorimeter specifications are given in Table 3.1. The calorimeter is mounted

on a stand with jacks that allow limited vertical movement. A more detailed side view of the HCAL is found in Figure 3.13, showing showing fibers, light guides, and photomultipliers. The calorimeter is composed of 64 layers of 24.1 mm thick Fe and 5 mm thick scintillator, giving a sampling fraction of 3.5% and a total thickness of 88.5 radiation lengths and 9.6 interaction lengths. Its active area is 0.990 m wide by 0.980 m high.

Table 3.1: Hadronic Calorimeter specifications.

Type:	Sampling (Fe:scintillator, 5:1)
Composition	24.1 mm Fe, 5.0 mm PS scintillator
Layer depth:	36.93 mm
Number of layers:	64
Size (x×y×z):	0.990×0.980×2.388 m^3
Mass:	12667 kg
Cell size :(x×y×z)	0.495 m×0.980 m×16 layers
Total cells:	8 (2x×1y×4z)
Fiber diameter:	2.0 mm
Fiber separation:	30.0 mm
Fibers per cell:	16×16 = 256
Total fibers:	8×256 = 2048
Interaction length:	2.40λ_I per cell
	9.62λ_I total
Radiation length:	22.1X_0 per cell
	88.5X_0 total
Sampling fraction:	3.54%

The calorimeter is composed of Kuraray SCSN-81 PS scintillator. Each of the 64 sheets of scintillator has 32 keyhole-shaped channels milled into it, and they are separated by 30 mm. The light of the scintillator sheets is brought out by Bicron single-clad BCF-92 wavelength shifting fibers with a 2 mm diameter.
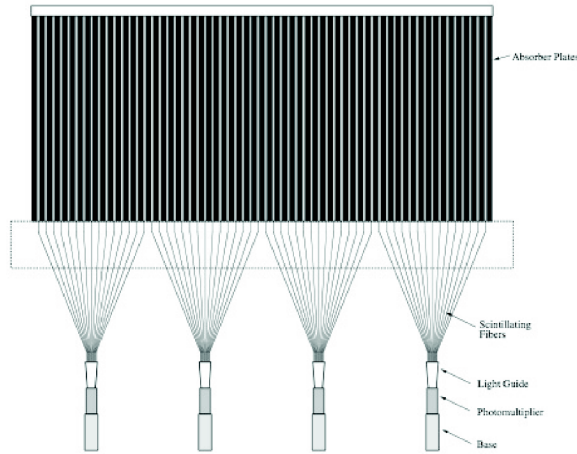
Figure 3.13: Hadronic Calorimeter details.

3.3.6 Drift and Proportional Chambers

The MIPP Experiment uses three small drift chambers (BC1, BC2, BC3) to measure the incoming beam particles (e.g. proton from primary beamline) and six large chambers to track particles downstream of the TPC. Four of the six large chambers (DC1, DC2, DC3, DC4) are drift chambers similar to the beam chambers in design. The two chambers in front and behind of the RICH detector are proportional wire chambers (PWC5 and PWC6).

All nine chambers have four planes of wires. The Beam Chambers have 160 wires per plane, and they are all identical. DC1 has 512 wires per plane. DC2, DC3 and DC4 have 512 wires on plane 2 and plane 3, but only 448 channels on plane 1 and plane 4 with wires at larger angles. The two PWCs have 640 wires per plane. The total number of wires read out is 14848.

The 9728 BC/DC channels are read out through 1216 8-channel pre-amps and 304

32-channel discriminators, while the PWCs have 160 32-channel pre-amps. During the run, the BCs and the DCs were read out with LeCroy 4291 TDCs, and the PWCs used RHM electronics.

The wire spacing is 1.016 mm in the Beam Chambers, 3.4925 mm in DC1, 3.175 mm in DC2, DC3 and DC4, and 3.0 mm in the PWCs. The BCs and DCs have wires at angles of $\pm 7.93°$ and $\pm 21.6°$ to the vertical. The PWCs measure x in plane 1 (vertical wires), y in plane 2 (horizontal wires), and angles of $\pm 28.07°$ in planes 3 and 4. The active area is 15.24×10.16 cm^2 in the BCs, 182.88×121.92 cm^2 in DC1, 152.4×101.6 cm^2 in DC2, DC3 and DC4, and 200×200 cm^2 in the PWCs.

3.3.7 Magnets

MIPP employs two the analysis magnets known as Jolly Green Giant (JGG) and ROSIE.

JGG was previously used in E690 at Fermilab and at BNL. It consists of four sets of coils, two sets on top and two below the aperture. Each set has 16 coils inside, and each coil has two turns. All coils in a set are operated in series. Over the course of the MIPP running period, several of these coils failed and were either fixed or removed. As a consequence, there are three field maps. Only the first field map was measured using Zip-tracking field measuring device, and the rest were simulated by computer models for use during reconstruction. In each of these configurations, the central field is approximately 7 kG and the field near the pole tips is 8 kG.

3.4 MIPP Acceptances for NuMI Target

A key feature of the MIPP experiment is its excellent particle identification capabilities. Almost all particle species across the entire kinematic range that can be produced from the 120 GeV/c primary proton beam can be unambiguously identified through a combination of the experiment's sub-detectors. This is illustrated in Figure 3.14. These detectors have nearly 100% acceptance over the full range of secondary momenta relevant to the MINOS experiment and track-by-track particle identification can be done at roughly the 3σ level over the same range. The data set taken by MIPP using the NuMI target should therefore provide a direct input to the simulations of the NuMI horn focusing system essentially eliminating hadron production as a significant source of uncertainty in the absolute prediction of the Near and Far detector spectra.

The overall acceptance regions for tracking pions and kaons in the RICH are shown in Figure 3.15(a) and Figure 3.15(b) respectively.
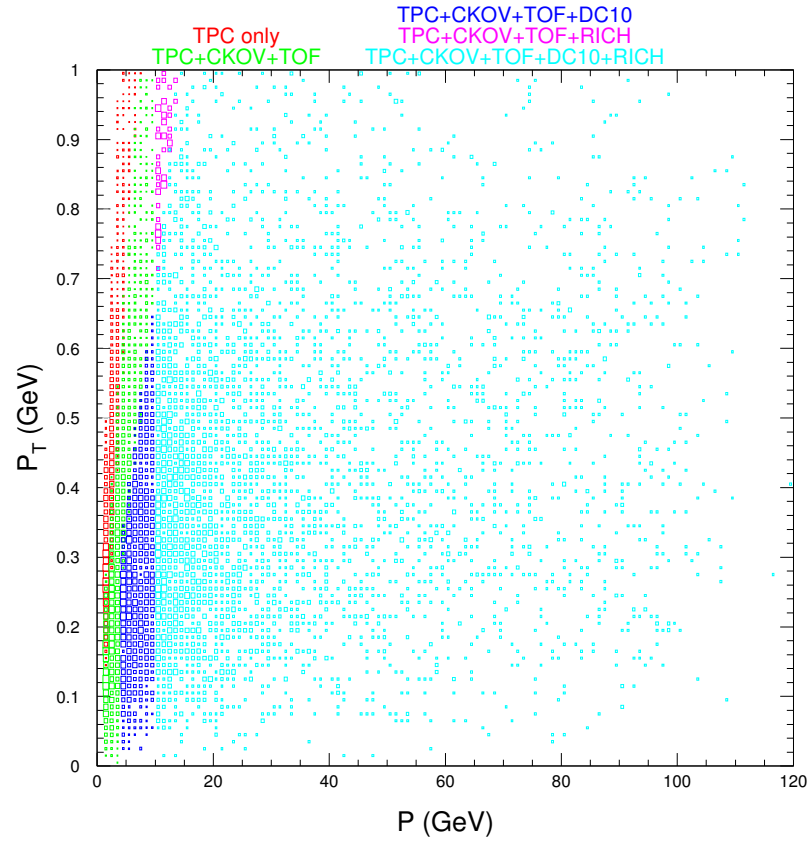
Figure 3.14: The acceptance of the various sub-detectors in the MIPP experiment as a function of secondary particle momentum and transverse momentum.
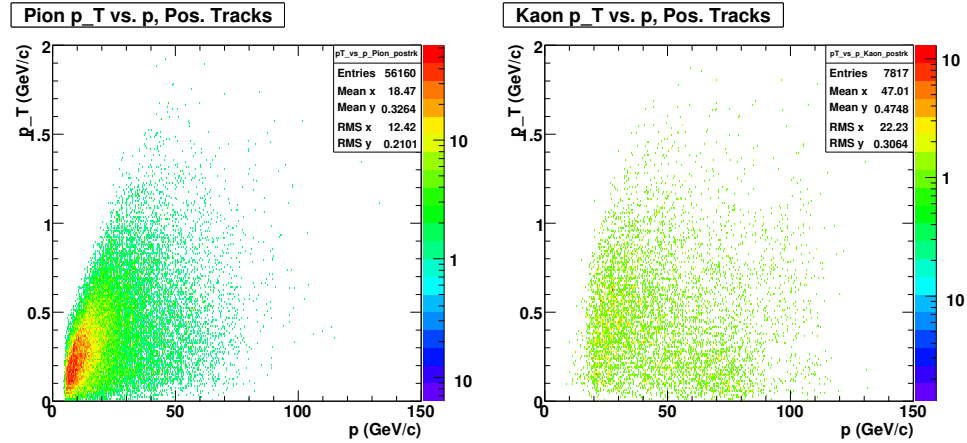
Figure 3.15: p_t vs. p spectrum for all positive (a) pion and (b) kaon tracks coming off of the NuMI target. Pions were selected using the RICH particle identification log-likelihoods [described in Subsection 4.3.3].

Chapter 4

Event Reconstruction

The event reconstruction proceeds through several steps. Firstly, a set of hits in the TPC and chambers is used in conjunction with the magnets to measure and calculate the 3-dimensional spatial coordinates, momentum and charge of charged particles. The complete kinematic description of an event requires that the mass of each particle is specified in addition to its momentum. This is achieved through particle identification using one or more of the sub-detectors. For the NuMI target analysis, the goal is to distinguish pions, kaons and protons. The RICH sub-detector provides this ability above 20 GeV/c. Below 20 GeV/c, the TPC, the TOF and the differential Cherenkov detector can be used. However, at the time of writing, these had yet to be implemented. For this reason, the main focus of this chapter is particle identification with the RICH and hence for particles above 20 GeV/c.

4.1 Monte Carlo Simulation

A Monte Carlo was developed to simulate the MIPP experiment. The MIPP Monte Carlo simulation is based on FLUKA-2006 [11, 12] for secondary particle production and GEANT [10] for tracking along the beam line and through the detector volumes.

The FLUKA beam simulation uses a modified version of the MINOS implementation of the NuMI target. The modifications are

- The incoming proton beam width is adjusted to that expected from the MIPP primary beamline.

- MIPP does not need to cool the target, so water volumes within the cooling tubes and helium volumes around the target are replaced by air volumes.

- Addition of a magnetic field. The NuMI target in the MIPP apparatus is in the fringe field of the JGG. However, as can be seen in Figure 4.1, for the momentum range concerned the particle production is insensitive to the presence of the field.

4.2 Tracking

Before tracking begins, a pre-processing step filters out beam pileup events. The remaining events are subject to a pattern recognition algorithm to identify tracks with at least 5 hits in the TPC and chambers. This step includes the formation of

(a) Positive particles.   (b) Negative particles.
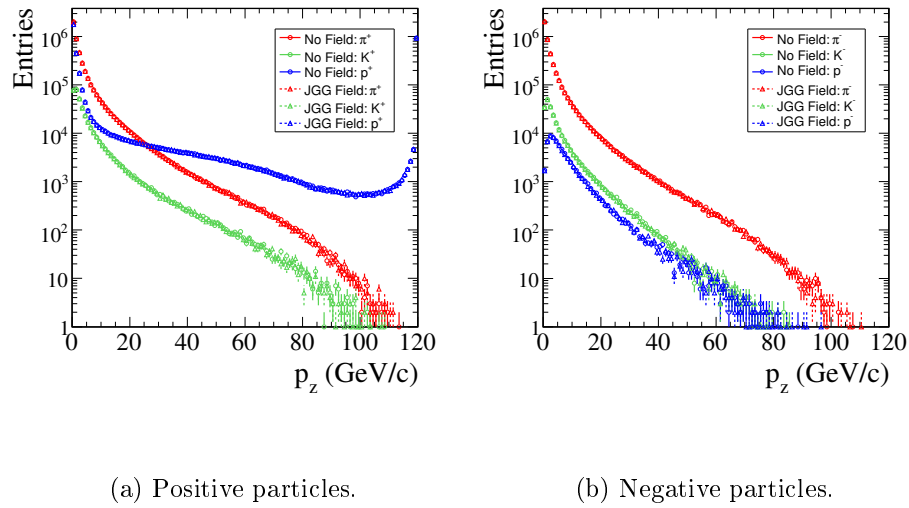
Figure 4.1: Effect of JGG magnetic field on particle production.

global tracks from track segments in the individual sub-detectors. The resulting global tracks are fitted for momentum based on their curvature in the magnetic fields. A detailed description of the tracking algorithm is presented in Andre Lebedev's thesis [3], a summary of which is given below.

The first major goal of tracking is to combine chamber hits across the length of the experiment into reconstructed tracks. The 9 chambers are grouped into three closely spaced sets (BC1/2/3, DC1/2/3 and DC4/PWC5/6) and each group is used to form a 3-dimensional track segment. The three track segments are then matched in order to form a chamber track candidate which can be fit for momentum based on its curvature in the ROSIE magnetic field.

The reconstruction of a track segment proceeds as follows: starting with hit wire

clusters in each plane of each chamber, all possible wire crosses between planes are found. These crosses are then examined across all three chambers in a group to find a consistent track segment. If a track segment has an acceptable χ^2, the procedure continues.

Chamber track candidates are then found by matching the track segments of DC1/2/3 and DC4/PWC5/6. The candidate is then checked for consistency with a BC1/2/3 track segment and matched if possible. Each track segment corresponds to a set of chambers in a field free region. The segments therefore form straight lines which specify the entry and exit points to the ROSIE magnetic field. This allows the momentum and direction of the particle trajectory to be calculated.

The TPC reconstruction is the next major step in the track reconstruction procedure [18]. The algorithm adopted has been adapted from that used by BNL E901 [19]. A global tracking algorithm is used to combine the TPC tracks with the chamber track candidates. Finally, a vertexing algorithm checks whether fully reconstructed tracks originate from a common point. This step is combined with a final vertex-constrained track fit to determine the momentum and direction from all available information.

4.3   Particle Identification

In this section, the algorithms used for particle identification with the RICH detector are described.

Cherenkov light is generated in a carbon dioxide radiator ($n - 1 \simeq 481 \cdot 10^{-6}$) of length $L = 986.827 \ cm$. Figure 4.2 shows a display of one event in the RICH. This display shows the signals observed in the RICH, the particle track vertex extrapolated from the chambers, and the predicted rings for the mass hypotheses π, K and p. Also, the momenta and charges of the tracks are given. Cherenkov photon signals along the predicted rings are clearly seen.
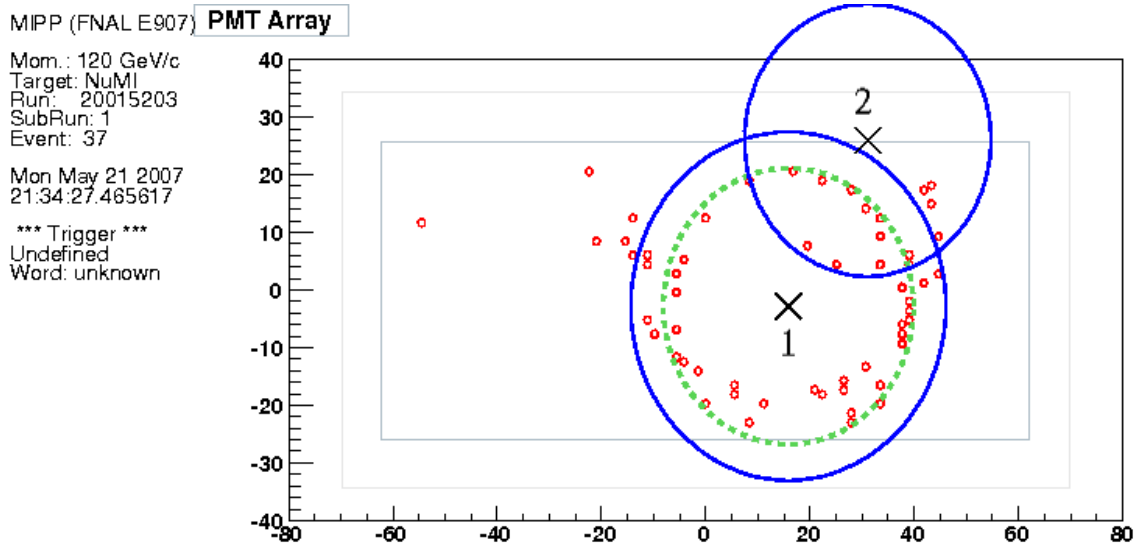
Figure 4.2: Event display in the RICH. Solid lines: rings predicted for the π mass hypothesis; dashed line: K hypothesis; crosses: predicted ring center from tracking. Cross 1: -25.9 GeV/c; Cross 2: -7.2 GeV/c.

To interpret the Cherenkov ring information and to construct analysis methods for identifying particles with high efficiency and low misidentification, the expected signals in the detector are now derived.

4.3.1   The Cherenkov Effect

The Cherenkov effect occurs when the velocity of a charged particle traversing a dielectric medium exceeds the velocity of light in that medium (c/n), where n is the index of refraction for the medium. Excited atoms in the vicinity of the particle become polarized and coherently emit radiation at a characteristic fixed angle θ, which is determined by the velocity of the particle and the index of refraction of the medium from the relation

$$\cos\theta = 1/\beta n \qquad (4.1)$$

with $\beta > 1/n$.

The index of refraction of a material is a function of wavelength, temperature and pressure. Figure 4.3 shows the variation of n with wavelength for CO_2, where n decreases with increasing λ. The variation with temperature is small.

According to Equation 4.1, there is a threshold velocity $\beta_{threshold} = 1/n$ below which no light is emitted. As the particle velocity increases beyond $\beta_{threshold}$, the light is given off at larger and larger angles up to a maximum $\theta_{max} = \cos^{-1}(1/n)$ which occurs for $\beta = 1$.

The amount of energy emitted per unit length and per unit wavelength interval $d\lambda$ by a singly charge particle is given by

$$\frac{dE}{dx d\lambda} = \frac{4\pi^2 r_e m c^2}{\lambda^3}\left(1 - \frac{1}{\beta^2 n^2}\right) \qquad (4.2)$$

where r_e is the classical radius of the electron. The emitted energy is strongly peaked
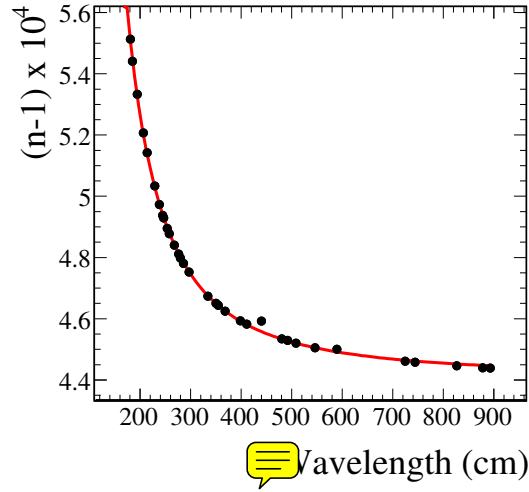
Figure 4.3: Index of refraction of CO_2 as a function of wavelength.

at short wavelengths. Equation 4.2 can be rewritten in terms of the number N of emitted photons as

$$\frac{dN}{dx d\lambda} = \frac{2\pi\alpha}{\lambda^2}\left(1 - \frac{1}{\beta^2 n^2}\right) \tag{4.3}$$

where α is the fine structure constant. The total number of photons emitted per unit path length is

$$\frac{dN}{dx} = 2\pi\alpha \int_{\beta n > 1}\left(1 - \frac{1}{\beta^2 n^2(\lambda)}\right)\frac{d\lambda}{\lambda^2} \tag{4.4}$$

If the variation in $n(\lambda)$ is small over the wavelength region λ_1 to λ_2, the energy emitted per unit length becomes

$$\frac{dE}{dx} = 2\pi^2 r_e mc^2 \sin^2\theta\left(\frac{1}{\lambda_1^2} - \frac{1}{\lambda_2^2}\right) \tag{4.5}$$

while the photon yield is

$$\frac{dN}{dx} = 2\pi\alpha \sin^2\theta\left(\frac{1}{\lambda_1} - \frac{1}{\lambda_2}\right) \tag{4.6}$$

Using the wavelength interval 155 - 670 nm, corresponding roughly to the response range of the photomultiplier tubes in the RICH, we find that

$$dE/dx \;=\; 11200 \sin^2 \theta \qquad \text{eV/cm}$$

$$dN/dx \;=\; 2270 \sin^2 \theta \qquad \text{photons/cm} \tag{4.7}$$

For a singly charged particle with $\beta \sim 1$ traversing CO_2 ($n \sim 1.000481$), the Cherenkov angle is 1.78°. This implies that 10.8 eV/cm is given off as Cherenkov radiation, which is small compared to the energy loss due to ionization.

The angular distribution of the light intensity is approximately a δ function at the Cherenkov angle. The actual distribution observed is broadened due to dispersion, energy loss of the particle, multiple scattering and diffraction in the detector.

4.3.2 Detector Effect

The mirrors gather the Cherenkov light produced by a particle traversing the region and focus it onto the PMT array. The reflection coefficient for light at normal incidence on the mirror surface is shown in Figure 4.4. In the visible spectrum the mirrors have high reflectance. However, in the far ultraviolet region, they have a much lower reflectance.

Another important consideration is the transmission of light through the medium. Carbon dioxide has absorption bands in the far ultraviolet portion of the spectrum. Figure 4.5 shows the region over which CO_2 has a high absorption.
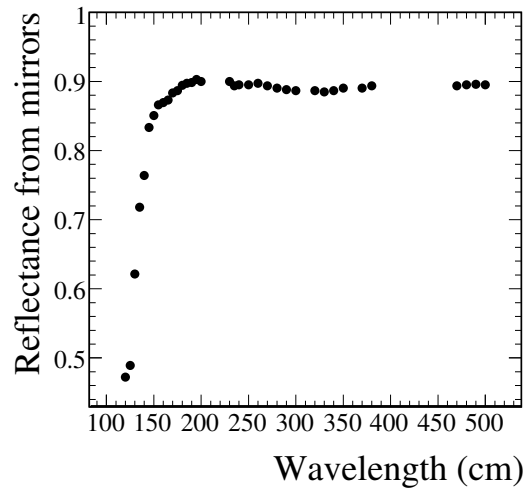
Figure 4.4: The reflectance at normal incidence from mirrors.
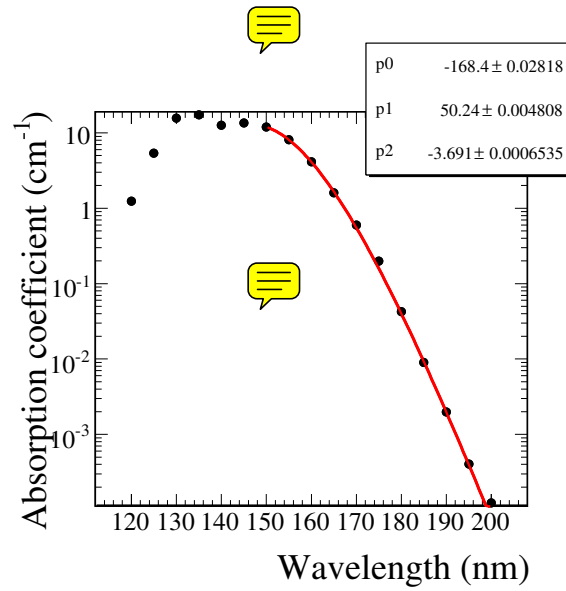
Figure 4.5: Absorption region of Carbon Dioxide.

Figure 4.6 shows light transmission efficiency for the PMT and its housing. Figure 4.6(a) is the efficiency of reflection from the cones as a function of wavelength;

Figure 4.6(b) is the efficiency with which light is transmitted through the quartz window. Note that the quartz allows light transmission below 200 nm; finally, Figure 4.6(c) shows the PMT quantum efficiency as a function of wavelength.
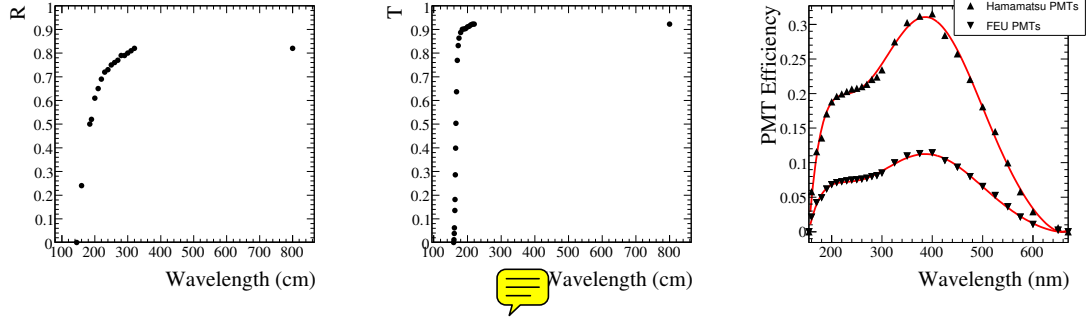
(a) Efficiency of reflection from cone.

(b) Efficiency of light transmission through quartz window.

(c) PMT quantum efficiency.

Figure 4.6: Efficiencies of light transmission of a PMT and its housing as a function of wavelength.

The photoelectron output of a given PMT is obtained by convolving the frequency spectrum of produced Cherenkov radiation with the frequency response of the collection system and tube. Thus, using Equation 4.3 for the number of photons produced per unit path, we find that the number of emitted photoelectrons in the tube per unit particle pathlength is

$$\frac{dN_e}{dx} = 2\pi\alpha \int \left(1 - \frac{1}{\beta^2 n^2}\right) \epsilon_c(\lambda) \frac{d\lambda}{\lambda^2} \tag{4.8}$$

where $\epsilon_c(\lambda)$ is the efficiency for collecting photons of wavelength λ at the cathode.

The number of photoelectrons can then be written in the form

$$N_e = N_0 L \sin^2 \theta \tag{4.9}$$

where L is the length of the radiator and the various efficiencies and spectral responses are incorporated in the constant N_0.

The index of refraction of the gas is related to its density ρ through the Lorenz-Lorentz law

$$\frac{n^2 - 1}{n^2 + 2} \frac{M}{\rho} = R \tag{4.10}$$

where M is the molecular weight and R is the molecular refraction coefficient.

Since for gases $n \simeq 1$, Equation 4.10 can be rewritten to a high degree of accuracy as

$$n - 1 \simeq \frac{3}{2} \frac{R}{M} \rho \tag{4.11}$$

From the ideal gas law

$$P = \rho R' T / M \tag{4.12}$$

where P is the pressure, T is the absolute temperature, and R' the gas constant. From Equation 4.11 and Equation 4.12, we obtain the following equation

$$n - 1 = (n_0 - 1)\rho/\rho_0 \tag{4.13}$$

where the subscript 0 indicates that the quantity is measured at standard temperature and pressure.

4.3.3 Maximum Likelihood Method for Particle Identification

The RICH exploits the Cherenkov process since only particles whose velocity exceeds some minimum value produce light. As the different particle species have different masses, given a momentum measurement, the RICH can be used to distinguish between particles based on ring radius.

A maximum likelihood approach for particle identification is used. Each particle which crosses the active area of the RICH and which is above the Cherenkov threshold

$$\gamma_{threshold} = \frac{1}{1 - \beta_{threshold}^2} = 32 \tag{4.14}$$

produces Cherenkov light which is focused by the spherical mirror with focal length, $F = 10 \; m$, onto a ring of radius

$$R = F\sqrt{\frac{1}{\gamma_{threshold}^2} - \frac{1}{\gamma^2}}. \tag{4.15}$$

In our case, $R = 32 \; cm$ for $\gamma \to \infty$. The position of the ring center in the focal surface and the ring radius for the different mass hypotheses can be predicted from the parameters of the track and the particle momentum measured in tracking. we only consider the mass hypotheses of e, μ, π, K and p.

The method for particle identification is to count the number of observed digits in the "search band": the RICH active region between the smallest physically possible ring radius and the electron radius for a given momentum. The probability of producing each observed digit is calculated for each particle hypothesis. The ring can

then be associated with the most probable hypothesis. The probability calculation

proceeds as follows.

The detection efficiency may be calculated as

$$\epsilon(\beta) = 1 - Pr(0, N_e) \tag{4.16}$$

where $Pr(0, N_e)$ is the probability that no electrons where emitted by the photocath-

ode of the PMT if the average number is N_e. According to Equation 4.8, N_e depends

on β, the collection efficiency, and the quantum efficiency of the tube. Since the

photoelectron emission follows a Poisson distribution, we have

$$\epsilon(\beta) = 1 - \exp(-N_e) \tag{4.17}$$

For each mass hypothesis j, we assume a probability function to observe photoelec-

trons $N_e^{(i)}$ at each photomultiplier i. The probability of observing $N_e^{(i)}$ photoelectrons

is

$$P_j^{(i)} = f_j(N_e^{(i)}). \tag{4.18}$$

The joint probability to find all photoelectrons at their observed positions is the

product

$$\prod_{i=1}^{m} f_j(N_e^{(i)}) \tag{4.19}$$

where m is the total number of photomultipliers in the search band.

According to the Poisson distribution in Equation 4.17, if photomultiplier i has a

digit, the probability to observe exactly N_e photoelectrons for the signal is

$$S_j(N_e^{(i)}) = 1 - \exp(-N_e^{(i)}) \tag{4.20}$$

Otherwise, the probability is

$$S_j(N_e^{(i)}) = \exp(-N_e^{(i)}) \tag{4.21}$$

We also expect some background hits, which have a constant probability, $B^{(i)}$, of occurring over the surface of each photomultiplier, depending on its type (Russian or Hamamatsu) and not on the hypothesis j. This background estimate is calculated from the number of digits seen in the PMT array and is taken from the data set.

If we combine signal $S_j(N_e^{(i)})$ and background $B^{(i)}$, we get the probability for a photomultiplier with detected photoelectrons

$$f_j(N_e^{(i)}) = 1 - \exp(-N_e^{(i)})(1 - B^{(i)}) \tag{4.22}$$

and the probability for a photomultiplier without a hit

$$f_j(N_e^{(i)}) = \exp(-N_e^{(i)})(1 - B^{(i)}) \tag{4.23}$$

We get the likelihood function for hypothesis j

$$\mathcal{L}_j = \prod_{i=1}^{m} f_j(N_e^{(i)}) = \begin{cases} \prod_{i=1}^{m} \left(1 - \exp(-N_e^{(i)})(1 - B^{(i)})\right) & \text{PMT has a hit} \\ \prod_{i=1}^{m} \exp(-N_e^{(i)})(1 - B^{(i)}) & \text{PMT has no hit} \end{cases}$$

Thus log-likelihood function reads

$$\log \mathcal{L}_j = \sum_{i=1}^{m} f_j(N_e^{(i)}) = \begin{cases} \sum_{i=1}^{m} \log \left(1 - \exp(-N_e^{(i)})(1 - B^{(i)})\right) & \text{PMT has a hit} \\ \sum_{i=1}^{m} \left(\log(1 - B^{(i)}) - N_e^{(i)}\right) & \text{PMT has no hit} \end{cases}$$
$$\tag{4.24}$$

If the particle is below threshold, we expect only background (we denote this hypothesis by the index 0). In this case, $N_e^{(i)}$ is zero and we get the simple expression

$$\mathcal{L}_0 = \begin{cases} \prod_{i=1}^m B^{(i)} & \text{PMT has a hit} \\ \\ \prod_{i=1}^m \left(1 - B^{(i)}\right) & \text{PMT has no hit} \end{cases} \tag{4.25}$$

To discriminate different mass hypotheses i and j, a cut on the log likelihood ratio $R_{ij} = \log(\mathcal{L}_i/\mathcal{L}_j) = \log(\mathcal{L}_i) - \log(\mathcal{L}_j)$ is applied. For the analysis of experimental data, simultaneous cuts for different log likelihood ratios, e.g. for R_{Kp} and $R_{\pi p}$ are used. These cuts are usually momentum dependent.

This method works well for particle identification in events with only a few rings, but as the number of rings increases, the search bands overlap, and the efficiency goes down and misidentification goes up. Therefore, an extension to the method was developed which favors the information from digits that unambiguously belong to a single ring. This will be described in the following section.

4.3.4 Iterative Weighting Method

When analyzing data recorded by the RICH, each digit on the photomultiplier array has to be considered in the evaluation of the likelihood for a given charged track. In cases where ring radii are rather large and track density is high, a considerable overlap of rings appears. In such a case, the peak in the radius distribution corresponding to the digits from the considered track might become obscured by the contribution of digits from the neighboring tracks. In the standard approach, the

background at the photomultiplier array is measured, and the likelihood functions for various particle hypotheses are calculated as in Subsection 4.3.3.

To improve this method, we notice that most of the background digits actually belong to other tracks in the events, which suggests that an iterative procedure, in which each digit would gradually become predominately associated with one of the tracks, could be used reduce the background level. This method is described in [20], and summarized in this subsection.

For each of the tracks and for each of the photons, the corresponding ring radius is first calculated, and a histogram is filled . In the iterative approach, we proceed to clean up the histograms in the following way: instead of using a weight of one for a given photon in all three histograms, each photon is ascribed a weight such that the sum of weights is equal to one for each photon. The weight for a specific photon in the histogram corresponding to the track k is calculated for the next iteration according to the formula

$$w_k = \frac{y_k}{\sum_{itrk=0}^{n} y_{itrk}} \tag{4.26}$$

where y_{itrk} is the number of entries in the bin, into which the given photon fits, in histogram $itrk$. As a result, a photon is given the highest weight in the histogram, where it fits into the peak, and lowest, where it is part of a scarcely populated background.

The likelihood function is then constructed in the following way. Consider each digit i in a given track with the corresponding weight w_i, the likelihood function

becomes

$$\log \mathcal{L}_j = \begin{cases} \sum_{i=1}^{m} w_i \log\left(1 - \exp(-N_e^{(i)})(1 - B^{(i)})\right) & \text{PMT has a hit} \\ \sum_{i=1}^{m} w_i \left(\log(1 - B^{(i)}) - N_e^{(i)}\right) & \text{PMT has no hit} \end{cases} \tag{4.27}$$

where the index i runs over all digits in the $e/\mu/\pi/K/p$ hypotheses windows, and number of digits $n_r = \sum w_i$.

4.4 RICH Alignment

The 16 mirrors in the RICH which reflect Cherenkov light onto the PMT array must be aligned in software in order to facilitate ring/track matching. The mirrors are assumed to be transversely shifted from their nominal positions only; longitudinal shifts and rotations are not accounted for in the following procedure. Alignment constants are calculated on a run-by-run basis.

The events are reconstructed as usual and a mirror is determined for each track based on its trajectory. The predicted spatial coordinates of an associated ring center on the PMT array are then calculated. An independent algorithm is also run on the RICH digit information only in order to find and fit the rings. An alignment constant can then be found for each mirror based on the agreement between the track coordinate prediction and that found by the ring-finding algorithm. Figure 4.7 shows the distributions used to determine the constants for each mirror.
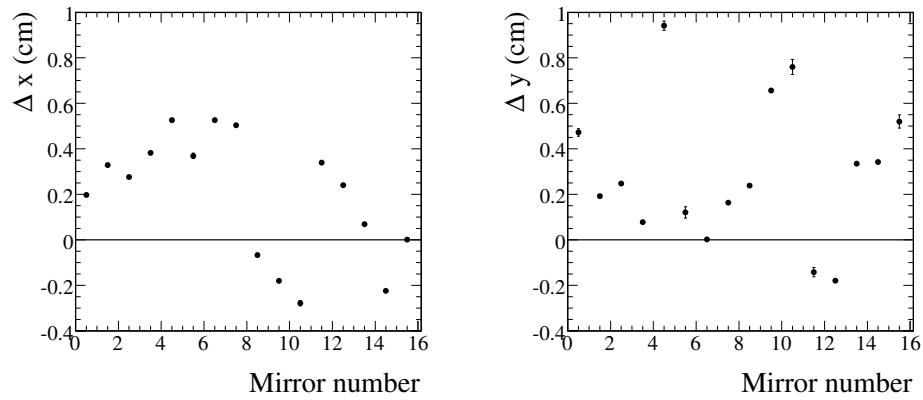
Figure 4.7: RICH alignment constants in x (left) and y (right) versus mirror numbers.

4.5 RICH Calibration

In solving Equation 4.8 for N_e, an integral over λ is required. Light scattering in the detector medium introduces a width to the intrinsic Cherenkov angle which causes the ring radius to be broader and therefore to illuminate a larger region of the PMT array. This broadening will affect the number of photoelectrons per hit PMT and so is partially degenerate with the PMT efficiencies. Also, as shown in Equation 4.13, the index of refraction parameter (n-1) changes proportional to the density of CO_2 in the RICH. This parameter is also included in the calibration.

In order to calibrate the Monte Carlo to the data, four parameters need to be tuned: a width related to light scattering, the Hamamatsu and Russian PMT efficiencies and the index of refraction parameter, (n-1). The tuning is achieved by comparing the data and MC occupancy of hit PMTs as a function of distance from the ring center; occupancy is defined as the number of hit PMTs as a fraction of

the total number of PMTs at a particular radius. Occupancy is therefore strongly dependent on light level.

The light scattering width, the PMT efficiency and the (n-1) calibration constants were determined using beam particles from the data with known momenta: the 30 GeV/c, 60 GeV/c and 120 GeV/c p/K/π beam. The parameters were adjusted in order to minimize the deviations between the data and the predicted occupancies. Figure 4.8 and Figure 4.9 show the result of this tuning for several beam settings. It can be seen that the prediction closely matches the data. The constants are used when calculating the expected number of photoelectrons in the log-likelihood method.
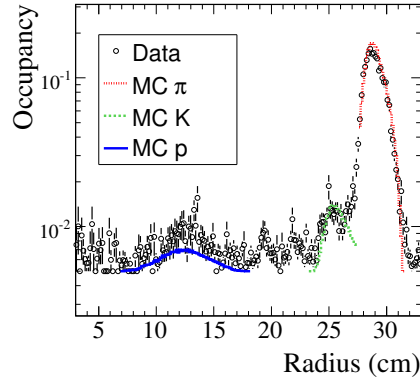
(a) 30 GeV beam
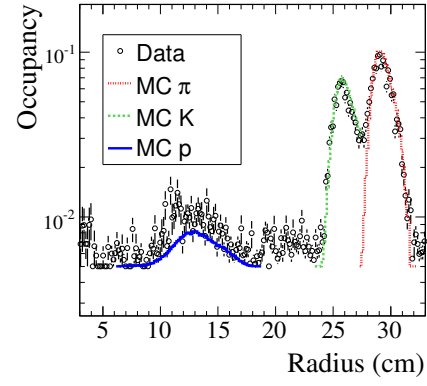
(b) 30 GeV beam
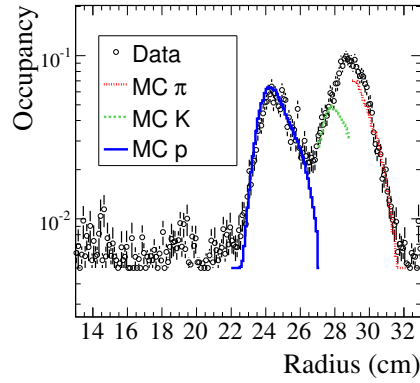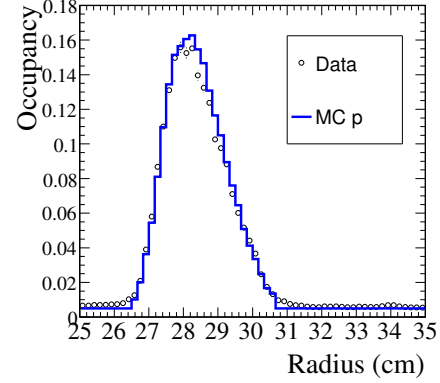
(c) 60 GeV beam

(d) 120 GeV beam

Figure 4.8: The RICH calibration for Russian PMTs.
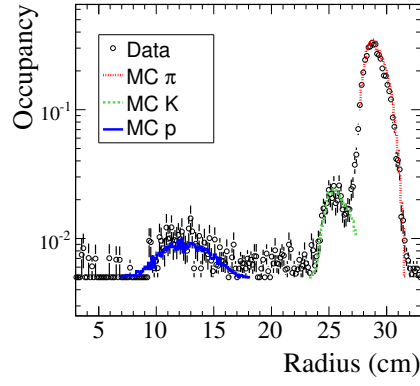
(a) 30 GeV beam
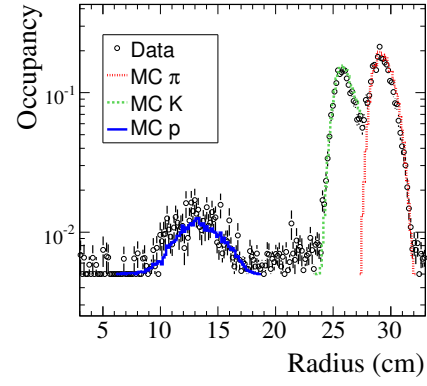
(b) 30 GeV beam
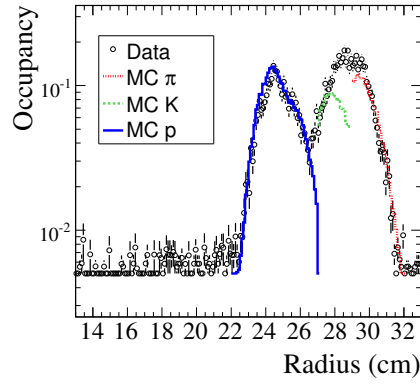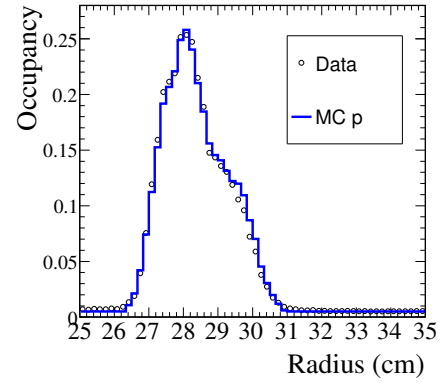
(c) 60 GeV beam

(d) 120 GeV beam

Figure 4.9: The RICH calibration for Hamamatsu PMTs.

Chapter 5

NuMI Target Analysis

This chapter describes the analysis of the NuMI target data. The goal is to measure the production ratios: π^-/π^+, K^-/K^+, K^+/π^+ and K^-/π^- above 20 GeV/c using only the tracking and RICH particle identification capabilities of the MIPP experiment. The analysis strategy and cuts employed are described and the systematic errors resulting from the approach are determined. The final results are then shown in Chapter 6.

5.1   Event Sample and Cuts

The experimental setup and the data processing procedure specific to the NuMI data analysis are described in this section. A number of cuts are applied to the data to obtain a clean sample of events. These include the beam definition, the NuMI trigger scheme, track and momentum selection, and particle classification.

5.1.1 Beam Selection and NuMI Trigger Scheme

Two event selection steps are introduced in order to clean up the event sample and to reduce the backgrounds due to the beam.

Firstly, there is a scintillation counter upstream of the NuMI target, consisting of three overlapping scintillators: solid (v_b), with a 2 mm diameter hole (v_2) and with a 6 mm diameter hole in the center (v_6), as shown in Figure 5.1. A 2 mm trigger is defined as $v_b \cap \overline{v_2} \cap \overline{v_6}$, while a 6 mm trigger is $v_b \cap v_2 \cap \overline{v_6}$. The 6 mm trigger was prescaled using hardware logic to resemble the NuMI beam in MINOS, and therefore all data with 2 mm and 6 mm triggers have been used without imposing any selection (Figure 5.2). Note that the proton beam spot size obtained from the trigger cuts in data is slightly different from the NuMI Monte Carlo simulations, (which were tuned to reflect the MINOS beam condition). This leads to a small systematic effect which will be described in Subsection 5.3.1.

Secondly, cuts on the beam position are performed. The position of the incoming beam particle is registered in three Beam Chambers. A small fraction of beam particles in the tail of the beam profile beyond $|x| > 0.45$ cm and $|y| > 0.5$ cm with respect to the beam center are cut. This corresponds to $< 0.5\%$ of the events.

5.1.2 Track Selection

The reconstructed interaction vertex is calculated for groups of tracks which are deemed to come from the same interaction. To consider an interaction vertex, it
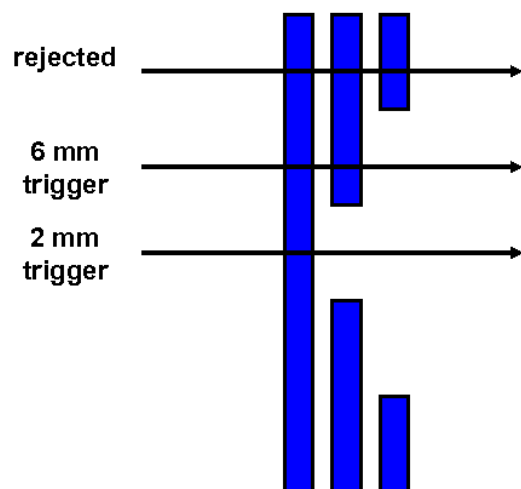
Figure 5.1: A schematic of the NuMI triggers.
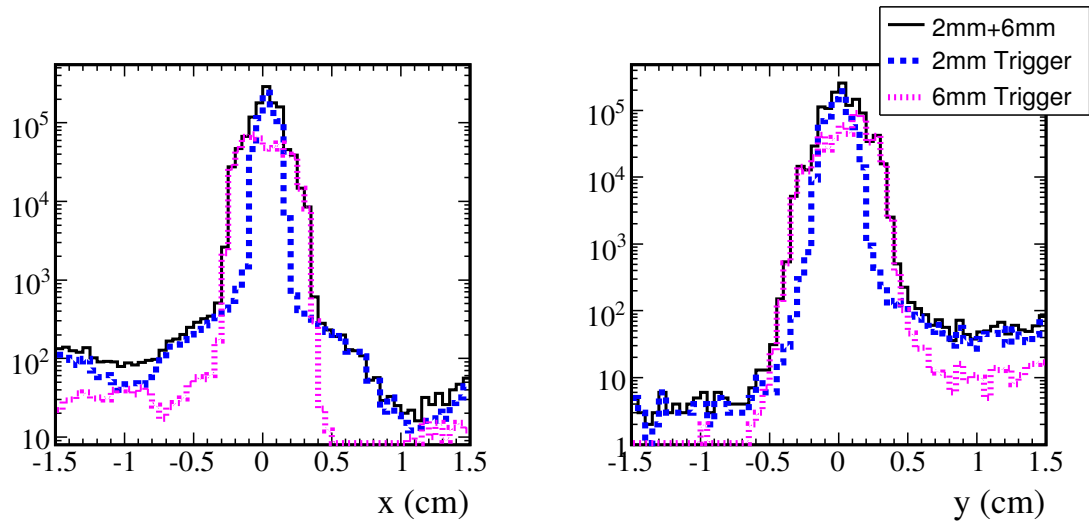
Figure 5.2: Beam positions of 2 mm and 6 mm NuMI triggers.
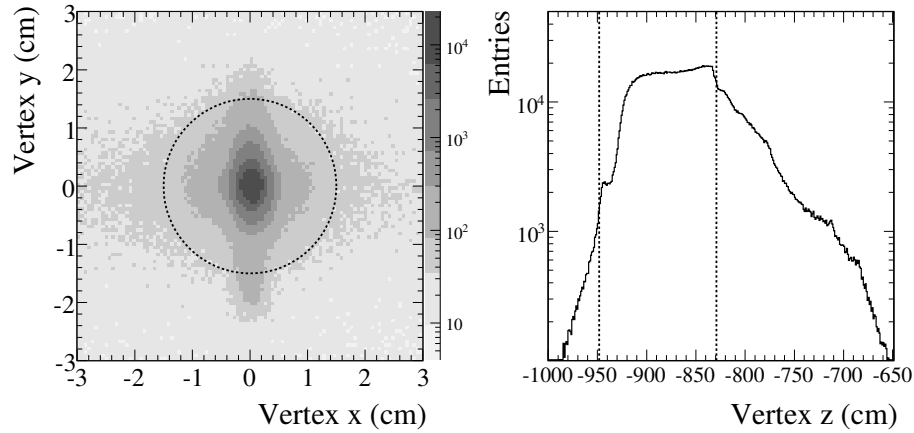
Figure 5.3: Radial and longitudinal reconstructed vertex positions for interaction vertices with ≥ 2 tracks in data. Dashed lines: cuts on vertices.

must have at least 2 tracks associated with it since vertices with only a single track typically correspond to a non-interacting proton.

Cuts are placed on the interaction vertex position to ensure that the interaction occurred within the target. Figure 5.3 shows the radial, r, and longitudinal, z, coordinates of the reconstructed vertices in data. The vertex is constrained to be in a region around the target by applying the following cuts on r and z:

- Radial: $r < 1.5$ cm, where r is relative to the axial center of the target

- Longitudinal: front of target $< z <$ end of target

5.1.3   Momentum Selection and Binning

Due to limitations imposed by the detector acceptance and by the particle iden-
tification limit of the RICH, only reconstructed particles with 20 GeV/c < p_z <
90 GeV/c and p_T < 2 GeV/c are considered. The resulting analysis phase space and
momentum binning scheme is presented in Table 5.1.

Table 5.1: Binning scheme in p_z and p_T.

Bin	$p_z (GeV/c)$	$p_T (GeV/c)$
(0, 0)	20 - 24	0 - 0.2
(0, 1)	20 - 24	0.2 - 0.4
(0, 2)	20 - 24	0.4 - 0.6
(0, 3)	20 - 24	0.6 - 1.0
(1, 0)	24 - 31	0 - 0.2
(1, 1)	24 - 31	0.2 - 0.4
(1, 2)	24 - 31	0.4 - 0.6
(1, 3)	24 - 31	0.6 - 1.0
(1, 4)	24 - 31	1.0 - 1.2
(2, 0)	31 - 42	0 - 0.2
(2, 1)	31 - 42	0.2 - 0.4
(2, 2)	31 - 42	0.4 - 0.6
(2, 3)	31 - 42	0.6 - 1.0
(2, 4)	31 - 42	1.0 - 1.55
(3, 0)	42 - 60	0 - 0.2
(3, 1)	42 - 60	0.2 - 0.4
(3, 2)	42 - 60	0.4 - 0.6
(3, 3)	42 - 60	0.6 - 1.0
(3, 4)	42 - 60	1.0 - 2.0
(4, 0)	60 - 90	0 - 0.2
(4, 1)	60 - 90	0.2 - 0.4
(4, 2)	60 - 90	0.4 - 0.6
(4, 3)	60 - 90	0.6 - 1.0
(4, 4)	60 - 90	1.0 - 2.0

5.1.4 Particle Classification

The likelihood approach for identifying π, K and p was discussed in Subsection 4.3.3. In each case a track will be identified as the particle with largest likelihood. In regions where the predicted ring radii for π, K and p are very similar (e.g. at higher momenta), the log likelihood becomes a less effective discriminator for distinguishing the different species. As a result, additional cuts have been developed to improve the selection purity.

Figure 5.4 shows the log-likelihood of π and K with respect to the log-likelihood of p for NuMI Monte Carlo events. The following log likelihood ratio cuts are used for particle classification in the data analysis:

- $R_{\pi^+p^+} > 10$, select π^+

- $R_{K^+p^+} > 35$, select K^+

- $R_{K^-p^-} > 15$, select K^-

These numbers were tuned to give the best compromise between high efficiency and high purity (i.e. large background subtraction) [described below in Subsections 5.2.1, 5.2.3 and Appendix A]. For simplicity, these cuts are momentum-independent.

To study particle identification under real experimental conditions, the log-likelihood of data and the Monte Carlo simulation are compared. These comparisons, shown in Figures 5.5, 5.6, 5.7 and 5.8, have been obtained by applying cuts on beam, trigger, position of the vertex. The RICH particle log likelihood ratio cuts listed above were
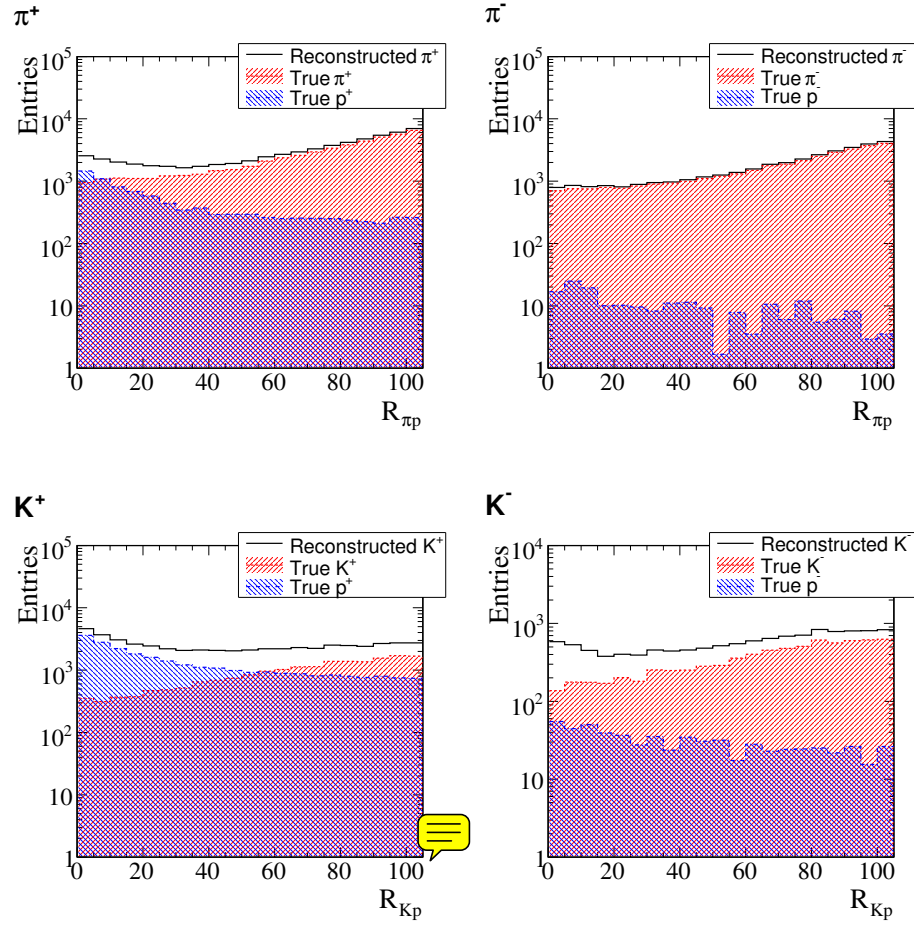
Figure 5.4: Log likelihood ratios for π^+ (upper left), π^- (upper right), K^+ (lower left) and K^- (lower right) with respect to p in Monte Carlo. Solid lines: reconstructed particle; hatched: true particles.

also used. The log-likelihood ratio of the RICH particle identification and the next largest log-likelihood is indicated in Figures 5.5, 5.6, 5.7 and 5.8. The distributions are normalized according to the maximum bins in the data. The shape agreement between data and Monte Carlo is reasonably good, although the data distributions are slightly broader than the Monte Carlo.

5.2   Evaluation of Corrections

In order to calculate production ratios, it is necessary to first extract true momentum distributions for each particle species. To do this, a series of corrections must be applied to the reconstructed data. There are several reasons for this:

- $\sim 10\%$ of secondary particles interact upstream of the RICH

- $\sim 10\%$ of particles that pass through the RICH flange (rather than the RICH front window) interact

- $\sim 10\%$ of kaons decay in flight upstream of the RICH

- Misidentification caused by the likelihood selection method

- Multiple scattering of particles upstream of the RICH leading to underestimated momenta, which in turn leads to misidentification by the likelihood selection method
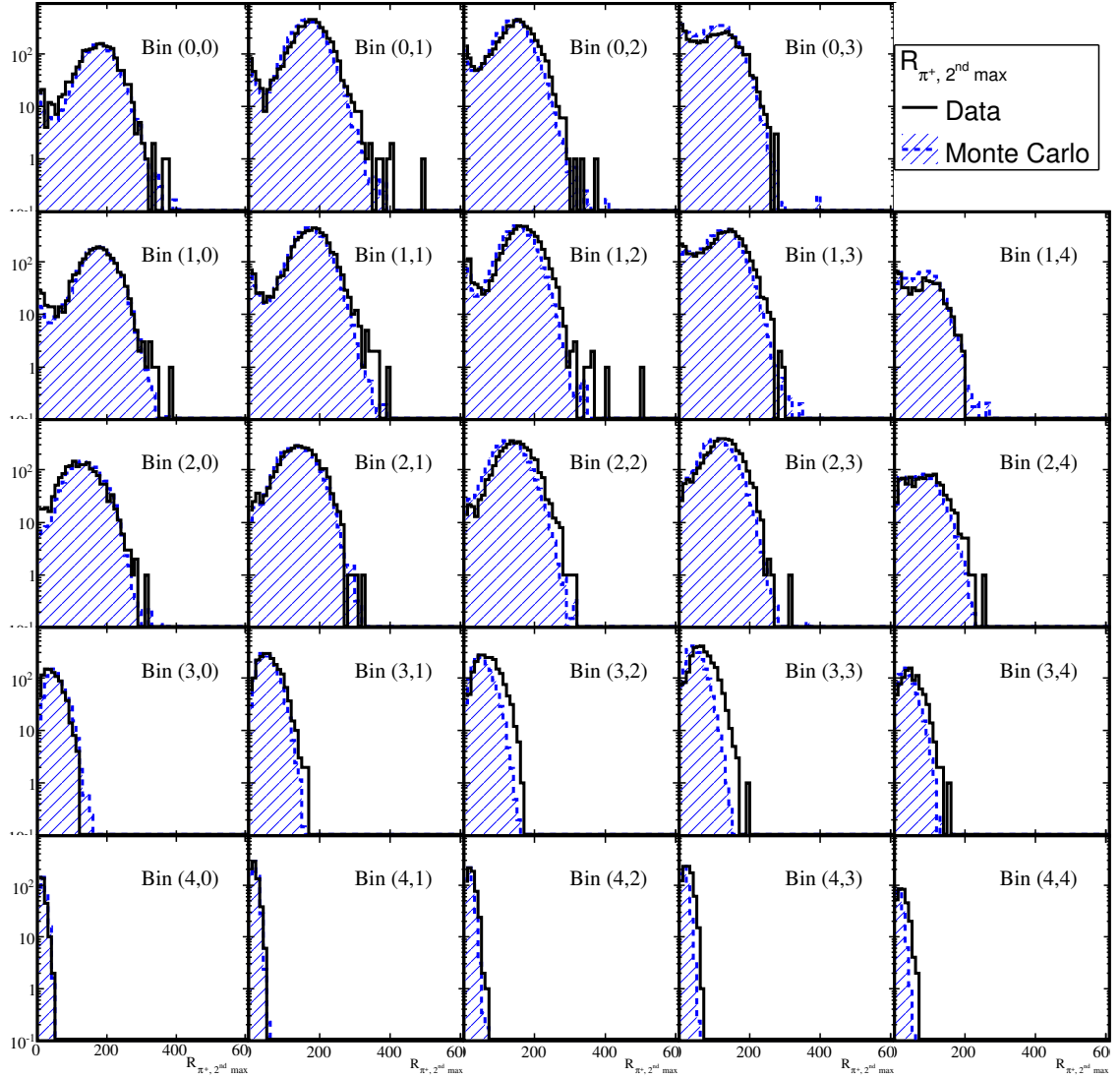
Figure 5.5: Log-likelihood ratio for reconstructed π^+ in different momentum bins. The log-likelihood ratio of reconstructed π^+ and the 2nd largest likelihood is shown. Solid lines: data; hatched: Monte Carlo simulation.
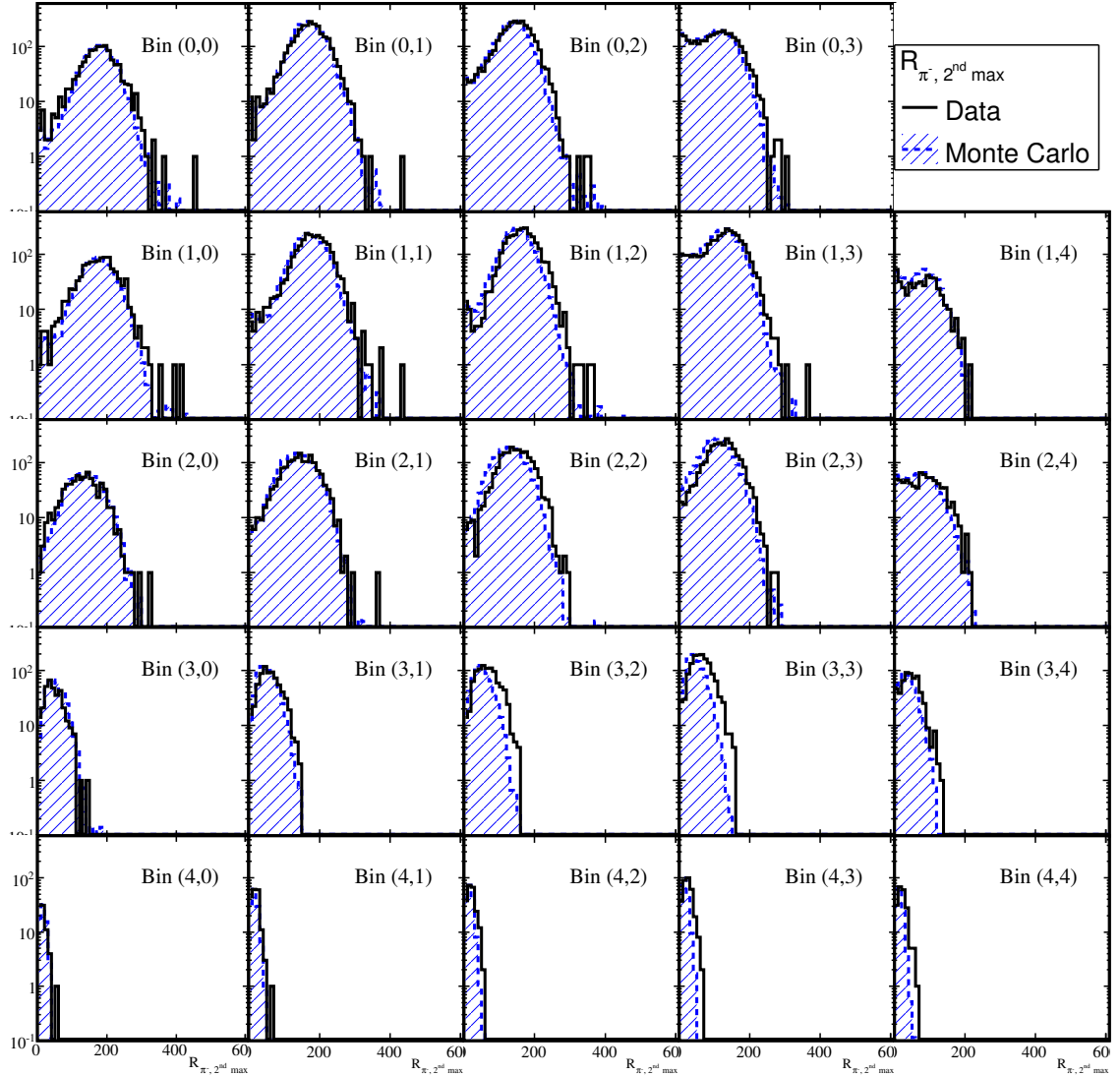
Figure 5.6: Log-likelihood ratio for reconstructed π^- in different momentum bins. The log-likelihood ratio of reconstructed π^- and the 2nd largest likelihood is shown. Solid lines: data; hatched: Monte Carlo simulation.
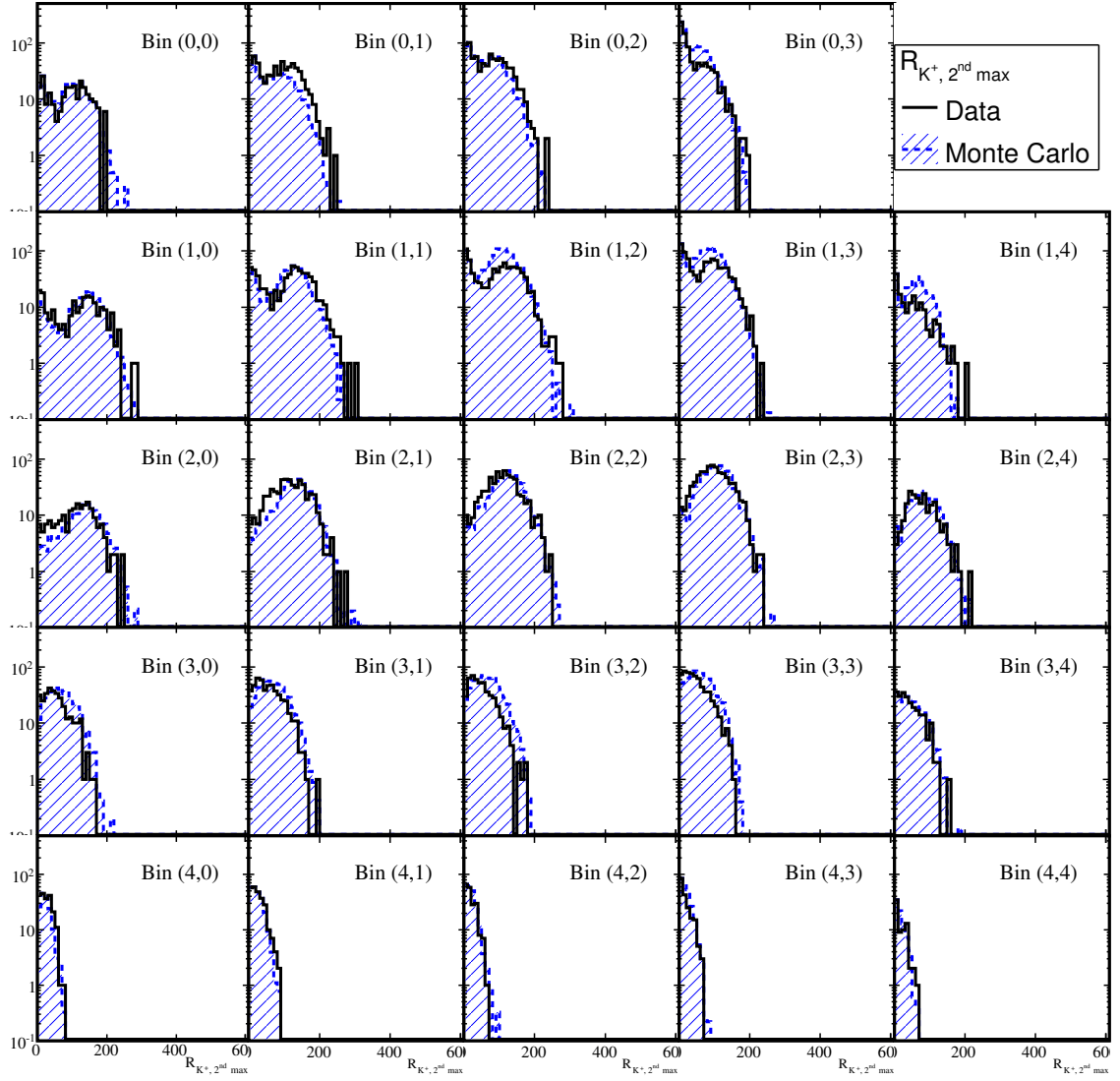
Figure 5.7: Log-likelihood ratio for reconstructed K^+ in different momentum bins. The log-likelihood ratio of reconstructed K^+ and the 2nd largest likelihood is shown. Solid lines: data; hatched: Monte Carlo simulation.
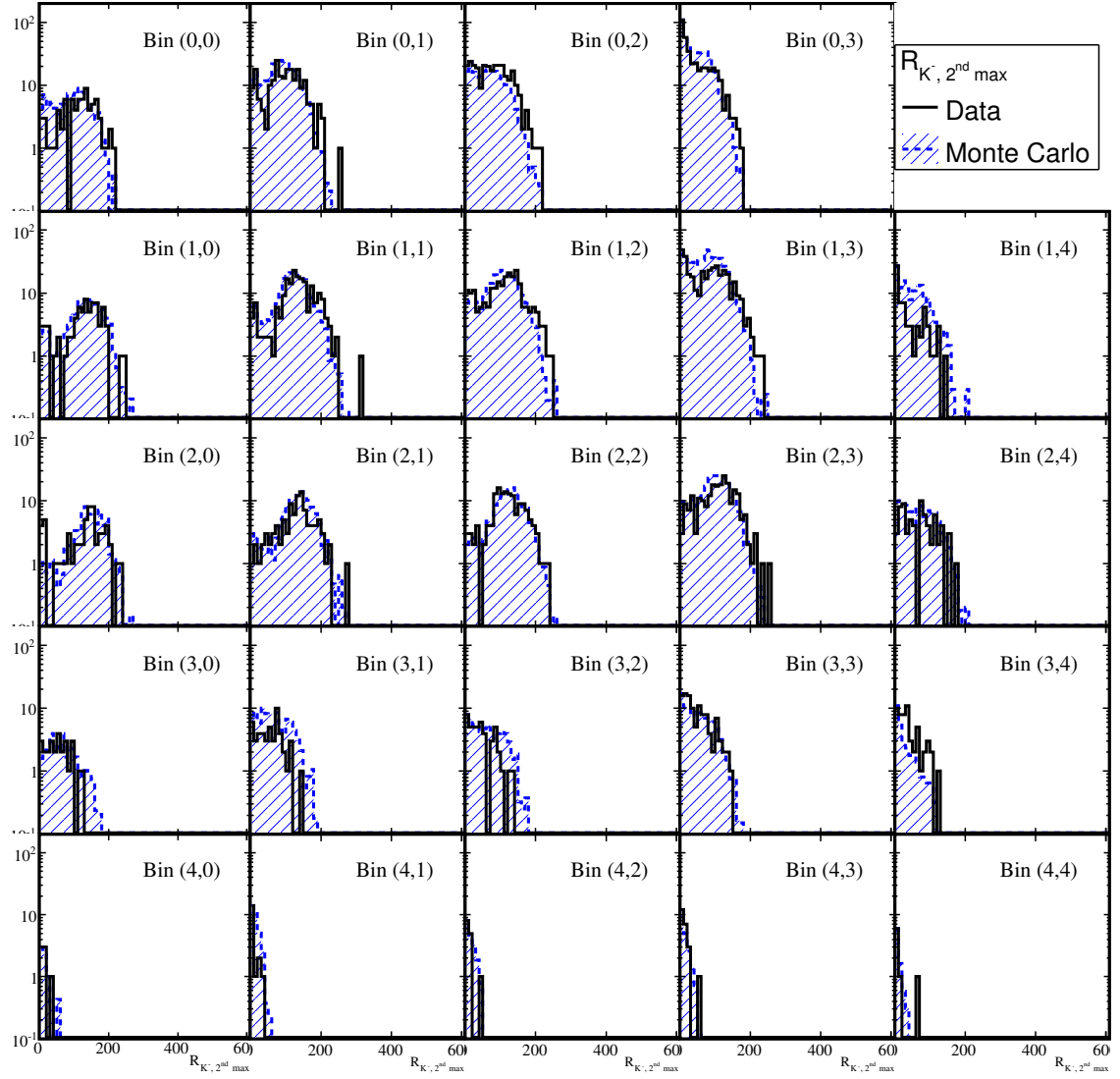
Figure 5.8: Log-likelihood ratio for reconstructed K^- in different momentum bins. The log-likelihood ratio of reconstructed K^- and the 2nd largest likelihood is shown. Solid lines: data; hatched: Monte Carlo simulation.

The Monte Carlo simulation provides a way of correcting for these effects to first order. The corrections calculated for this analysis are

1. Purity correction: subtracts background events from the selected sample.

2. Momentum correction: translates a reconstructed momentum distribution to true momentum.

3. Efficiency correction: accounts for events which are not correctly reconstructed by the algorithms.

The determination of particle identification and its derivation was discussed in Chapter 4. The cuts mentioned in Section 5.1 are applied to the sample before evaluating the correction parameters. These corrections will be described and quantified below.

5.2.1   Purity Correction

The first correction applied to data accounts for background contamination in the selected sample. The correction employs the purity as calculated from the Monte Carlo simulation and is defined as

$$\mathcal{P}_x^i = \frac{t_x^x}{t_x}$$

where t_x is the number of reconstructed x, t_x^x is the number of true x reconstructed to be x, $x = \pi^\pm, K^\pm, p^\pm$, and i denotes the reconstructed momentum bin. Figure 5.9 shows the purity versus momentum bin. The $\mathcal{P}_{\pi^\pm}^i$, $\mathcal{P}_{K^\pm}^i$ and $\mathcal{P}_{p^\pm}^i$ values themselves are the corrections applied bin-by-bin to the data.
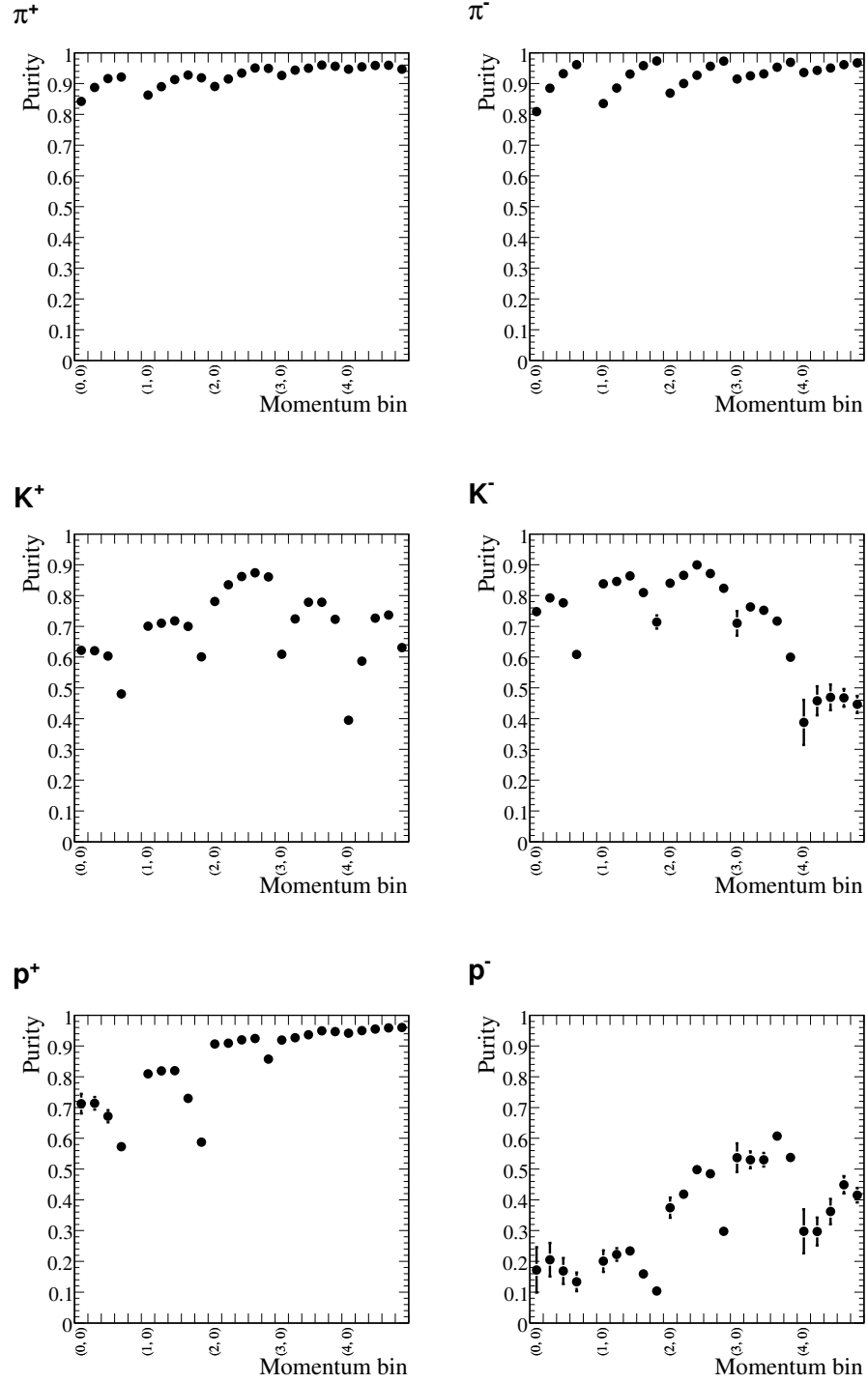
Figure 5.9: Purity of $\pi^{\pm}$, $K^{\pm}$ and $p^{\pm}$ as a function of reconstructed momentum bin (p_z, p_T).

5.2.2 Momentum Correction

The tracking and fitting procedure outlined in Section 4.2 results in a momentum resolution of ~5% for 120 GeV/c Monte Carlo protons. It is therefore necessary to unfold the reconstructed momentum distribution measured in data to true momentum distribution in order to calculate the production ratios.

This is achieved by using the Monte Carlo to calculate the probability density function (PDF) for true momentum for each bin of reconstructed momentum. In other words, the true momentum probability distribution is constructed for all particles reconstructed in a single reconstructed momentum bin. These PDF's can be represented as a matrix as shown in Figure 5.10. This matrix is used to reassign the number of events in each reconstructed momentum bin into a range of true bins. The result is a prediction of the true momentum distribution.

This can be summarized mathematically as follows

$$B^j = \sum_{i=1}^{nbins} \mathcal{M}_x^{ij} b^i$$

$$\sum_{j=1}^{nbins} \mathcal{M}_x^{ij} = 1$$

where B^i = number of events in true bin i, b^j = number of events in reconstructed bin j, and $\mathcal{M}_x^{ij}$ is the number of x to assigned to true momentum bin j for each event observed in reconstructed momentum bin i. Note that $\mathcal{M}$ is the matrix shown in Figure 5.10. It can be seen that the matrix has only very small non-diagonal elements, reflecting the fact that the momentum resolution is small compared to the

bin sizes chosen for the analysis.

5.2.3 Efficiency Correction

The identification efficiency of x is defined as

$$\mathcal{E}_x^j = \frac{t_x^x}{T_x}$$

where T_x is the number of true x in the Monte Carlo simulation. This is defined per true momentum bin j and is shown in Figure 5.11. The efficiency correction applied bin-by-bin to the data is then $1/\mathcal{E}$.

5.2.4 Application of Corrections

After obtaining the correction factors from the Monte Carlo simulation as described in the previous sections, these can then be applied to the reconstructed momentum distributions from data. Define n_x^i to be the number of reconstructed x in reconstructed momentum bin i and N_x^j to be the predicted number of true x in true momentum bin j, obtained by applying the correction factors. Then,

$$N_x^j = \sum_{i=1}^{nbins} \frac{\mathcal{P}_x^i}{\mathcal{E}_x^j} \mathcal{M}_x^{ij} n_x^i$$

5.2.5 Background Estimation from Data

So far, the Monte Carlo has been used to estimate these backgrounds and inefficiencies. However, a major problem with this determination lies in the discrepancy
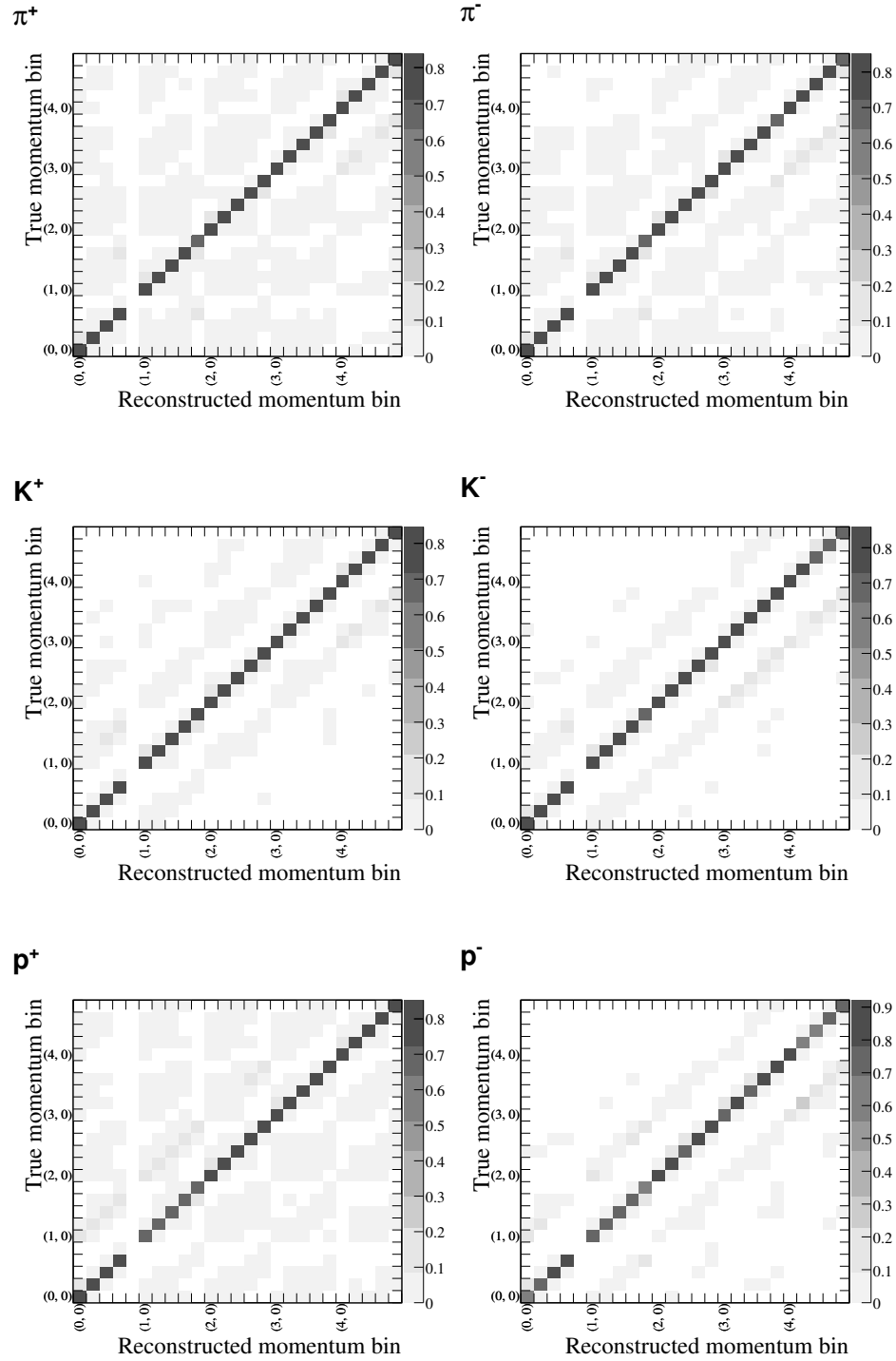
Figure 5.10: Momentum correction factors of $\pi^\pm$, $K^\pm$ and $p^\pm$ as a function of true momentum bin versus reconstructed momentum bin. The shaded areas indicate the probability that a reconstructed momentum bin falls into the corresponding true momentum bin.
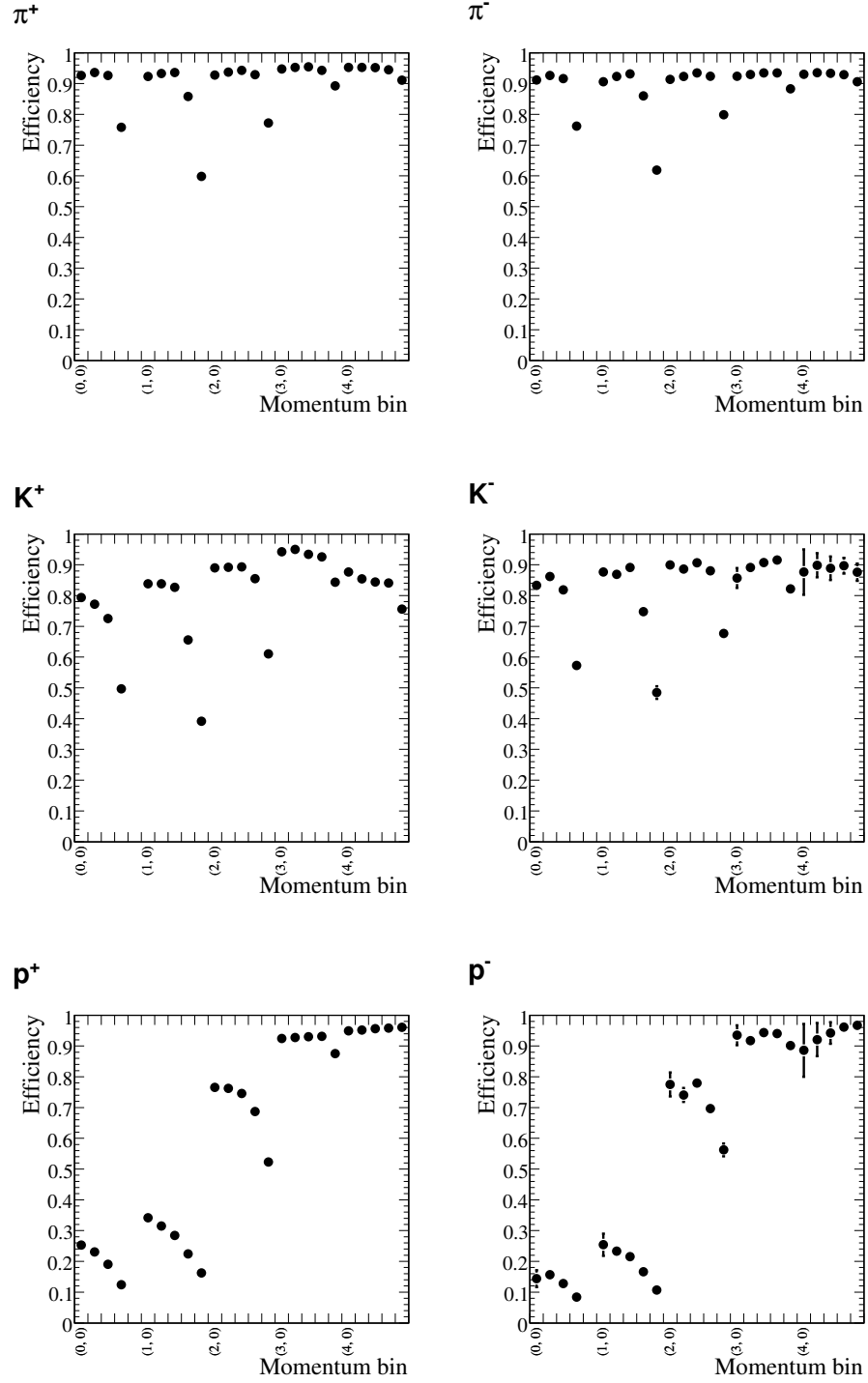
Figure 5.11: Efficiency of $\pi^{\pm}$, $K^{\pm}$ and $p^{\pm}$ selection as a function of true momentum bin (p_z, p_T).

between the data and the Monte Carlo simulation. In order to improve the accuracy of the Monte Carlo simulation, an iterative, data-driven approach is adopted. Define a yield for each particle species and each true momentum bin; for example, f_{π^+} for π^+ is given by

$$f_{\pi^+} = \frac{N_{\pi^+}}{N_{\pi^+} + N_{K^+} + N_{p^+}}$$

where N_{x^+} is the predicted number of true x^+ obtained by applying the corrections to the data. Similarly, the yield F_{π^+} for π^+ is extracted from the Monte Carlo truth information

$$F_{\pi^+} = \frac{T_{\pi^+}}{T_{\pi^+} + T_{K^+} + T_{p^+}}$$

where T_{x^+} is the true number of x^+ in the Monte Carlo simulation. Note that for π^-, K^- and p^-, the denominator is the sum of the negative N_{x^-} or T_{x^-}. Figure 5.12 shows $f_{\pi^\pm}$, $f_{K^\pm}$, $f_{p^\pm}$ in solid lines and $F_{\pi^\pm}$, $F_{K^\pm}$, and $F_{p^\pm}$ in dashed lines before iteration.

The data/MC yield ratio, $w_j = f_j/F_j$, for particle j is then obtained and used to adjust the Monte Carlo simulation. The yields have no effect on the selection efficiency, and so this tuning only concerns the selection purity.

After weighting each Monte Carlo particle according to the calculated w_j, the purity correction is recalculated as described in Subsection 5.2.1. The new purity correction, which represents a new mixing scheme between different particle species, is used to calculate new yields from the data and thus new yield ratios.

The evolution of the iteration and the resulting yield ratios are shown in Figure 5.13, where the ratio is shown as a function of momentum bin (p_z, p_T) for 7
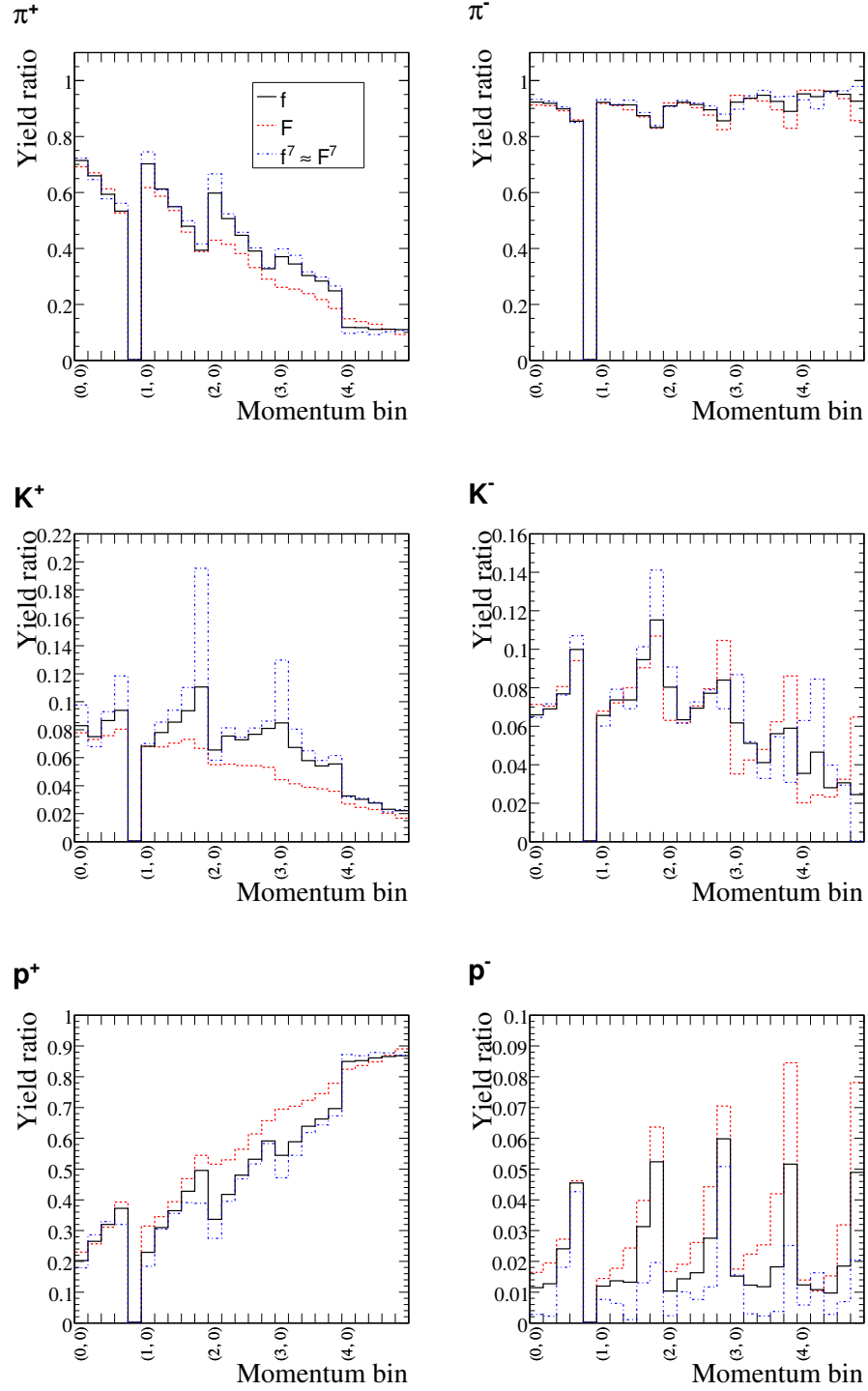
Figure 5.12: Yield for each particle species in data ($f_{\pi^\pm}$, $f_{K^\pm}$, $f_{p^\pm}$) and in Monte Carlo ($F_{\pi^\pm}$, $F_{K^\pm}$, and $F_{p^\pm}$). Solid lines: data; dashed lines: Monte Carlo without iteration; dot-dashed lines: Monte Carlo after 7th iteration.

iterations. The yield ratios come to stable values and approach 1. The yield values after the 7th iteration, $f_{x\pm}^7 (\cong F_{x\pm}^7)$, are shown as dot-dashed lines in Figure 5.12. The final values are closer but not identical to the original data, reflecting the iterative nature of the procedure. In most cases, the yields are driven beyond the original data values.

Figure 5.14 shows the effect of this background tuning on the purity correction as a function of reconstructed momentum bin (p_z, p_T) for 7 iterations. Overall, the purity is increased for $\pi^\pm$ and $K^\pm$, while the purity for protons decreases on average.

The result of the Monte Carlo tuning on the reconstructed spectrum can be seen in Figure 5.15. The data and Monte Carlo distributions are normalized to each other by area. The total χ^2 between the data and the Monte Carlo for all particles before tuning is 6192.06 and after tuning is 4490.72. In general, therefore, the agreement improves after the iteration stage. That is to say the Monte Carlo weighting factors derived from comparisons of the bin-by-bin truth ratios are able to improve agreement at the reconstructed level. It is clear however, that the current Monte Carlo implementation of the experiment is not sufficient to perfectly describe the data: convergence at the truth level does not lead to convergence at the reconstructed level. In particular, although most of the particle species do show improved agreement, the π^+ is somewhat poorer after the iteration, as can be seen from the $\chi 2$ breakdowns in Table 5.2. The remaining discrepancies will therefore have to be accounted for by a systematic error.
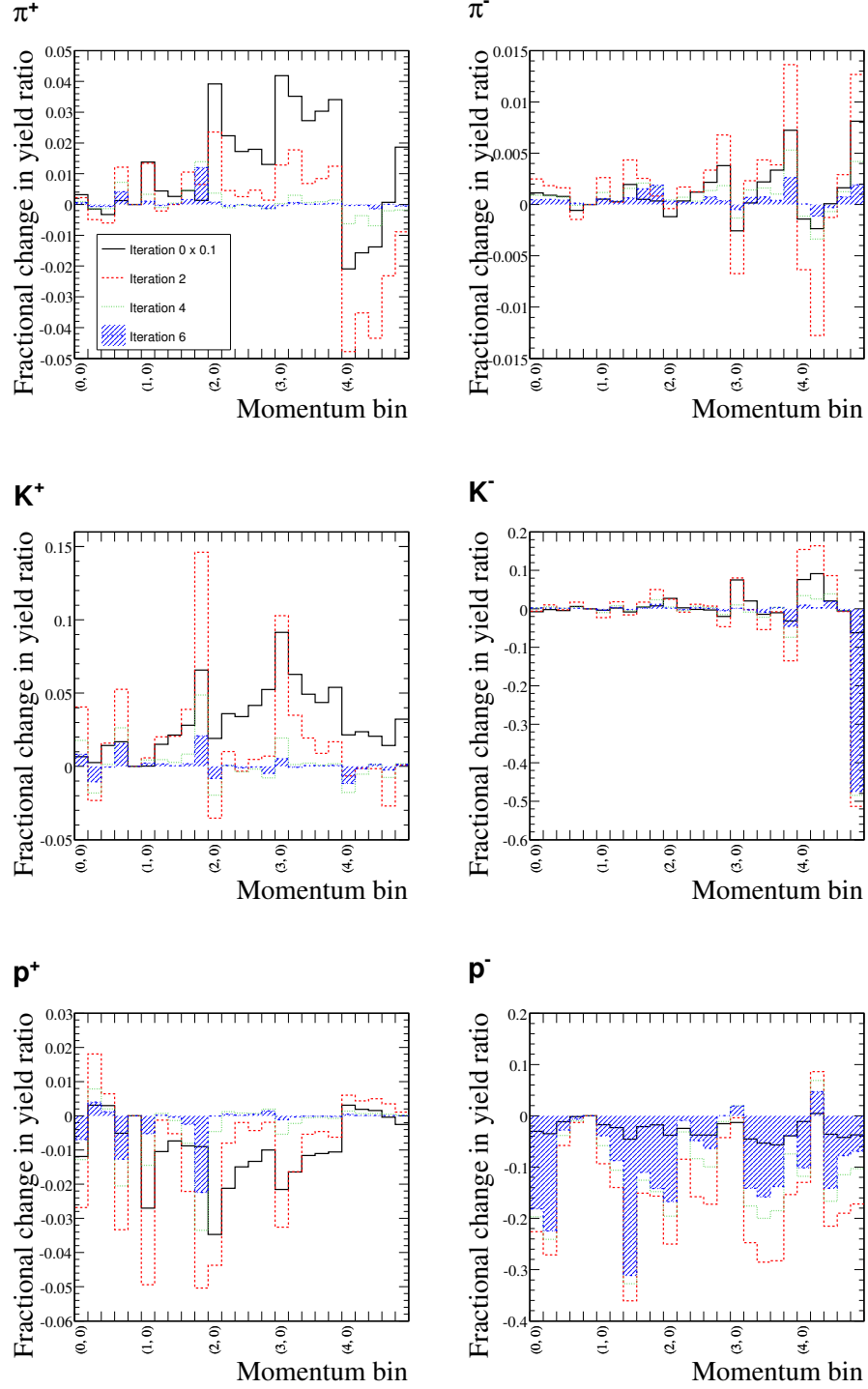
Figure 5.13: Effect of background subtraction on fractional change in yield ratio. The fractional change in yield ratio $(w_j^{k+1} - w_j^k)/w_j^k$ between iterations k and $k+1$ for 7 iterations is shown.
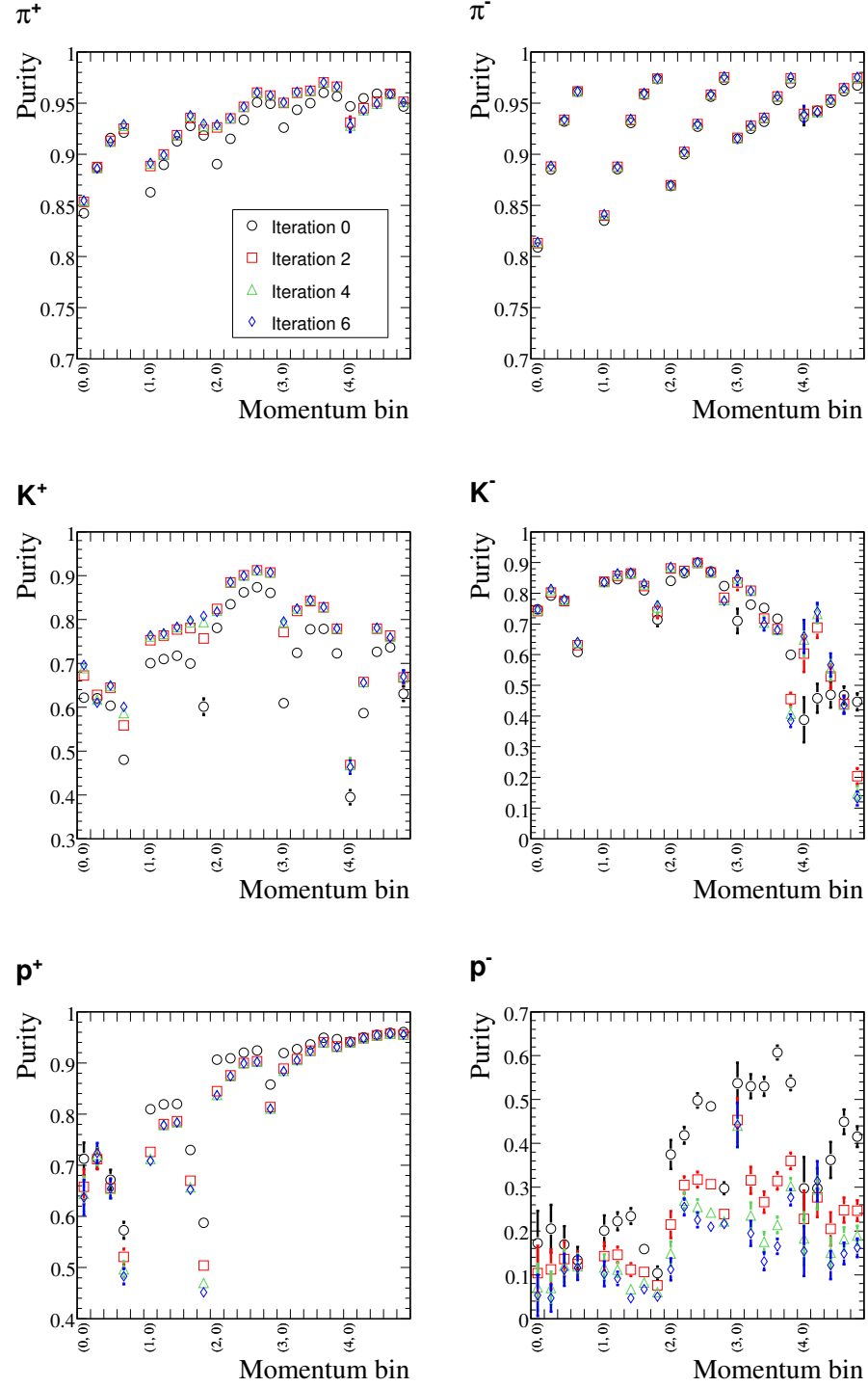
Figure 5.14: Effect of Monte Carlo event weighting on purity correction factor for 7 iterations.
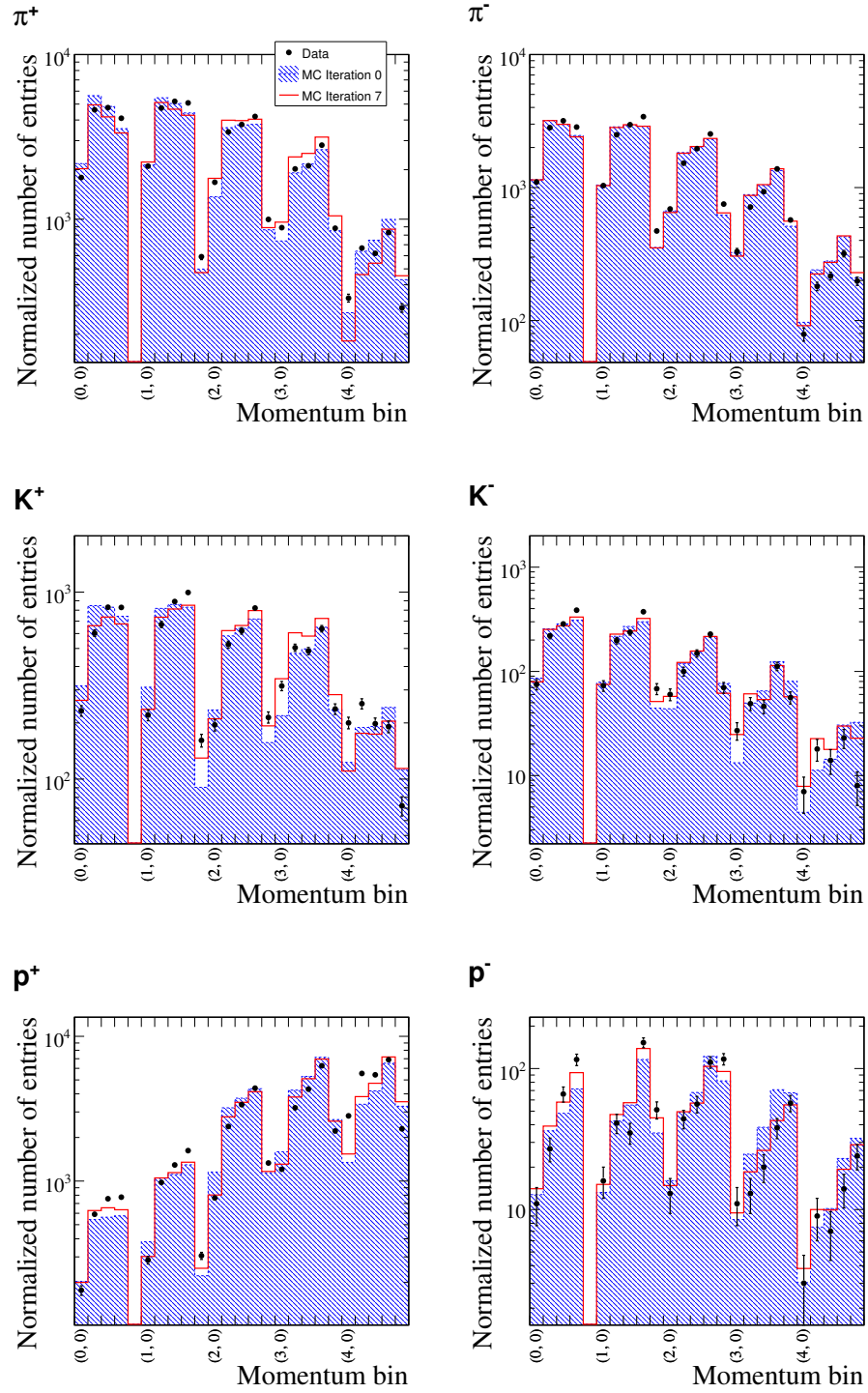
Figure 5.15: Normalized number of entries for $\pi^{\pm}$, $K^{\pm}$ and $p^{\pm}$ as a function of momentum bin. Points: data; hatched: Monte Carlo simulation with no iteration; solid lines: Monte Carlo simulation after 7 iterations.

Table 5.2: The $\chi 2$ between data and Monte Carlo for $\pi^{\pm}$, $K^{\pm}$ and $p^{\pm}$ before and after iteration.

Particle	Before Iteration	After Iteration
π^+	915.06	1109.29
π^-	526.26	500.59
K^+	423.79	270.77
K^-	169.51	73.02
p^+	4022.47	2492.96
p^-	134.97	44.09
Sum	6192.06	4490.72

5.3   Systematic Errors

The effect of systematics errors on the π^-/π^+, K^-/K^+ and $K^{\pm}/\pi^{\pm}$ ratios have been calculated using the Monte Carlo simulation. An estimation of systematic errors induced by

- Beam tuning

- Momentum bias

- Background subtraction

are discussed in this section. The total systematic errors are then obtained by quadratic summation of the individual errors from each source.

5.3.1   Beam Systematic Error

The goal of this study is to estimate the changes in the production ratio due to small changes in the proton beam profile. This is motivated by observed differ-

ences between the data and Monte Carlo beam widths. The beam systematic error is obtained by artificially increasing/decreasing the width of the beam after beam selection. Figure 5.16 shows the reconstructed beam positions in data and Monte Carlo; the Monte Carlo was generated with the same beam profile as the NuMI beam in MINOS. The difference in beam width between the MIPP data and the Monte Carlo simulation is noticeable: the Monte Carlo simulation has a wider beam

$$\Delta\sigma_{x_{beam}} = \sigma^{MC}_{x_{beam}} - \sigma^{data}_{x_{beam}} = 0.1 \ mm \text{ and } \Delta\sigma y_{beam} = \sigma^{MC}_{y_{beam}} - \sigma^{data}_{y_{beam}} = 0.2 \ mm.$$
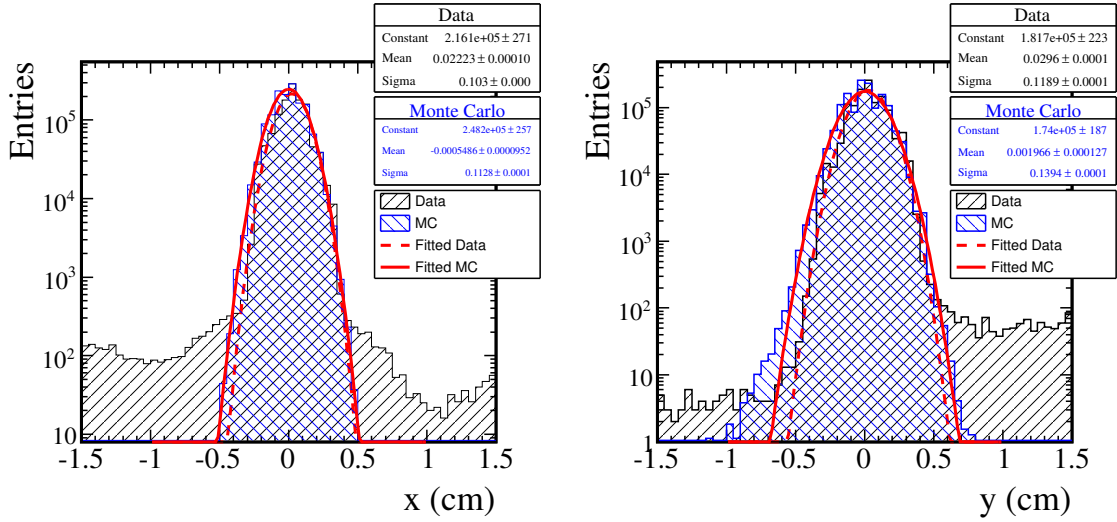
Figure 5.16: Reconstructed beam positions and their Gaussian fits in data and Monte Carlo simulation. Hatched: data and Monte Carlo simulation; dotted lines: Gaussian fit of data; solid lines: Gaussian fit of MC.

These values are used to reweight the Monte Carlo to investigate the effect of a wider/narrower beam. The resulting effects are shown in Figure 5.17 as a function of momentum bin (p_z, p_T) for ratios π^+/π^-, K^+/K^-, K^+/π^+ and K^-/π^-. The systematic effect due to beam width variation on the ratios is very small, $< 4\%$ in

general.
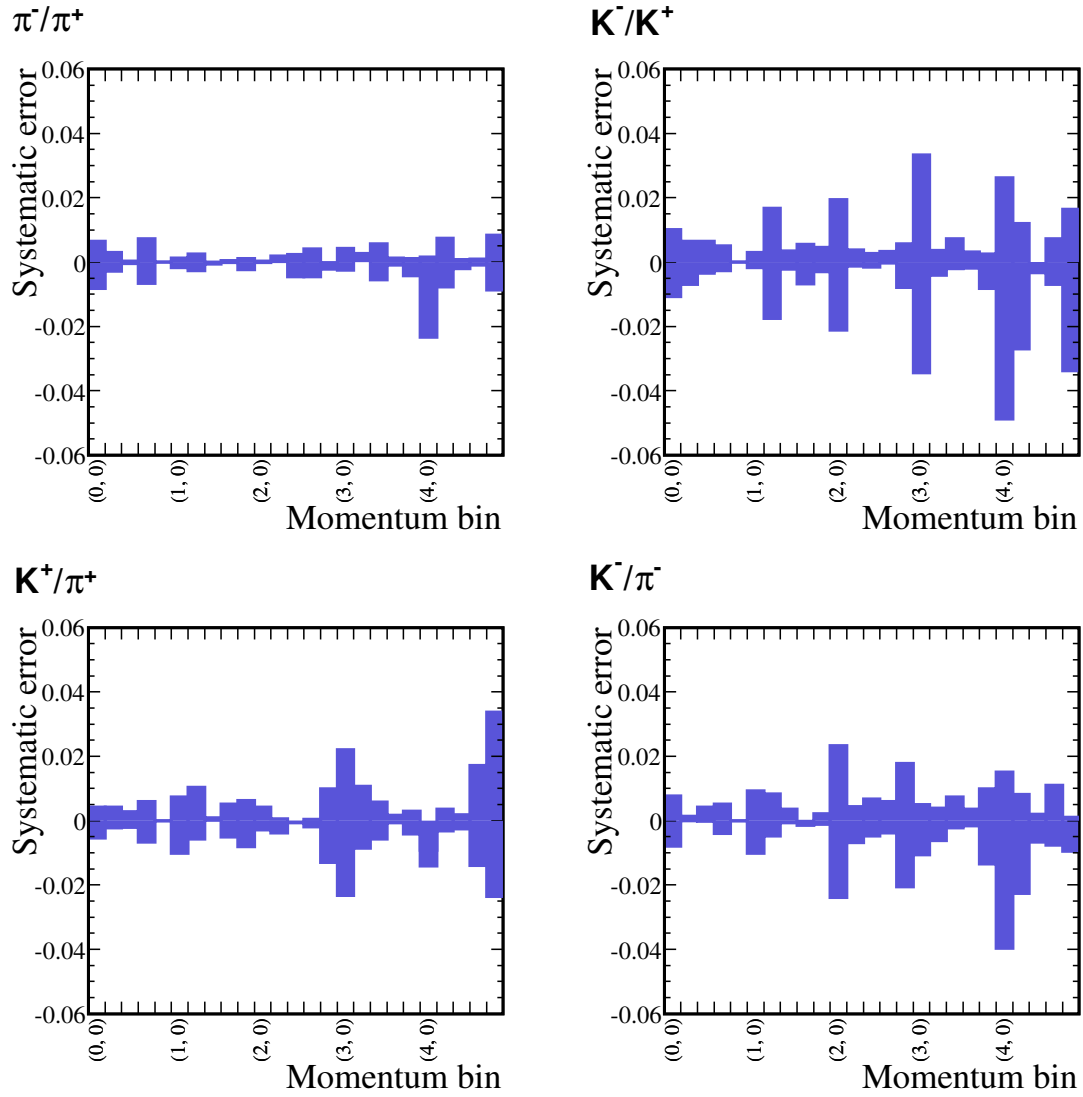
Figure 5.17: Effect of beam systematic on π^+/π^- (upper left), K^+/K^- (upper right), K^+/π^+ (lower left) and K^-/π^- (lower right) due to $\Delta\sigma_{x_{beam}} = \pm 0.1$ mm and $\Delta\sigma_{y_{beam}} = \pm 0.2$ mm.

5.3.2 Momentum Systematic Error

The derivation in Subsection 5.2.2 is calculated using the Monte Carlo simulation and therefore does not taken into account differences between the measured reconstructed momentum in the experimental data and the Monte Carlo. As illustrated in Figure 5.18, the average reconstructed momentum in data is actually smaller than in the Monte Carlo simulation for the 120 GeV/c proton beam by about 3%. This observation is used to define the size of momentum bias to use in the systematic error study. A Monte Carlo sample is re-assigned a biased reconstructed momentum, shifted by $\pm 3\%$ from the original values. This sample is then treated like data and used along with corrections calculated from the standard Monte Carlo to calculate the production ratios.
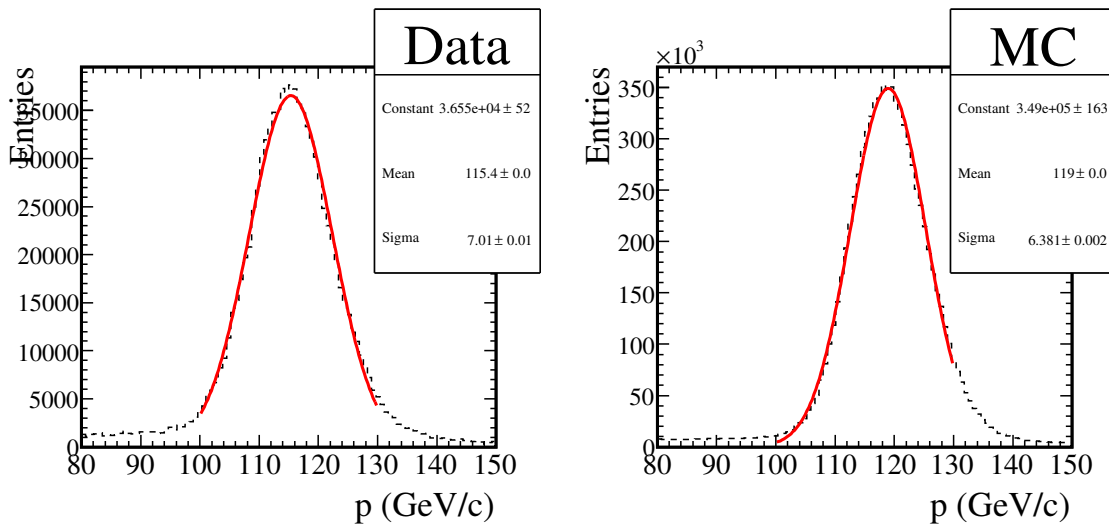
Figure 5.18: Reconstructed momentum and its corresponding Gaussian fit in data (left) and Monte Carlo simulation (right) for 120 GeV/c proton beam. Dotted lines: reconstructed momentum; solid lines: Gaussian fit.

The resulting effects are shown in Figure 5.19 for ratios π^+/π^-, K^+/K^-, K^+/π^+ and K^-/π^- as a function of (p_z, p_T), by applying a systematic of $\Delta p_z = \pm 3\%$ and $\Delta p_T = \pm 3\%$. The typical effects stay below the $\pm 5\%$ limit, with at most 15% effect on a bin per bin basis.
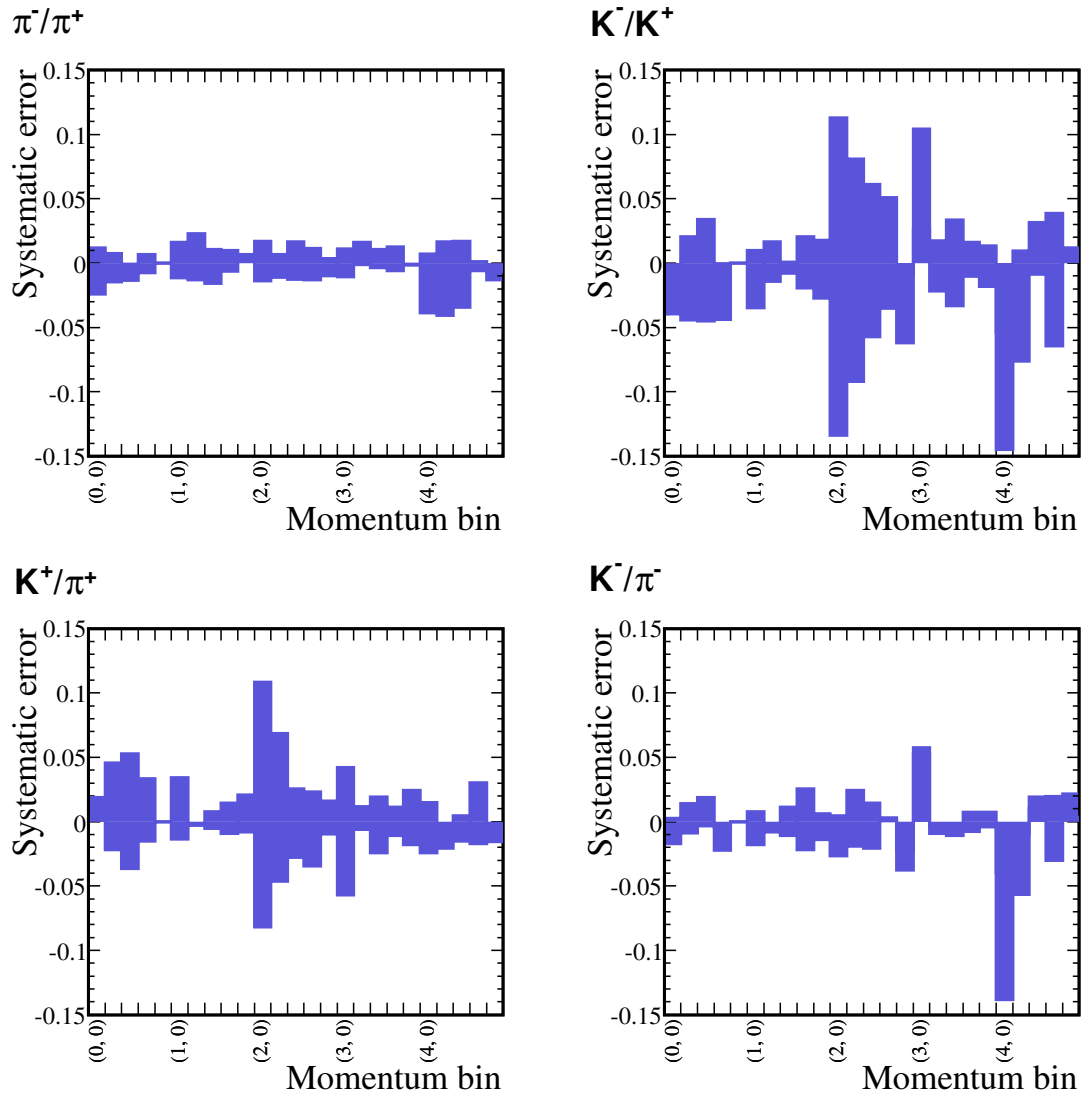
Figure 5.19: Effect of momentum systematic on π^+/π^- (upper left), K^+/K^- (upper right), K^+/π^+ (lower left) and K^-/π^- (lower right) due to $\Delta p_z = \pm 3\%$ and $\Delta p_T = \pm 3\%$.

5.3.3   Background Systematic Error

The main systematic error is expected to come from the background subtraction. The systematic uncertainty introduced through background subtraction depends on the log-likelihood ratio cuts and the number of background subtraction iterations shown in Subsection 5.2.5. In Subsection 5.2.5, the true number of Monte Carlo particles are reweighted to ensure that the true particle yields agree with the data predictions.

To estimate the systematic error after iterations, the remaining differences between the data and the Monte Carlo simulation are treated as the systematic error on the background events in each bin. The purities and the ratios are then recomputed based on the maximum and minimum allowed number of background events. The effect of this study is demonstrated in Figure 5.20, which shows the background systematic error as a function of momentum bin (p_z, p_T).
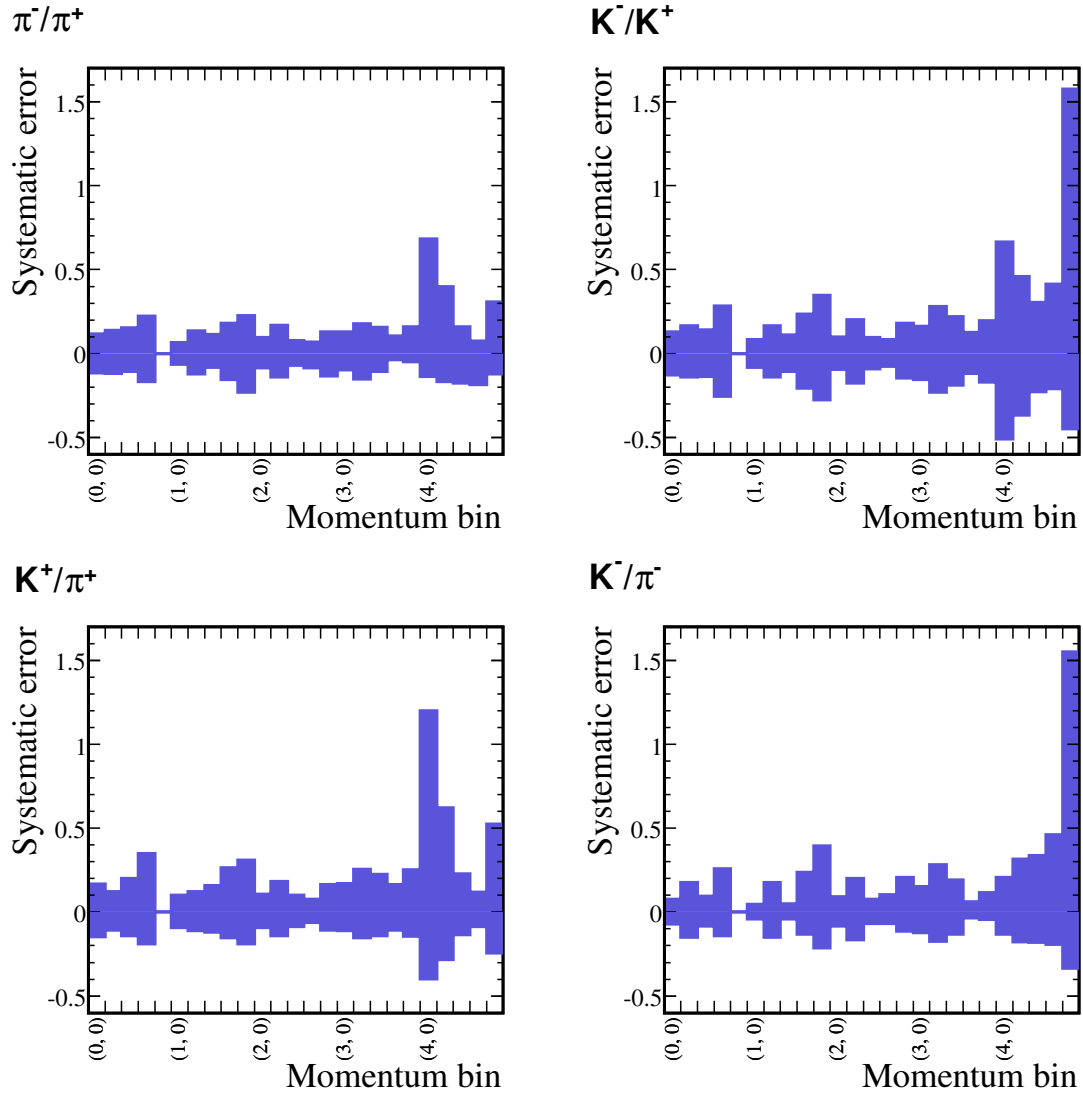
Figure 5.20: Effect of background systematic on π^+/π^-, K^+/K^-, K^+/π^+ and K^-/π^-.

Chapter 6

Results and Comparison

The set of π^-/π^+, K^-/K^+, $K^\pm/\pi^\pm$ ratios obtained from the data analysis and correction procedures described in Chapter 5 is shown in this chapter as a function of momentum bin (p_z, p_T). This chapter also summarizes the numerical results from the MIPP NuMI target data in tables, gives a set of distributions as a function of momentum bin (p_z, p_T), and shows the comparison to the MIPP Monte Carlo simulation, the MIPP thin Carbon data and the MINOS models.

6.1 Measurements of Particle Production Ratios from the NuMI Target

Table 6.1, Table 6.2, Table 6.3 and Table 6.4 present the π^-/π^+, K^-/K^+, K^+/π^+ and K^-/π^- ratios respectively. They correspond to the binning scheme discussed in

Table 5.1 in Chapter 5.

The distributions of the ratios in (p_z, p_T) are shown in Figure 6.1.
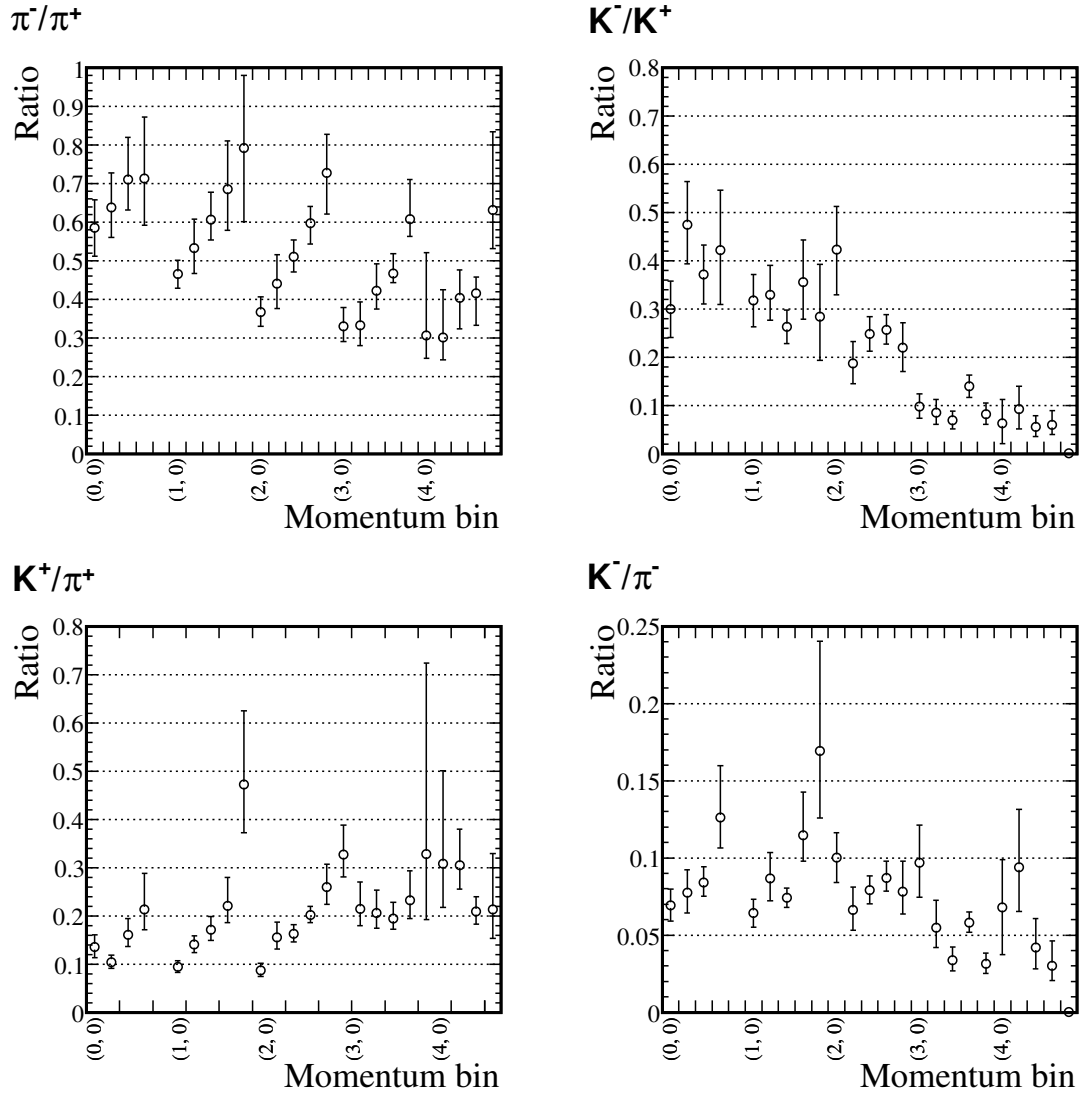
Figure 6.1: The ratios as a function of (p_z, p_T) for π^-/π^+, K^-/K^+ and $K^\pm/\pi^\pm$ produced in p+NuMI collisions at 120 GeV/c.

These ratios form an internally consistent ensemble that reveals structures of transverse and longitudinal momentum dependencies in the available phase space.

Table 6.1: The π^-/π^+ ratio in p+NuMI interactions in (p_z, p_T) at 120 GeV/c. The statistical and systematic uncertainties are given.

| Bin | π^-/π^+ | Statistical | Errors in percent | | | |
			Total Systematic	Beam	Momentum	Background
(0, 0)	$0.585^{+0.073}_{-0.073}$	4.111	$+11.719$ -11.802	$+0.642$ -0.823	$+1.170$ -2.427	$+11.643$ -11.521
(0, 1)	$0.638^{+0.089}_{-0.078}$	2.531	$+13.759$ -11.975	$+0.296$ -0.278	$+0.750$ -1.454	$+13.736$ -11.883
(0, 2)	$0.710^{+0.109}_{-0.079}$	2.461	$+15.218$ -10.807	$+0.024$ -0.044	$+0.000$ -1.328	$+15.218$ -10.725
(0, 3)	$0.713^{+0.160}_{-0.121}$	2.669	$+22.240$ -16.792	$+0.722$ -0.671	$+0.665$ -0.746	$+22.219$ -16.762
(1, 0)	$0.465^{+0.037}_{-0.036}$	3.890	$+6.817$ -6.625	$+0.121$ -0.177	$+1.607$ -1.143	$+6.624$ -6.523
(1, 1)	$0.533^{+0.075}_{-0.067}$	2.507	$+13.865$ -12.260	$+0.253$ -0.267	$+2.300$ -1.294	$+13.670$ -12.189
(1, 2)	$0.607^{+0.071}_{-0.052}$	2.322	$+11.457$ -8.296	$+0.004$ -0.060	$+1.052$ -1.575	$+11.408$ -8.145
(1, 3)	$0.685^{+0.125}_{-0.107}$	2.261	$+18.135$ -15.418	$+0.045$ -0.020	$+0.974$ -0.644	$+18.109$ -15.404
(1, 4)	$0.793^{+0.188}_{-0.192}$	7.088	$+22.617$ -23.159	$+0.104$ -0.233	$+0.680$ 0.000	$+22.606$ -23.158
(2, 0)	$0.366^{+0.039}_{-0.036}$	4.606	$+9.743$ -8.793	$+0.035$ -0.019	$+1.703$ -1.377	$+9.593$ -8.684
(2, 1)	$0.440^{+0.075}_{-0.064}$	3.080	$+16.774$ -14.109	$+0.189$ 0.000	$+0.670$ -1.116	$+16.760$ -14.065
(2, 2)	$0.510^{+0.043}_{-0.039}$	2.805	$+7.939$ -7.148	$+0.243$ -0.454	$+1.663$ -1.273	$+7.760$ -7.019
(2, 3)	$0.597^{+0.045}_{-0.054}$	2.534	$+7.028$ -8.666	$+0.409$ -0.452	$+1.148$ -1.309	$+6.922$ -8.554
(2, 4)	$0.727^{+0.100}_{-0.106}$	5.157	$+12.807$ -13.582	$+0.000$ -0.215	$+0.370$ -0.984	$+12.802$ -13.544
(3, 0)	$0.330^{+0.048}_{-0.039}$	6.556	$+12.955$ -9.890	$+0.417$ -0.247	$+1.091$ -1.081	$+12.902$ -9.828
(3, 1)	$0.333^{+0.061}_{-0.053}$	4.293	$+17.697$ -15.236	$+0.266$ 0.000	$+1.610$ -0.103	$+17.622$ -15.236
(3, 2)	$0.423^{+0.069}_{-0.048}$	3.903	$+15.820$ -10.704	$+0.571$ -0.549	$+1.062$ -0.374	$+15.774$ -10.683
(3, 3)	$0.467^{+0.051}_{-0.024}$	3.301	$+10.506$ -3.917	$+0.133$ -0.098	$+1.274$ -0.610	$+10.428$ -3.868
(3, 4)	$0.608^{+0.102}_{-0.045}$	5.527	$+15.832$ -4.844	$+0.112$ -0.428	$+0.000$ -0.150	$+15.832$ -4.823
(4, 0)	$0.307^{+0.214}_{-0.060}$	12.837	$+68.398$ -14.540	$+0.164$ -2.336	$+0.704$ -3.851	$+68.394$ -13.825
(4, 1)	$0.301^{+0.123}_{-0.058}$	8.637	$+39.962$ -17.373	$+0.737$ -0.779	$+1.667$ -4.074	$+39.920$ -16.871
(4, 2)	$0.403^{+0.073}_{-0.080}$	8.099	$+16.155$ -18.023	$+0.077$ -0.205	$+1.693$ -3.419	$+16.066$ -17.695
(4, 3)	$0.416^{+0.042}_{-0.082}$	6.735	$+7.433$ -18.625	$+0.086$ -0.091	$+0.101$ -0.594	$+7.431$ -18.615
(4, 4)	$0.631^{+0.204}_{-0.099}$	9.843	$+30.740$ -12.313	$+0.840$ -0.863	$+0.000$ -1.321	$+30.728$ -12.211

Table 6.2: The K^-/K^+ ratio in p+NuMI interactions in (p_z, p_T) at 120 GeV/c. The statistical and systematic uncertainties are given.

Bin	K^-/K^+	Statistical	Total Systematic	Beam	Momentum	Background
			Errors in percent			
(0, 0)	$0.299^{+0.058}_{-0.058}$	14.250	$+13.092$ -13.346	$+1.003$ -1.079	$+0.000$ -3.950	$+13.053$ -12.702
(0, 1)	$0.474^{+0.089}_{-0.081}$	8.520	$+16.811$ -14.791	$+0.653$ -0.701	$+2.060$ -4.416	$+16.672$ -14.099
(0, 2)	$0.372^{+0.061}_{-0.061}$	7.534	$+14.503$ -14.524	$+0.653$ -0.344	$+3.378$ -4.519	$+14.089$ -13.799
(0, 3)	$0.422^{+0.124}_{-0.113}$	7.053	$+28.443$ -25.787	$+0.511$ -0.267	$+0.000$ -4.388	$+28.438$ -25.410
(1, 0)	$0.317^{+0.054}_{-0.054}$	14.615	$+8.558$ -8.977	$+0.305$ -0.173	$+1.003$ -3.493	$+8.494$ -8.268
(1, 1)	$0.330^{+0.061}_{-0.054}$	8.007	$+16.650$ -14.148	$+1.672$ -1.754	$+1.663$ -1.417	$+16.482$ -13.968
(1, 2)	$0.263^{+0.035}_{-0.035}$	7.498	$+10.979$ -10.847	$+0.346$ -0.220	$+0.065$ -0.798	$+10.973$ -10.815
(1, 3)	$0.356^{+0.087}_{-0.077}$	6.171	$+23.695$ -20.802	$+0.545$ -0.678	$+2.058$ -1.917	$+23.599$ -20.702
(1, 4)	$0.284^{+0.108}_{-0.090}$	15.648	$+34.636$ -27.626	$+0.463$ -0.298	$+1.779$ -2.734	$+34.587$ -27.488
(2, 0)	$0.423^{+0.089}_{-0.094}$	14.831	$+15.072$ -16.454	$+1.937$ -2.121	$+11.273$ -13.372	$+9.815$ -9.350
(2, 1)	$0.187^{+0.045}_{-0.043}$	10.894	$+21.616$ -19.884	$+0.378$ -0.121	$+8.106$ -9.200	$+20.035$ -17.627
(2, 2)	$0.248^{+0.036}_{-0.035}$	9.026	$+11.428$ -10.769	$+0.264$ -0.163	$+6.100$ -5.723	$+9.660$ -9.121
(2, 3)	$0.257^{+0.031}_{-0.029}$	7.505	$+9.686$ -8.399	$+0.334$ -0.034	$+5.075$ -3.500	$+8.244$ -7.635
(2, 4)	$0.220^{+0.052}_{-0.049}$	15.536	$+18.179$ -15.941	$+0.562$ -0.793	$+0.000$ -6.191	$+18.171$ -14.668
(3, 0)	$0.098^{+0.027}_{-0.024}$	19.079	$+19.598$ -15.931	$+3.323$ -3.445	$+10.417$ 0.000	$+16.264$ -15.554
(3, 1)	$0.085^{+0.028}_{-0.024}$	15.873	$+28.149$ -23.182	$+0.355$ -0.410	$+1.737$ -2.174	$+28.093$ -23.076
(3, 2)	$0.070^{+0.019}_{-0.018}$	16.610	$+22.364$ -19.086	$+0.733$ -0.200	$+3.371$ -3.329	$+22.096$ -18.792
(3, 3)	$0.139^{+0.023}_{-0.022}$	10.604	$+12.799$ -11.925	$+0.314$ -0.187	$+1.601$ -1.022	$+12.695$ -11.880
(3, 4)	$0.082^{+0.023}_{-0.021}$	19.365	$+19.709$ -17.125	$+0.257$ -0.816	$+1.332$ -1.821	$+19.662$ -17.009
(4, 0)	$0.064^{+0.049}_{-0.042}$	40.041	$+66.409$ -53.296	$+2.627$ -4.872	$+0.000$ -14.468	$+66.357$ -51.063
(4, 1)	$0.092^{+0.048}_{-0.041}$	23.730	$+45.881$ -37.463	$+1.200$ -2.708	$+0.936$ -7.602	$+45.856$ -36.583
(4, 2)	$0.056^{+0.023}_{-0.020}$	28.376	$+30.530$ -22.668	$+0.000$ -0.338	$+3.153$ -0.880	$+30.366$ -22.649
(4, 3)	$0.060^{+0.029}_{-0.020}$	25.244	$+41.439$ -21.922	$+0.718$ -0.696	$+3.865$ -6.433	$+41.252$ -20.945
(4, 4)	$0.001^{+0.002}_{-0.002}$	293.522	$+157.697$ -45.054	$+1.640$ -3.380	$+1.184$ 0.000	$+157.684$ -44.927

Table 6.3: The K^+/π^+ ratio in p+NuMI interactions in (p_z, p_T) at 120 GeV/c. The statistical and systematic uncertainties are given.

Bin	K^+/π^+	Statistical	Total Systematic	Beam	Momentum	Background
(0, 0)	$0.136^{+0.025}_{-0.022}$	7.222	$+16.845$ -14.830	$+0.413$ -0.535	$+1.860$ 0.000	$+16.737$ -14.821
(0, 1)	$0.104^{+0.014}_{-0.012}$	4.926	$+12.993$ -10.924	$+0.426$ -0.227	$+4.557$ -2.172	$+12.160$ -10.703
(0, 2)	$0.161^{+0.034}_{-0.024}$	4.222	$+20.676$ -14.512	$+0.283$ -0.210	$+5.288$ -3.665	$+19.986$ -14.040
(0, 3)	$0.213^{+0.075}_{-0.042}$	4.355	$+35.146$ -19.035	$+0.590$ -0.672	$+3.326$ -1.533	$+34.983$ -18.961
(1, 0)	$0.094^{+0.012}_{-0.011}$	7.430	$+10.725$ -9.432	$+0.739$ -1.014	$+3.416$ -1.362	$+10.139$ -9.278
(1, 1)	$0.140^{+0.018}_{-0.016}$	4.166	$+12.360$ -10.959	$+1.034$ -0.580	$+0.000$ -0.280	$+12.317$ -10.940
(1, 2)	$0.171^{+0.028}_{-0.022}$	3.708	$+15.940$ -12.041	$+0.086$ 0.000	$+0.765$ -0.527	$+15.921$ -12.030
(1, 3)	$0.221^{+0.059}_{-0.035}$	3.597	$+26.447$ -15.285	$+0.512$ -0.514	$+1.458$ -0.908	$+26.402$ -15.249
(1, 4)	$0.472^{+0.153}_{-0.100}$	9.429	$+31.008$ -18.904	$+0.624$ -0.806	$+2.081$ -0.812	$+30.932$ -18.869
(2, 0)	$0.087^{+0.015}_{-0.013}$	8.297	$+15.173$ -12.404	$+0.427$ -0.291	$+10.820$ -8.186	$+10.628$ -9.315
(2, 1)	$0.156^{+0.031}_{-0.024}$	4.651	$+19.461$ -14.805	$+0.062$ -0.379	$+6.833$ -4.617	$+18.222$ -14.061
(2, 2)	$0.163^{+0.018}_{-0.017}$	4.371	$+10.447$ -9.176	$+0.000$ -0.077	$+2.552$ -2.794	$+10.131$ -8.740
(2, 3)	$0.202^{+0.018}_{-0.016}$	3.826	$+8.038$ -7.030	$+0.049$ -0.195	$+2.324$ -3.442	$+7.695$ -6.126
(2, 4)	$0.259^{+0.048}_{-0.035}$	8.038	$+16.554$ -10.908	$+0.993$ -1.298	$+1.592$ -0.950	$+16.448$ -10.788
(3, 0)	$0.327^{+0.061}_{-0.046}$	6.201	$+17.678$ -12.573	$+2.211$ -2.323	$+4.195$ -5.689	$+17.031$ -10.969
(3, 1)	$0.214^{+0.056}_{-0.034}$	4.843	$+25.702$ -15.224	$+1.066$ -0.865	$+1.176$ -0.607	$+25.653$ -15.187
(3, 2)	$0.206^{+0.047}_{-0.031}$	4.958	$+22.549$ -14.189	$+0.575$ -0.569	$+1.933$ -2.423	$+22.458$ -13.970
(3, 3)	$0.195^{+0.033}_{-0.023}$	4.403	$+16.608$ -10.714	$+0.173$ -0.077	$+1.143$ -1.068	$+16.568$ -10.660
(3, 4)	$0.232^{+0.061}_{-0.038}$	7.427	$+25.385$ -14.556	$+0.296$ -0.418	$+2.440$ -1.804	$+25.266$ -14.438
(4, 0)	$0.328^{+0.395}_{-0.136}$	10.927	$+119.969$ -39.899	$+0.000$ -1.404	$+1.477$ -2.440	$+119.960$ -39.800
(4, 1)	$0.308^{+0.193}_{-0.090}$	8.061	$+62.198$ -28.270	$+0.350$ -0.326	$+0.000$ -2.072	$+62.197$ -28.192
(4, 2)	$0.305^{+0.075}_{-0.050}$	8.799	$+22.854$ -13.634	$+0.182$ -0.263	$+0.458$ -1.528	$+22.849$ -13.545
(4, 3)	$0.209^{+0.031}_{-0.026}$	8.476	$+12.279$ -9.049	$+1.720$ -1.389	$+3.035$ -1.730	$+11.773$ -8.773
(4, 4)	$0.213^{+0.116}_{-0.060}$	13.996	$+52.655$ -24.532	$+3.376$ -2.361	$+0.000$ -1.539	$+52.546$ -24.370

Table 6.4: The K^-/π^- ratio in p+NuMI interactions in (p_z, p_T) at 120 GeV/c. The statistical and systematic uncertainties are given.

Bin	K^-/π^-	Statistical	Total Systematic	Beam	Momentum	Background
			Errors in percent			
$(0, 0)$	$0.069^{+0.010}_{-0.010}$	12.954	$+7.794$ -7.350	$+0.773$ -0.791	$+0.270$ -1.701	$+7.751$ -7.107
$(0, 1)$	$0.077^{+0.015}_{-0.013}$	7.398	$+17.756$ -15.152	$+0.128$ 0.000	$+1.414$ -0.900	$+17.699$ -15.126
$(0, 2)$	$0.084^{+0.010}_{-0.009}$	6.707	$+9.637$ -8.231	$+0.418$ -0.018	$+1.884$ -0.330	$+9.442$ -8.224
$(0, 3)$	$0.126^{+0.034}_{-0.020}$	6.156	$+25.967$ -14.340	$+0.510$ -0.398	$+0.000$ -2.215	$+25.962$ -14.162
$(1, 0)$	$0.064^{+0.009}_{-0.009}$	13.173	$+4.801$ -4.732	$+0.924$ -1.009	$+0.779$ -1.774	$+4.646$ -4.270
$(1, 1)$	$0.087^{+0.017}_{-0.014}$	7.283	$+17.624$ -14.903	$+0.827$ -0.473	$+0.000$ -0.789	$+17.604$ -14.875
$(1, 2)$	$0.074^{+0.006}_{-0.006}$	6.918	$+5.118$ -4.356	$+0.355$ -0.074	$+1.129$ -1.080	$+4.979$ -4.219
$(1, 3)$	$0.115^{+0.028}_{-0.017}$	5.500	$+23.893$ -13.378	$+0.000$ -0.149	$+2.548$ -2.178	$+23.757$ -13.198
$(1, 4)$	$0.169^{+0.071}_{-0.044}$	14.359	$+39.371$ -21.369	$+0.219$ -0.114	$+0.623$ -1.380	$+39.365$ -21.324
$(2, 0)$	$0.100^{+0.016}_{-0.016}$	13.127	$+9.373$ -9.136	$+2.337$ -2.387	$+0.454$ -2.658	$+9.066$ -8.408
$(2, 1)$	$0.066^{+0.015}_{-0.013}$	10.322	$+20.190$ -16.662	$+0.432$ -0.686	$+2.427$ -1.901	$+20.039$ -16.539
$(2, 2)$	$0.079^{+0.009}_{-0.009}$	8.380	$+7.970$ -7.223	$+0.668$ -0.481	$+1.449$ -2.071	$+7.809$ -6.903
$(2, 3)$	$0.087^{+0.011}_{-0.009}$	6.936	$+10.557$ -6.969	$+0.593$ -0.393	$+0.306$ 0.000	$+10.536$ -6.958
$(2, 4)$	$0.078^{+0.020}_{-0.015}$	14.259	$+20.735$ -12.136	$+1.780$ -2.064	$+0.000$ -3.750	$+20.658$ -11.356
$(3, 0)$	$0.097^{+0.024}_{-0.022}$	19.197	$+16.313$ -12.408	$+0.503$ -1.066	$+5.743$ 0.000	$+15.260$ -12.363
$(3, 1)$	$0.055^{+0.018}_{-0.013}$	15.714	$+28.138$ -17.420	$+0.384$ -0.617	$+0.000$ -0.922	$+28.136$ -17.385
$(3, 2)$	$0.034^{+0.009}_{-0.007}$	16.326	$+19.256$ -13.199	$+0.737$ -0.220	$+0.000$ -1.090	$+19.242$ -13.152
$(3, 3)$	$0.058^{+0.007}_{-0.006}$	10.196	$+6.209$ -3.463	$+0.354$ -0.166	$+0.724$ -0.748	$+6.156$ -3.378
$(3, 4)$	$0.031^{+0.007}_{-0.006}$	18.719	$+11.598$ -4.729	$+0.986$ -1.341	$+0.725$ -0.409	$+11.533$ -4.516
$(4, 0)$	$0.068^{+0.031}_{-0.031}$	40.604	$+20.838$ -19.594	$+1.516$ -3.965	$+0.000$ -13.812	$+20.783$ -13.321
$(4, 1)$	$0.094^{+0.037}_{-0.029}$	23.931	$+31.673$ -18.863	$+0.811$ -2.264	$+0.000$ -5.674	$+31.662$ -17.846
$(4, 2)$	$0.042^{+0.019}_{-0.014}$	28.167	$+33.712$ -18.033	$+0.193$ -0.677	$+1.900$ 0.000	$+33.658$ -18.020
$(4, 3)$	$0.030^{+0.016}_{-0.010}$	24.714	$+46.135$ -19.503	$+1.104$ -0.767	$+1.964$ -3.017	$+46.080$ -19.253
$(4, 4)$	$0.000^{+0.001}_{-0.001}$	293.353	$+155.056$ -33.614	$+0.105$ -0.949	$+2.152$ 0.000	$+155.041$ -33.600

As presented in Figure 6.1, the dependence of the ratios on both variables p_z and p_T are visible: the π^-/π^+ and K^+/π^+ ratios increase with p_T, whereas the π^-/π^+, K^-/K^+ and K^-/π^- ratios decrease with p_z.

6.2   Comparison to Other Data and Models

In this section, the π^-/π^+, K^-/K^+ and $K^\pm/\pi^\pm$ ratios for the NuMI data are compared with the thin Carbon data and the Monte Carlo simulation. In addition, the comparison between the NuMI data and the MINOS models are presented.

Figure 6.2 shows the ratios produced in the NuMI data, the thin Carbon data and the NuMI Monte Carlo simulation as a function of momentum bin. Important substructures in both data sets are directly comparable to the NuMI Monte Carlo simulation. However, the Monte Carlo simulation overestimates the π^-/π^+ and K^-/K^+ ratios, while it underestimates the K^+/π^+ ratio. The poor agreement between simulation and data indicates that the particle production on the NuMI target is not well simulated.

In comparison to the p+C collisions [3], the NuMI data show a steeper structure in p_T for π^-/π^+ and K^+/π^+, whereas the decreasing slope of p_z in K^-/K^+ in the NuMI data clearly visible. Also, the NuMI data tend to have higher K^+/π^+ in most momentum bins than the thin Carbon data. Note however that the thin Carbon data points have asymmetric error bars which are larger in the upper limit. This may indicate the need for a more detailed background study of the thin Carbon data.
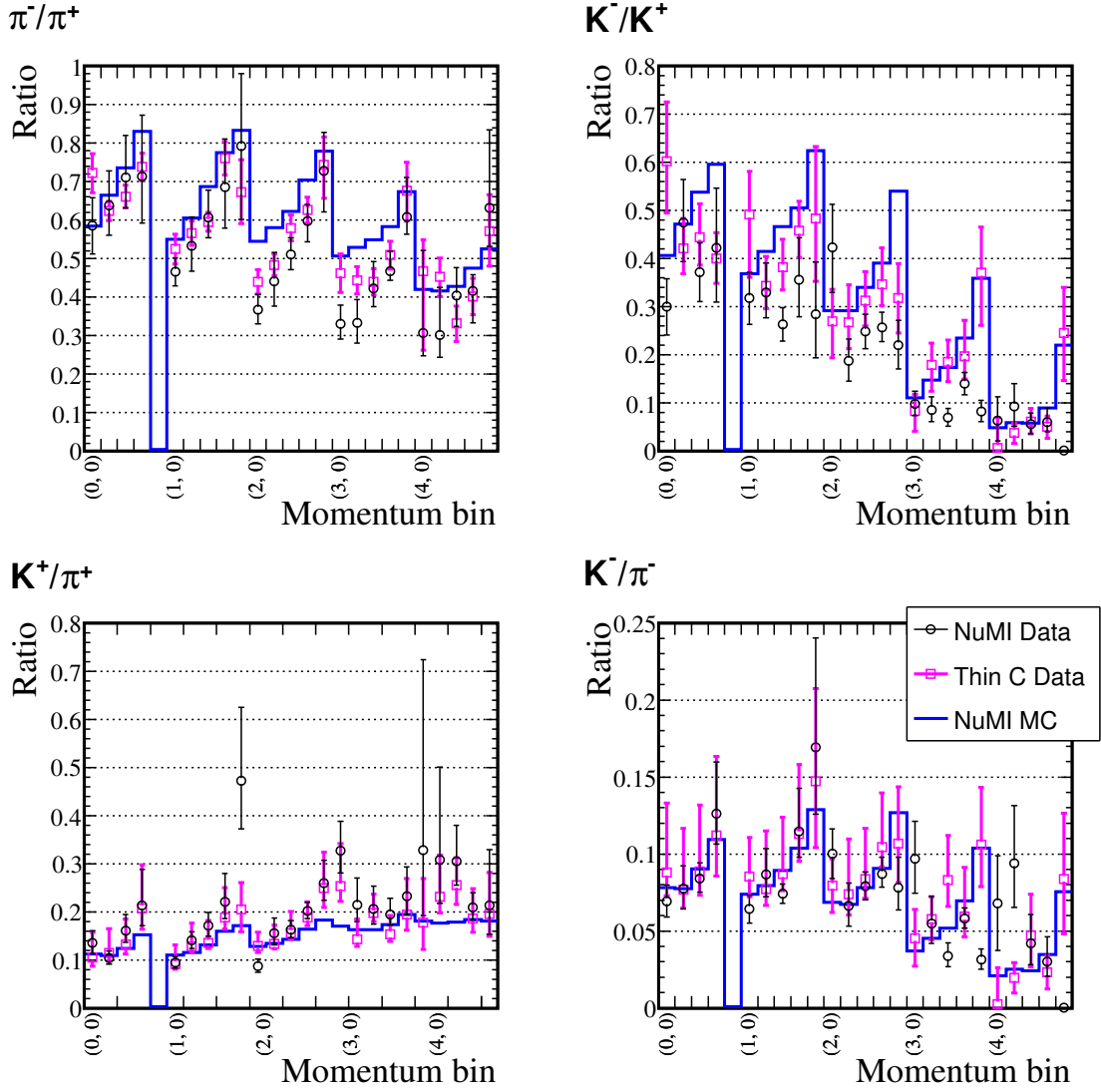
Figure 6.2: The ratios as a function of (p_z, p_T) for π^-/π^+, K^-/K^+ and $K^\pm/\pi^\pm$ produced in p+NuMI, p+C collisions and NuMI Monte Carlo simulation at 120 GeV/c.

Figure 6.3 shows the ratios between the NuMI data and the thin Carbon data, and the ratios between the NuMI Monte Carlo simulation and the thin Carbon Monte Carlo simulation. As discussed above, and shown in Figure 6.2, the distributions have steep slopes in p_T in the NuMI data and they are more pronounced than in p+C collisions. This feature is clearly visible in the Monte Carlo ratio of π^-/π^+ in Figure 6.3. It also demonstrates that the ratios are expected to be smaller than 1 in the Monte Carlo simulation for π^-/π^+ and K^-/K^+, and larger than 1 for K^+/π^+ and K^-/π^-, which is consistent with the data measurement in most bins.

Note that the thin Carbon target has an interaction length of 2 %, whereas the NuMI target has an interaction length of 90 %. The particle ratios from the measurements of proton-Carbon interactions account for only the interactions of the primary protons, and so the effect of re-interactions in the NuMI target should be the primary difference between the two data samples.

The only other relevant models which can be directly compared to the NuMI data are the MINOS models [4, 5]. In order to assess differences between the MINOS models and the NuMI data, the ratios at different (p_z, p_T) presented in Figure 6.1 are replotted for p_T <0.2 GeV/c and 0.2 GeV/c < p_T <0.4 GeV/c as a function of p_z. This allows a clear view of the substructure at low p_T. These comparisons are shown in Figure 6.4 and Figure 6.5.

This comparison shows global similarities. Remarkable differences are however visible in $K^\pm/\pi^\pm$ at high p_z where, a clear upward deviation with the MINOS refit
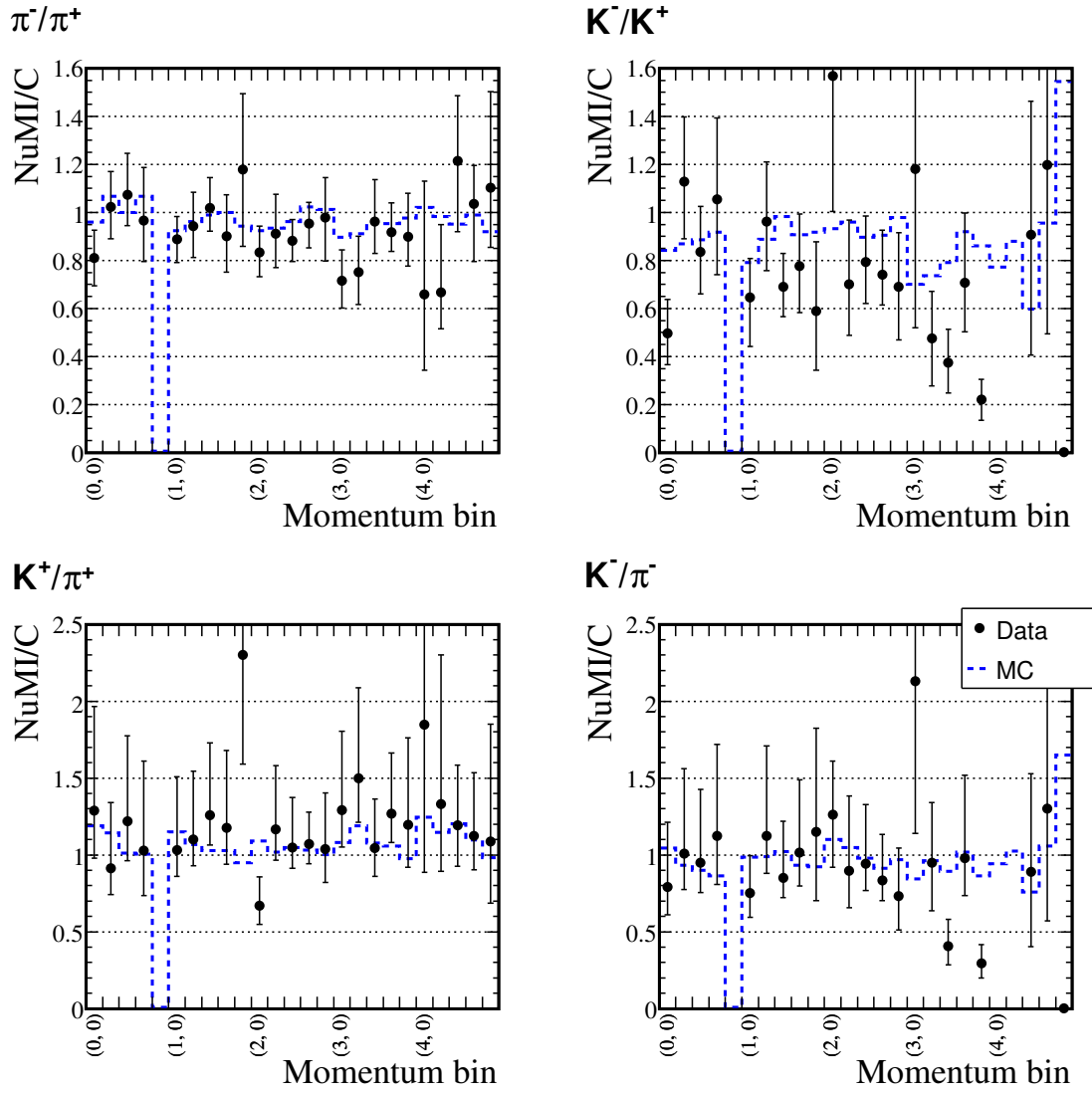
Figure 6.3: The ratios between p+NuMI and p+C collisions as a function of (p_z, p_T) for π^-/π^+, K^-/K^+ and $K^\pm/\pi^\pm$ in data and Monte Carlo simulation at 120 GeV/c. Points: data; dashed line: Monte Carlo simulation.
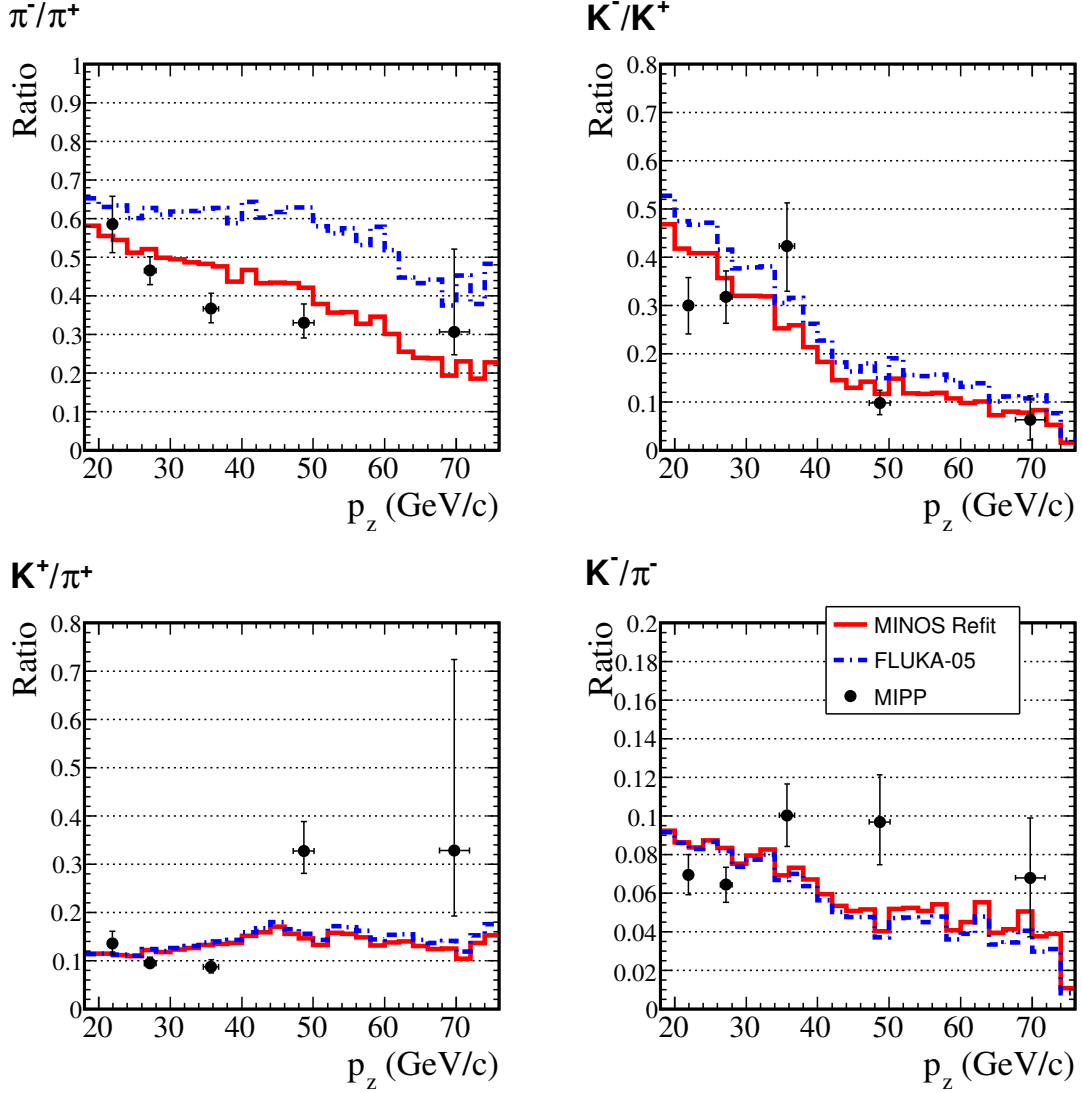
Figure 6.4: The ratios as a function of p_z at p_T <0.2 GeV/c for π^-/π^+, K^-/K^+ and $K^\pm/\pi^\pm$ produced in MIPP NuMI data and the MINOS models.
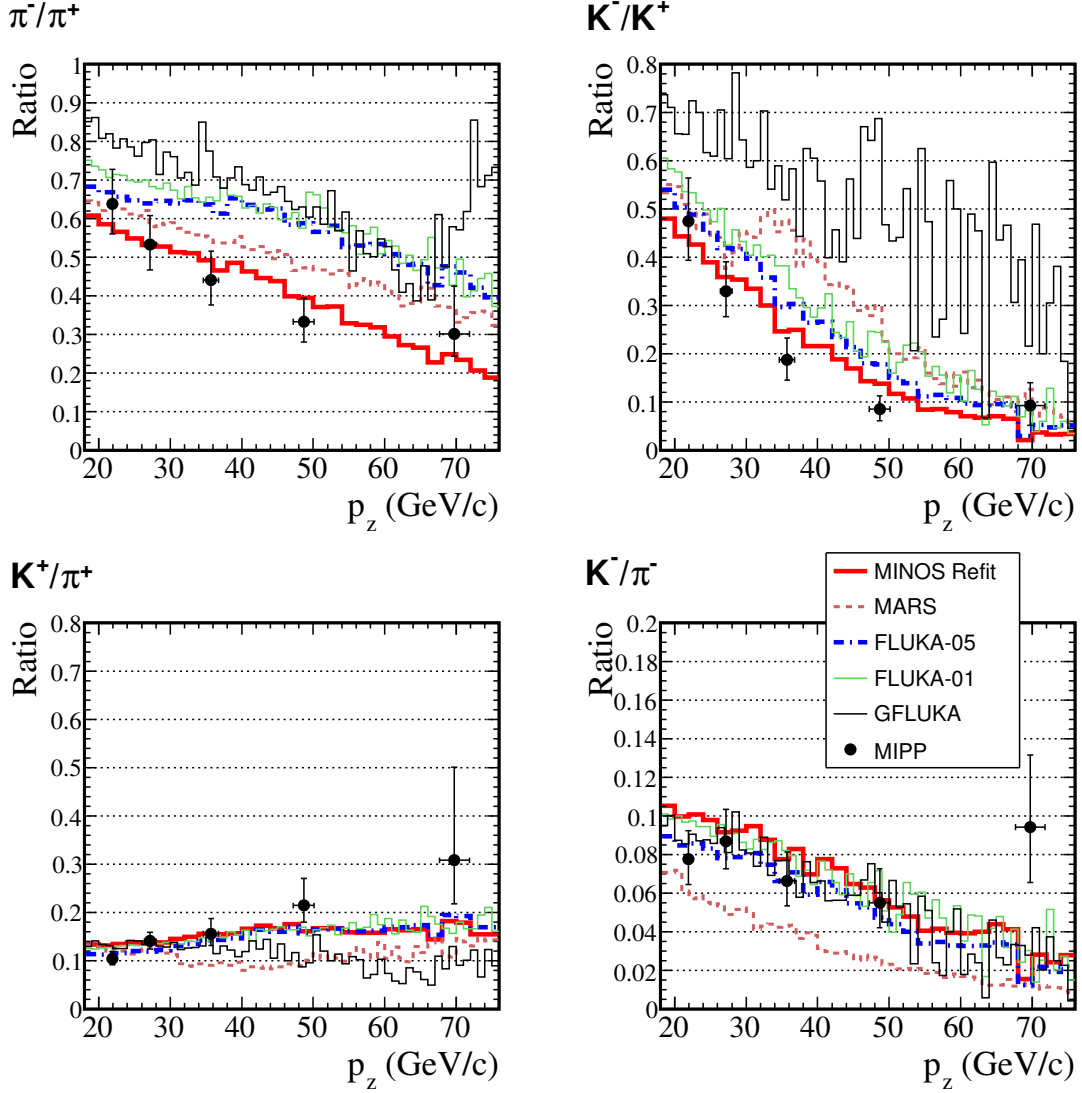
Figure 6.5: The ratios as a function of p_z at 0.2 GeV/c < p_T <0.4 GeV/c for π^-/π^+, K^-/K^+ and $K^\pm/\pi^\pm$ produced in MIPP NuMI data and the MINOS models.

is evident. It is interesting to note that these data structures agree with the MINOS

refit parametrization more than other models.

Chapter 7

Conclusions

The π^-/π^+, K^-/K^+, π^+/K^+ and π^-/K^- production ratios for proton inter-
actions with the NuMI target observed with the MIPP experiment are presented.
The data cover the high momentum region with p_T <2 GeV/c and 20 GeV/c <
p_z <90 GeV/c. The statistical uncertainties are typically at the 10% level for π^-/π^+
and π^+/K^+. An iterative, data-driven method is used to evaluate the accuracy of
the Monte Carlo simulation and reduce the particle identification background.

These data carry important information concerning understanding of the neutrino
spectrum in MINOS from the NuMI beam. The data also provide substantial new in-
put to hadron production models for Monte Carlo simulations. Detailed comparisons
with the MIPP thin Carbon data and the Monte Carlo simulations in the correspond-
ing energy range, as well as comparisons to the existing MINOS models, demonstrate
that the models in general agree with the data. Some discrepancies exist however,

particularly for K^+/π^+ at high p_z. It is also interesting to note that the MINOS Refit model shows generally better agreement than any other model.

A natural extension to this work would be to compute particle yields from the NuMI target based on the thin Carbon target measurements by taking into account the contribution of cascade processes and tertiary particle production. Also, improvements to the particle identification and background estimation should be possible by using the information from other sub-detectors. This would also improve momentum space coverage. Finally, the MIPP data collected for other thin targets can be used to provide a deeper understanding of hadron production in the Monte Carlo models.

Bibliography

[1] The NuMI Technical Design Handbook. 1998.

[2] MINOS Technical Design Report. MINOS-doc-337, 1998.

[3] A. Lebedev. *Ratio of Pion Kaon Production in Proton Carbon Interactions*. PhD thesis, Harvard University, Cambridge, MA, May 2007.

[4] D. G. Michael *et al.* [MINOS Collaboration]. Observation of muon neutrino disappearance with the MINOS detectors and the NuMI neutrino beam. *Phys. Rev. Lett.*, **97**:191801, 2006.

[5] Zarko Pavlovic. private communication.

[6] H. W. Atherton *et al.* Precise measurements of particle production by 400 GeV/c protons on beryllium targets. CERN 80-07, 1980.

[7] D. S. Barton *et al.* Experimental study of the *A dependence of inclusive hadron fragmentation. Phys. Rev. D*, **27**:2580–2599, 1983.

[8] G. Ambrosini *et al.* Measurement of charged particle production from 450 GeV/c protons on beryllium. *Eur. Phys. J.*, **C10**:605–627, 1999.

[9] M. G. Catanesi *et al.* Proposal for hadron production measurements using the NA49 detector for use in long-baseline and atmospheric neutrino flux calculations. CERN-SPSC/2001-017, 2001.

[10] Application Software Group. Geant – detector description and simulation tool. CERN Program Library Long Writeup W5013, 1994.

[11] A. Fassò, A. Ferrari, J. Ranft, and P.R. Sala. Fluka: a multi-particle transport code. CERN-2005-10 (2005), INFN/TC_05/11, SLAC-R-773.

[12] A. Fassò, A. Ferrari, S. Roesler, P.R. Sala, G. Battistoni, F. Cerutti, E. Gadioli, M.V. Garzelli, F. Ballarini, A. Ottolenghi, A. Empl and J. Ranft. The physics models of fluka: status and recent developments. Computing in High Energy and Nuclear Physics 2003 Conference (CHEP2003), La Jolla, CA, USA, March 24-28, 2003, (paper MOMT005), eConf C0303241 (2003), arXiv:hep-ph/0306267.

[13] N. V. Mokhov. The MARS Code System User's Guide, Version 13(95). Report Fermilab-FN-628, 1995.

[14] F. Pietropaolo M. Bonesini, A. Marchionni and T. Tabarelli de Fatis. On particle production for high energy neutrino beams. *Eur. Phys. J.*, **C20**:13–27, 2001.

[15] A. J. Malensek. Empirical Formula for Thick Target Particle Production. Fermilab-FN 341, 1981.

[16] A. Abramov *et al.* Dynamic Stress Calculations for ME and LE Targets and Results of Prototyping for the LE Target. MINOS-doc-675, 2000.

[17] J. Engelfried *et al.* Selex phototube rich detector. *Nucl. Instr. and Meth. A*, **431**:53–69, 1999.

[18] J. Paley, R. Soltz, P. D. Barnes, M. Heffner, J. Klay and D. Miller. MIPP TPC Reconstruction. MIPP-doc-129, 2006.

[19] Xihong Yang. *Centrality dependence of strangeness production in proton-nucleus collisions at AGS energies.* PhD thesis, Columbia University, 2000.

[20] M. Starič and P. Križan. An iterative method for the analysis of Cherenkov rings in the HERA-B RICH. *Nucl. Phys. A*, **433**:279–285, 1999.

Appendix A

Maximization of Purity and

Efficiency

In this Appendix, the proof that the likelihood ratio cuts should be tuned to maximize $\mathcal{P} \times \mathcal{E}$ is demonstrated, where $\mathcal{P} =$Purity and $\mathcal{E}=$efficiency.

Let us assume the following parameters:

$S_0 =$ the total number of signal events

$S =$ the measured number of signal events

$B =$ the number of measured background events

$\sigma =$ error on S

Using the definitions of purity and efficiency,

$S = \mathcal{E} S_0$

$\mathcal{P} = S/(S + B).$

Solving for B, we have

$B = S(1 - \mathcal{P})/\mathcal{P}$.

Given that $\sigma = \sqrt{S + B}$, the fractional error on S is:

$\sigma/S = \sqrt{S + B}/S = \sqrt{S + S(1 - \mathcal{P})/\mathcal{P}}/S = \sqrt{(1 + (1 - \mathcal{P})/\mathcal{P})/S}$

$\sigma/S = 1/\sqrt{\mathcal{P}S} = 1/\sqrt{\mathcal{E}\mathcal{P}S_0}$.

Therefore, in order to minimize σ/S, one would need to to maximize $\mathcal{E}\mathcal{P}$.